Simulating Open Quantum System Chemical Dynamics on Classical and Quantum Computing Devices

by

Pouya Khazaei

A dissertation submitted in partial fulfillment
of the requirements for the degree of
Doctor of Philosophy
(Chemistry)
in The University of Michigan
2026

Doctoral Committee:

Professor Eitan Geva, Chair
Assistant Professor Yuki Kobayashi
Professor Roseanne Sension
Professor Dominika Zgid

Pouya Khazaei
pkhazaei@umich.edu
ORCID iD: 0009-0005-2847-4798

© Pouya Khazaei 2026

DEDICATION

For Mom

ACKNOWLEDGEMENTS

I would like to thank everyone who made this dissertation possible.

First and foremost, I am deeply grateful to my advisor, Professor Eitan Geva, for his guidance, mentorship, and steady support throughout my Ph.D. This work would not have been possible without his direction and encouragement.

I would also like to thank my committee members—Professor Dominika Zgid, Professor Yuki Kobayashi, and Professor Rosanne Sension—for their insightful feedback and enriching instruction. Their perspectives strengthened this work and broadened my understanding.

I am grateful to all past and present members of the Geva group—Zongwei Huang, Dr. Ellen Mulvihill, Dr. Miriam Lenn, Dalia Hassan, Callie Wilson, Dr. Yifan Lai, Dr. Maximilian Saller, and Eric Ma—for their mentorship, collaboration, and thoughtful discussions. I am especially thankful to Yifan Lai for introducing me to the OD-QME framework and for the detailed notes and discussions that greatly shaped my development. I am also grateful to Eric Ma, who has been an outstanding mentee and colleague.

I would like to acknowledge my collaborators at the Center for Quantum Dynamics on Modular Quantum Devices (CQD-MQD). This initiative, spearheaded by Professor Victor Batista at Yale University, provided an exciting and supportive research environment. I am thankful to Professor Batista, Professor Sabre Kais, Professor Lea Ferreira dos Santos, and Professor Michel Devoret for their guidance and encouragement throughout this journey. I also appreciate the many collaborators within the center whose initiative and contributions enriched our shared projects.

Finally, I would like to thank my family and friends. To my mom, who has always believed in me and supported me every step of the way—her optimism and joy have meant more than I can express. To my aunt Sima, whose kindness and generosity inspire everyone around her. To my grandmother, who was always proud and quick with a joke, and whose encouragement meant so much. To my cousin Lily, who shared much of this journey with me here in Michigan and was always a source of laughter and conversation. To my brother, who has helped me navigate important decisions and offered thoughtful advice. To Lily's parents, for their warmth and encouragement. And finally, to Erik, a great friend throughout this program, whether making music or simply enjoying whatever activity came next.

TABLE OF CONTENTS

DEDICATION ii

ACKNOWLEDGEMENTS iii

LIST OF FIGURES vi

LIST OF TABLES viii

ABSTRACT ix

CHAPTER

1 Introduction 1

1.1 Background: Motivation and Quantum Dynamics 1
1.2 Simulating Quantum Dynamics on Classical Devices 7
1.2.1 Classical Representation of Quantum States 7
1.2.2 Classical Time-Evolution of Quantum States 7
1.3 Simulating Quantum Dynamics on Quantum Devices 9
1.3.1 Quantum Representation of Quantum States 9
1.4 Overview of the Dissertation 12

2 Cavity-Modified Nonequilibrium Fermi's Golden Rule Rate Coefficients from Cavity-Free Inputs 13

2.1 Statement of Collaboration 13
2.2 Introduction 13
2.3 Theory 15
2.3.1 Preliminary considerations 15
2.3.2 Cavity-modified population-only off-diagonal quantum master equation and nonequilibrium Fermi's golden rule rates 17
2.3.3 Asymptotic behavior and cavity-modified instantaneous Marcus theory 20
2.4 Cavity-modified rates for photo-induced charge transfer in the Carotenoid-Porphyrin-C_{60} Triad dissolved in liquid Tetrahydrofuran 22
2.5 Cavity-modified rates for the Garg-Onuchic-Ambegaokar (GOA) model of an electron transfer reaction in the condensed phase 26
2.6 Summary and concluding remarks 30

3 Solution of Nonautonomous Linear Ordinary Differential Equations on a Quantum Device 34

3.1 Statement of Collaboration . . . 34
3.2 Introduction . . . 34
3.3 Theory . . . 36
3.3.1 Linear Nonautonomous Ordinary Differential Equations . . . 36
3.3.2 Quantum Algorithm for the System Dynamics . . . 37
3.3.3 Summary of the EOM for SVD of $\Phi(t)$ . . . 39
3.3.4 EOM for $\Sigma^{\pm}$ . . . 40
3.3.5 Summary: SVD-EOM for Quantum Evolution of Nonautonomous Linear ODEs . . . 41
3.3.6 Quantum Algorithm for U and V . . . 42
3.3.7 Quantum Algorithm for $\Sigma^{\pm}$ . . . 44
3.4 Results & Discussion . . . 45
3.4.1 Noise Model . . . 45
3.4.2 Results . . . 46
3.5 Summary and Conclusions . . . 49

4 A Roadmap for Simulating Chemical Dynamics on a Parametrically Driven Bosonic Quantum Device . . . 51

4.1 Statement of Collaboration . . . 51
4.2 Introduction and Motivation . . . 52
4.3 Kerr-Cat Device and Effective Hamiltonian . . . 55
4.4 Device Dynamics versus Chemical Dynamics . . . 60
4.5 Concluding Remarks . . . 63

5 Conclusion . . . 67

5.1 Summary . . . 67
5.2 Outlook . . . 68

BIBLIOGRAPHY . . . 71

LIST OF FIGURES

FIGURE

1.1 Representative examples of chemical dynamical processes considered in this thesis. (a) Electronic charge transfer in an organic photovoltaic system consisting of a subphthalocyanine donor and a fullerene acceptor. (b) Excitation energy transfer in the photosynthetic Fenna–Matthews–Olson (FMO) complex. (c) Proton transfer in a guanine–cytosine DNA base pair, proceeding from the canonical form G–C through the transition state (TS) to the tautomeric form G^*–C^*. Panel (a) is adapted with permission from Lee, M. H.; Geva, E.; Dunietz, B. D. *J. Phys. Chem. C* **2014**, *118* (18), 9780–9789. Copyright 2014 American Chemical Society. Panels (b) and (c) are adapted from Refs. 1 and 2, respectively, under CC BY 4.0 licenses 2

2.1 Top panel: A schematic view of CPC_{60}/THF. Middle panel: The NE-FGR rate coefficient, $k_{D\to A}(t)$, for the $\pi\pi^*$ $\to$CT1 transition when CPC_{60} is in its bent conformation. Bottom panel: The population of the $\pi\pi^*$ donor state as a function of time, $P_D(t)$, simulated based on the p-tcl-OD-QME, Eq. 2.8. Shown are results based NE-FGR (NE), E-FGR (EQ) and the IMT approximation for NE-FGR (IMT). C indicates "in-cavity", while lack of C indicates "cavity-free". E.g., NE and C-NE corresponds to cavity-free and cavity-modified NE-FGR, respectively. 25

2.2 A schematic view of the GOA model under consideration and the nonequilibrium initial state. The donor (blue) and acceptor (red) PESs are plotted along the GOA model's primary mode coordinate. The number 2 corresponds to the shift, $s/y_0 = 2.0$, of the ground state equilibrium geometry elative to the donor's equilibrium geometry (orange, see Eq. 2.39). 31

2.3 Comparison of donor-to-acceptor transition rates, $k_{D\to A}(t)$, (top panels) and donor population, $P_D(t)$, (bottom panels) as a function of time, at different temperatures and frictions, for the GOA model. Shown are results based NE-FGR (NE), E-FGR (EQ) and the IMT approximation for NE-FGR (IMT). C indicates "in-cavity", while lack of C indicates "cavity-free". For example, NE and C-NE corresponds to cavity-free and cavity-modified NE-FGR, respectively. 32

3.1 Quantum circuit implementing the SVD-based dilation using $V^\dagger$, U_Σ, and U on the system register and Hadamard gates on the ancilla. 38

3.2 Quantum circuit illustrating the application of the single-step Cayley update $\mathrm{cay}(Z)^T \otimes I$ to the vectorized state $|U\rangle\rangle$. 43

3.3 Molecular structure of the CPC_{60} triad solvated in tetrahydrofuran (THF). . . . 47

3.4 Comparison of donor population dynamics obtained from the p-tcl-OD-QME (classical RK2 integration) and the SVD-EOM propagated on a noisy quantum simulator. The noise strength is scaled by $f \in \{10^{-3}, 5 \times 10^{-3}, 10^{-2}, 5 \times 10^{-2}, 10^{-1}, 5 \times 10^{-1}, 1\}$. 48

4.1 Schematic of Bosonic cQED Device for Quantum Dynamics Simulations in Hydrogen-Bonded Complexes. Adapted from Ref. 3. Copyright (2024) American Chemical Society. The device is a half-aluminum, half-copper cavity resonator containing two sapphire chips with a SNAIL-transmon, readout resonator, and Purcell filter (top left).[4] A strong microwave drive at twice the resonance frequency converts the SNAIL-transmon Hamiltonian into the bi-stable Kerr-cat parametric oscillator Hamiltonian for analog simulations of quantum dynamics in molecular systems, such as the adenine-thymine dimer (top right). Parameters $\Delta, K, \epsilon_1, \epsilon_2$ (middle left) are adjusted to map the effective Hamiltonian $\hat{H}_{KC}$ to the double-well Hamiltonian modeling the molecular system (middle right). The bottom left shows the Wigner transform phase space representation of the device quantum states, which are analogous to the states in molecular the double-well potential in the bottom right. 56

4.2 Hydrogen bonded complexes studied to analyze intramolecular proton transfer in cis-cis and cis-trans malonaldehyde (top), intramolecular proton transfer in adenine-thymine (amine, pyrimidine) (middle), and guanine-cytosine (amine, pyrimidine) base pairs. 57

4.3 Eigenstates obtained by diagonalization of the model Hamiltonians for cis-cis malonaldehyde (A), cis-trans malonaldehyde (B), adenine-thymine (C), and guanine-cytosine (D), based on either the chemical double-well Hamiltonian (blue) or the Kerr-cat Hamiltonian (red) with $c = 0.1\,\mathrm{a_0}$. Eigenstates are shown together with the potential energy surface as a function of the reaction coordinate 'x'. 60

4.4 Absolute energy differences for the lower lying eigenstates of the chemical double-well and Kerr-cat Hamiltonian (panels I) and cQED device parameters (panels II) as a function of the scaling parameter c for cis-cis malonaldehyde (A), cis-trans malonaldehyde (B), adenine-thymine (C) and guanine-cytosine (D). The horizontal black dashed line in panels I indicates the threshold of chemical accuracy at 1.5 $\mathrm{mE_h}$. The horizontal dashed lines in panels II indicate the maximum values of the parameters available in current cQED devices. The vertical dashed line indicates the maximum value of c recommended for accurate dynamics simulations (panels I) and minimum value of c ensuring experimental parameters available in existing cQED Kerr-cat platforms (panels II). [4] 65

4.5 Comparison of observables obtained with $\hat{H}_{DW}$ (solid lines) and $\hat{H}_{KC}$ (diamonds) as a function of c, using $\kappa = 0.1$ and $n_{\mathrm{th}} = 0.1$, for cis-cis malonaldehyde (A), cis-trans malonaldehyde (B), adenine-thymine (C) and guanine-cytosine (D). The time evolution of the product population is shown in the top subpanels (I), while the corresponding inverse reaction rate constants are shown in the bottom subpanels (II). 66

LIST OF TABLES

TABLE

2.1 The GOA model parameters used in this work. 29

3.1 Noise parameters extracted from the `FakeHanoiV2` backend. p_1 and p_2 denote single- and two-qubit depolarizing probabilities, T_1 and T_2 are coherence times, t_1, t_2, and t_m are gate and measurement durations, and p_{10}, p_{01} define the readout confusion matrix R. 46

4.1 Parameters used to simulate double-well potentials for proton transfer in molecular systems, according to the equation $V = k_4x^4 - k_2x^2 + k_1x$. 57

4.2 Table of inverse reaction rate constants T_X (in $\hbar/\mathrm{E_h}$) for each chemical system obtained with the $\hat{H}_{DW}$ and $\hat{H}_{KC}$ Hamiltonians, for various κ and n_{th} values with $c = 0.1\,\mathrm{a_0}$ 63

ABSTRACT

Modeling chemical dynamics is essential for understanding, predicting, and optimizing chemical processes. Because realistic chemical systems involve many interacting degrees of freedom, direct propagation of the many-body Schrödinger equation is intractable for all but the smallest systems. Quantum information platforms offer a fundamentally different representation: a d-dimensional state may be encoded using $k = \log_2(d)$ qubits rather than storing each amplitude independently. To harness this advantage for chemistry, it is necessary to develop quantum algorithms and hardware architectures capable of simulating the open-system dynamics ubiquitous in condensed-phase and molecular environments.

In the first chapter, we develop a theoretical framework for simulating a cavity-modified photoinduced charge-transfer reaction in the carotenoid–porphyrin–C_{60} (CPC_{60}) molecular triad dissolved in tetrahydrofuran (THF). Nonequilibrium Fermi's Golden Rule (NE-FGR) rate coefficients are obtained as a product of cavity-free and cavity-modified correlation functions. We further introduce an approximation based on Instantaneous Marcus Theory (IMT) that closely tracks the full NE-FGR result across all relevant time scales. Population transfer rates computed from the population-only off-diagonal quantum master equation (p-tcl-OD-QME) are shown to be consistent with the NE-FGR predictions. Our results demonstrate that nonequilibrium charge-transfer dynamics are significantly modified by coupling to an optical cavity.

The second chapter addresses the integration of linear nonautonomous ordinary differential equations on digital quantum hardware. Rather than classically constructing a nonunitary propagator at each time step and embedding it into a larger unitary operation for execution on quantum hardware, we eliminate this classical–quantum partitioning. We derive and propagate differential equations for the singular value decomposition (SVD) factors of the propagator directly, enabling time evolution to be implemented within a quantum-compatible framework. This approach shifts the locus of time integration from the classical processor to the quantum device.

In the third chapter, we investigate the feasibility of simulating chemical reaction dynamics on a parametrically driven bosonic superconducting Kerr-cat device. This analog platform enables direct control over parameters defining an effective double-well free-energy

landscape, as well as over environmental factors such as temperature and system–bath coupling strength. We demonstrate that proton transfer dynamics in prototypical benchmark systems, including hydrogen-bonded dimers of malonaldehyde and DNA base pairs, can be accurately reproduced using experimentally accessible Kerr-cat architectures.

CHAPTER 1

Introduction

1.1 Background: Motivation and Quantum Dynamics

Chemical dynamics concerns the time evolution of many-particle systems, including processes such as energy transfer, charge transfer, and chemical reactivity.[5, 6] These dynamical processes underpin a wide range of phenomena across molecular and condensed-phase systems.

For instance, excitation energy transfer is central to photosynthetic light-harvesting complexes, such as the Fenna–Matthews–Olson (FMO) complex,[7, 8] and underlies widely used fluorescence-based techniques including Förster resonance energy transfer (FRET).[9] Electronic charge transfer lies at the heart of redox chemistry and plays a key role in emerging technologies such as organic photovoltaics[10, 11, 12] and molecular electronics.[13, 14] Chemical reactivity, meanwhile, encompasses fundamental transformations such as proton transfer in DNA base pairs[15] and in extended hydrogen-bonded networks, ranging from aqueous solutions to complex condensed-phase environments.[16, 17] Representative examples of each type of process are shown in Fig. 1.1.

Understanding these processes at a dynamical level is essential for explaining natural phenomena, designing functional materials, and ultimately predicting and controlling reaction pathways and rates.

The fundamental theoretical framework for describing the state and dynamics of such systems is quantum mechanics. In standard non-relativistic quantum mechanics, the state of a closed system is represented by a state vector $|\psi(t)\rangle$ in Hilbert space. Its time evolution is governed by the Schrödinger equation,

$$i\hbar\frac{d}{dt}|\psi(t)\rangle = \hat{H}|\psi(t)\rangle, \tag{1.1}$$

where $\hat{H}$ is the Hamiltonian operator of the system.

For a system of N particles, the wavefunction depends on $3N$ spatial coordinates and

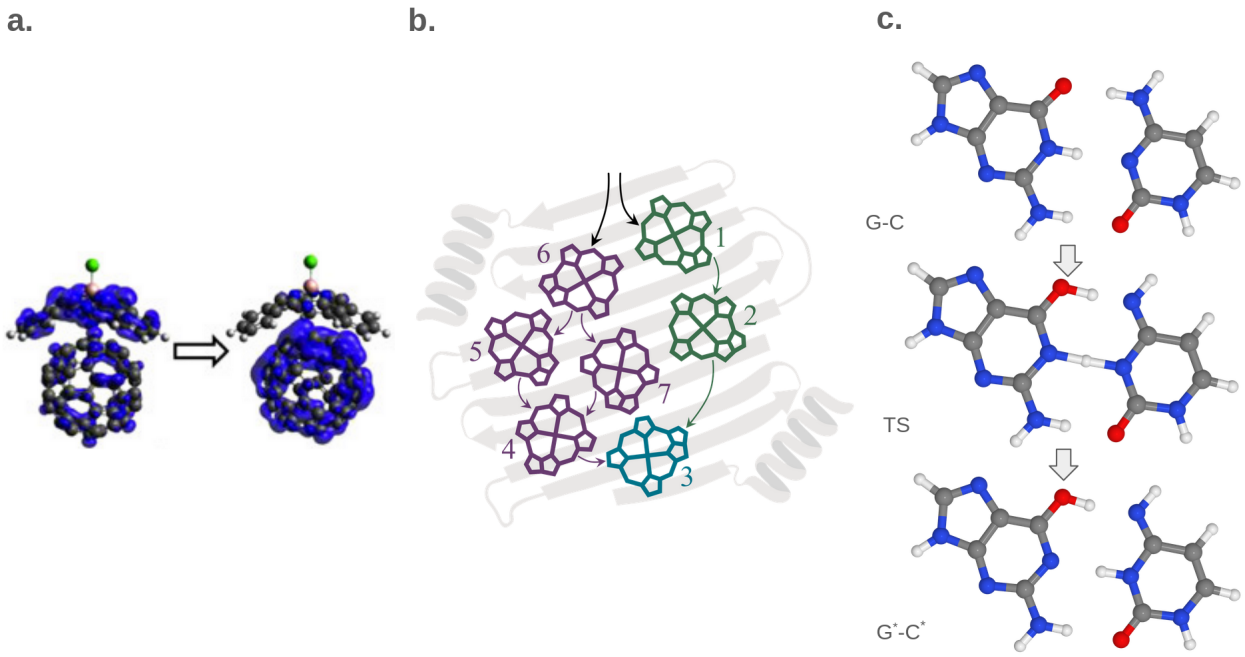


Figure 1.1: Representative examples of chemical dynamical processes considered in this thesis. (a) Electronic charge transfer in an organic photovoltaic system consisting of a subphthalocyanine donor and a fullerene acceptor. (b) Excitation energy transfer in the photosynthetic Fenna–Matthews–Olson (FMO) complex. (c) Proton transfer in a guanine–cytosine DNA base pair, proceeding from the canonical form G–C through the transition state (TS) to the tautomeric form G^*–C^*. Panel (a) is adapted with permission from Lee, M. H.; Geva, E.; Dunietz, B. D. *J. Phys. Chem. C* **2014**, *118* (18), 9780–9789. Copyright 2014 American Chemical Society. Panels (b) and (c) are adapted from Refs. 1 and 2, respectively, under CC BY 4.0 licenses

therefore resides in a high-dimensional configuration space. As the number of particles increases, the dimension of the corresponding Hilbert space grows rapidly, typically exponentially in standard many-body representations. Consequently, direct numerical integration of the Schrödinger equation becomes computationally infeasible for realistic chemical systems involving many coupled electronic and nuclear degrees of freedom.

This challenge motivates the development of alternative formulations that are better suited for describing high-dimensional systems. A more general description of quantum states is provided by the density operator formalism.[5, 18] For a closed system in a pure state, the density operator is defined as

$$\hat{\rho}(t) = |\psi(t)\rangle\langle\psi(t)|. \tag{1.2}$$

A density operator is characterized by the following properties:

$$\hat{\rho}^\dagger = \hat{\rho}, \tag{1.3}$$

$$\hat{\rho}_{jj} \geq 0, \tag{1.4}$$

$$\mathrm{Tr}[\hat{\rho}] = 1. \tag{1.5}$$

Hermiticity ensures real expectation values, positivity guarantees non-negative probabilities, and unit trace enforces normalization. A density operator of the form given in Eq. 1.2 represents a pure state and satisfies

$$\hat{\rho}^2 = \hat{\rho}, \qquad \mathrm{Tr}\left[\hat{\rho}^2\right] = 1. \tag{1.6}$$

More generally, a system may be described by a statistical ensemble of pure states,

$$\hat{\rho}(t) = \sum_i p_i(t)\, |\psi_i(t)\rangle\langle\psi_i(t)|, \qquad \sum_i p_i(t) = 1, \tag{1.7}$$

which corresponds to a mixed state characterized by

$$\hat{\rho}^2 \neq \hat{\rho}, \qquad \mathrm{Tr}\left[\hat{\rho}^2\right] < 1. \tag{1.8}$$

In many situations of practical interest, the system under study is not isolated but interacts with additional environmental, or bath, degrees of freedom. For a composite system consisting of a subsystem of interest coupled to a bath, the reduced density operator of the

subsystem is obtained by tracing over the bath degrees of freedom,

$$\hat{\sigma}(t) = \mathrm{Tr}_B \left\{ \hat{\rho}(t) \right\}. \tag{1.9}$$

Even if the total system evolves unitarily and remains in a pure state, the reduced density matrix of the subsystem generally becomes mixed due to entanglement with the bath. As the subsystem interacts with its environment, coherence between its states is degraded, leading to the suppression of off-diagonal elements in the reduced density matrix. This process, known as decoherence, underlies the effective non-unitary dynamics described by open quantum system theory.

Quantum master equations (QMEs) are equations that describe the time-evolution of the reduced density matrix and can capture the loss of coherences as the system interacts with the bath. The benefit of QMEs in relation to the Schrödinger equation is that the reduced density matrix can be picked to be a small subset of the total system which reduces the dimensionality of the problem compared to Schrödinger evolution of the total composite system. Rigorous derivation of quantum master equations starts with the equation of motion of the composite system, the Liouville equation

$$\frac{\mathrm{d}}{\mathrm{d}t}\hat{\rho}(t) = -\frac{i}{\hbar}\left[H, \hat{\rho}(t)\right] = \mathcal{L}\hat{\rho}(t), \tag{1.10}$$

where $\mathcal{L}$ is the Liouvillian super-operator. One can then use a projection-operator,

$$\mathcal{P}\hat{A} = \hat{\rho}_B(0) \otimes \mathcal{P}_e \,\mathrm{Tr}_B\{\hat{A}\}, \qquad \mathcal{Q} = \mathcal{I} - \mathcal{P}, \tag{1.11}$$

here $\mathcal{P}_e$ projects onto the electronic states of interest, we use the full density matrix here $\mathcal{P}_e = 1$. This yields the exact Nakajima–Zwanzig equation for the reduced density matrix of the system[19, 20, 21, 22]

$$\frac{d}{dt}\hat{\sigma}(t) = -\frac{i}{\hbar}\langle\mathcal{L}\rangle\hat{\sigma}(t) - \int_0^t d\tau\, \mathcal{K}(\tau)\hat{\sigma}(t-\tau)\,, \tag{1.12}$$

where

$$\langle\mathcal{L}\rangle(\cdot) = \mathrm{Tr}_B\{\hat{\rho}_B(0)\mathcal{L}\}(\cdot)\,, \tag{1.13}$$

$$\mathcal{K}(\tau) = \frac{1}{\hbar^2}\,\mathrm{Tr}_B\Big\{\mathcal{L}\, e^{-i\mathcal{Q}\mathcal{L}\tau/\hbar}\,\mathcal{Q}\mathcal{L}\,\hat{\rho}_B(0)\Big\}\,. \tag{1.14}$$

As exact calculations of memory kernels and Liouvillian are not available in closed-form, a number of perturbative methods have been developed. The first of which is the Redfield

QME. It takes the system-bath coupling as a perturbation and we present the approach here.[23]

One can split the Hamiltonian into the form of a zero-order Hamiltonian $\hat{H}_0 = \hat{H}_S + \hat{H}_B$ and interaction Hamiltonian taken as a weak perturbation $H_I = \hat{H}_{BS}$, one can expand to second-order to get a perturbative QME. Further, assuming the system's relaxation time is much slower than the decay of the memory kernel $\mathcal{K}(\tau)$ allows one to make a Markovian approximation such that one can obtain in the energy basis of the system

$$\begin{aligned}\frac{d}{dt}\hat{\sigma}_{jk}(t) = -i\omega_{jk}\,\hat{\sigma}_{jk}(t) - \sum_{m,n}\Gamma_{jn,mn}(\omega_{mn})\,\hat{\sigma}_{mk}(t) - \sum_{m,n}\Gamma^{*}_{km,mn}(\omega_{mn})\,\hat{\sigma}_{jn}(t) \\ + \sum_{m,n}\Gamma_{nk,jm}(\omega_{mj})\,\hat{\sigma}_{mn}(t) + \sum_{m,n}\Gamma^{*}_{mj,kn}(\omega_{nk})\,\hat{\sigma}_{mn}(t),\end{aligned} \tag{1.15}$$

where

$$\Gamma_{jk,mn}(\omega) = \frac{1}{\hbar^2}\int_0^\infty \mathrm{d}\tau e^{i\omega\tau} C_{jk,mn}(\tau), \tag{1.16}$$

here

$$C_{jk,mn}(\tau) = \mathrm{Tr}_B(\hat{\rho}_B^{eq}(0)\hat{\Lambda}_{jk}(\tau)\hat{\Lambda}_{mn}) \tag{1.17}$$

The terms $\hat{\Lambda}_{jk}$ are off-diagonal bath operators involved in the system-bath coupling. The EOM in Eq. 1.15 is known as the Redfield equation. Finally, another QME of practical interest is the Lindblad equation,[18] the Redfield equation can be cast in Lindblad form by making the secular approximation where $C_{jk,mn}(\tau) = \delta(j,n)\delta(k,m)C_{jk,kj}(\tau)$ so that

$$\frac{d}{dt}\hat{\sigma}(t) = -\frac{i}{\hbar}\Big[\hat{H}_S + \hat{H}_{\mathrm{LS}},\,\hat{\sigma}(t)\Big] + \sum_{j,k}\gamma_{jk}\left(\hat{L}_{jk}\,\hat{\sigma}(t)\,\hat{L}_{jk}^{\dagger} - \frac{1}{2}\left\{\hat{L}_{jk}^{\dagger}\hat{L}_{jk},\,\hat{\sigma}(t)\right\}\right). \tag{1.18}$$

Here we define $L_{jk} = |j\rangle\langle k|$, $\gamma_{jk} = 2\,\mathrm{Re}\,\Gamma_{jk,kj}(\omega_{jk})$, and $\hat{H}_{\mathrm{LS}}$ is the Lamb shift Hamiltonian obtained from the imaginary part of $\Gamma_{jk,kj}(\omega_{jk})$. We utilize a Lindblad QME in Chapter 4 to describe dissipative dynamics produced by the coupling of a bosonic quantum device to its surrounding environment.

The next quantum master equation we will consider is known as the population-only off-diagonal quantum master equation.[24, 25] This quantum master equation starts with the Shibata QME, we use the projection operator in Eq. 1.11 and move to the interaction

picture where

$$\tilde{\rho}(t) = e^{\frac{i}{\hbar}\hat{H}_0 t}\hat{\rho}(t)e^{-\frac{i}{\hbar}\hat{H}_0 t}, \tag{1.19}$$

$$\tilde{H}_I(t) = e^{\frac{i}{\hbar}\hat{H}_0 t}\hat{H}_I e^{-\frac{i}{\hbar}\hat{H}_0 t}, \tag{1.20}$$

$$\frac{\mathrm{d}}{\mathrm{d}t}\tilde{\rho}(t) = -\frac{i}{\hbar}\left[\tilde{H}_I(t), \tilde{\rho}(t)\right]. \tag{1.21}$$

The Shibata equation obtained in the interaction picture using the projection operator

$$\frac{\mathrm{d}}{\mathrm{d}t}\tilde{\sigma}_{\mathcal{P}}(t) = -\frac{i}{\hbar}\langle\mathcal{L}_I(t)\rangle_{\mathcal{P}}\tilde{\sigma}_{\mathcal{P}}(t) - \int_0^t d\tau\, \mathcal{K}_{\mathcal{P}}(t,\tau)\tilde{\sigma}_{\mathcal{P}}(t)\,, \tag{1.22}$$

where $\tilde{\sigma}_{\mathcal{P}}(t) = \mathcal{P}_e\tilde{\sigma}(t)$ and

$$\langle\mathcal{L}_I(t)\rangle_{\mathcal{P}} = \mathcal{P}_e\,\mathrm{Tr}_B[\mathcal{L}_I(t)\,\hat{\rho}_B(0)]\,, \tag{1.23}$$

$$\mathcal{K}_{\mathcal{P}}(t,\tau) = \frac{1}{\hbar^2}\mathcal{P}_e\,\mathrm{Tr}_B[\mathcal{L}_I(t)\,\mathcal{Q}\,\mathcal{L}_I(\tau)\,\hat{\rho}_B(0)]\,. \tag{1.24}$$

We choose here only electronic populations $\mathcal{P}_e\hat{\zeta} = \sum_j |j\rangle\langle j|\langle j|\hat{\zeta}|j\rangle$ and expand to second-order in $\mathcal{L}_I(t)$ with

$$\hat{H}_0 = \sum_j \hat{H}_j\,|j\rangle\langle j|, \tag{1.25}$$

$$\hat{H}_I = \sum_{jk} \hat{V}_{jk}\,|j\rangle\langle k|, \tag{1.26}$$

Where $\hat{H}_j$ is the Hamiltonian in diabatic electronic state $|j\rangle$ and $\hat{V}_{jk}$ are electronic coupling terms between electronic states. From this, we can obtain

$$\frac{d}{dt}\tilde{\sigma}_{jj}(t) = -\sum_{k\neq j} k'_{kj}(t)\,\tilde{\sigma}_{jj}(t) + \sum_{k\neq j} k'_{jk}(t)\,\tilde{\sigma}_{kk}(t), \tag{1.27}$$

$$k'_{jk}(t) = \frac{2}{\hbar^2}\,\mathrm{Re}\int_0^t d\tau\ \left\langle \hat{V}_{kj}(t)\,\hat{V}_{jk}(\tau)\right\rangle. \tag{1.28}$$

In Chapter 2, we implement and study this equation-of-motion for a photoexcited charge transfer reaction in carotenoid-porphyrin-C_{60} molecular triad dissolved in tetrahydrofuran.

1.2 Simulating Quantum Dynamics on Classical Devices

1.2.1 Classical Representation of Quantum States

For a closed quantum system described by a wavefunction $|\psi(t)\rangle$, the state resides in a Hilbert space. We assume a finite-dimensional Hilbert space of dimension d,

$$|\psi(t)\rangle \in \mathcal{H}, \qquad \dim(\mathcal{H}) = d. \tag{1.29}$$

Once a basis is chosen, the state is represented by a complex vector of length d, requiring storage of d complex amplitudes on a classical device. For many-body systems, however, the dimension d itself typically grows exponentially with the number of degrees of freedom, leading to an exponential growth in classical memory requirements.[26]

If instead one works in the density operator formulation, the state is described by a linear operator acting on $\mathcal{H}$,

$$\hat{\rho}(t) \in \mathcal{B}(\mathcal{H}), \tag{1.30}$$

where $\mathcal{B}(\mathcal{H})$ denotes the space of linear operators on $\mathcal{H}$. This operator space has dimension

$$\dim\Big(\mathcal{B}(\mathcal{H})\Big) = d^2, \tag{1.31}$$

so storing the density operator on a classical device requires d^2 complex numbers, corresponding to a $d \times d$ matrix representation.

Consequently, while the density operator formalism is essential for describing open quantum systems, it further increases the classical memory cost relative to the state-vector representation. For many-body systems where d scales exponentially with system size, the storage requirements for $\hat{\rho}(t)$ scale as d^2, compounding the computational challenge.

1.2.2 Classical Time-Evolution of Quantum States

Classical simulation of quantum dynamics reduces to the numerical integration of the equations of motion governing the state. For closed systems, the Schrödinger equation, Eq. 1.1, may be treated as a standard initial value problem. General-purpose integration schemes such as Euler and Runge–Kutta methods can be applied directly. These solvers are flexible and can treat linear or nonlinear, autonomous or nonautonomous systems.

However, it is often advantageous to exploit the structure of the Schrödinger equation.

Formally, the solution may be written[6, 27]

$$|\psi(t)\rangle = \Phi(t)|\psi(0)\rangle, \tag{1.32}$$

where $\Phi(t)$ is the propagator. In general,

$$\Phi(t) = \exp\Big(\Omega(t)\Big), \tag{1.33}$$

with $\Omega(t)$ given by the Magnus expansion. When the Hamiltonian is time-independent, $\hat{H}(t) = \hat{H}$, the solution simplifies to the matrix exponential

$$|\psi(t)\rangle = \exp\left(-\frac{i}{\hbar}\hat{H}t\right)|\psi(0)\rangle. \tag{1.34}$$

Numerical propagation then reduces to approximating the action of this exponential on the state. One widely used approach is the split-operator Fourier transform (SOFT) method. If the Hamiltonian can be decomposed as $\hat{H} = \hat{T} + \hat{V}$, short-time evolution over a step Δt may be approximated via a Trotter decomposition,

$$|\psi(t_i + \Delta t)\rangle \approx e^{-\frac{i}{\hbar}\hat{V}\frac{\Delta t}{2}} e^{-\frac{i}{\hbar}\hat{T}\Delta t} e^{-\frac{i}{\hbar}\hat{V}\frac{\Delta t}{2}} |\psi(t_i)\rangle. \tag{1.35}$$

Such methods preserve unitarity at each time step while exploiting the structure of the propagator.

For open quantum systems, the equations of motion for the reduced density matrix must be integrated. In the Markovian case,

$$\dot{\rho} = \mathcal{L}\rho, \tag{1.36}$$

the solution takes the exponential form

$$\rho(t) = \exp(\mathcal{L}t)\rho(0). \tag{1.37}$$

Here, the matrix exponential may be computed directly, approximated, or evaluated via diagonalization of $\mathcal{L}$.

In the non-Markovian case, where the dynamics contain time-convolution terms, the evolution must be computed using numerical quadrature of the memory integral, leading to history-dependent integro-differential equations. In all cases, the computational cost is governed by the dimension d (or d^2 in the density matrix formulation), which grows rapidly with system size.

1.3 Simulating Quantum Dynamics on Quantum Devices

1.3.1 Quantum Representation of Quantum States

The exponential scaling discussed above arises from the need to explicitly store all amplitudes of the quantum state in classical memory. Quantum hardware offers a fundamentally different representation.[28]

A quantum system with n degrees of freedom (DOF) spans a Hilbert space

$$\mathcal{H} = \bigotimes_{k=1}^{n} \mathcal{H}_k, \qquad \dim(\mathcal{H}) = N^n, \tag{1.38}$$

where $N = \dim(\mathcal{H}_k)$ is the dimension associated with each degree of freedom. For a qubit, $N = 2$; for a qudit, N is finite; and for a bosonic mode, $\mathcal{H}_k$ is infinite-dimensional.[3]

Unlike classical simulation, which stores the N^n complex amplitudes explicitly as elements of a data structure, a quantum device physically realizes this tensor-product Hilbert space. The amplitudes are encoded in the physical state of the device rather than stored explicitly in classical memory.

Thus, while classical simulation represents a state as a vector in $\mathbb{C}^{N^n}$, a quantum processor represents the same state as a physical configuration of n interacting subsystems. The physical resource requirement scales linearly in the number of subsystems, even though the underlying Hilbert space dimension grows exponentially.

Time evolution of a closed quantum system is implemented through unitary operations. Since a Hamiltonian $\hat{H}$ is Hermitian, the propagator

$$U(t) = e^{-i\hat{H}t/\hbar} \tag{1.39}$$

is unitary. Digital quantum devices realize unitary transformations through sequences of native gates drawn from a universal gate set. By decomposing $U(t)$ into such elementary operations, the quantum processor approximates time evolution within the physical Hilbert space.

In contrast, analog quantum simulators implement dynamics by engineering a physical Hamiltonian whose natural evolution approximates that of the target system. In such devices, time evolution occurs continuously according to

$$|\psi(t)\rangle = e^{-i\hat{H}_{\text{device}}t/\hbar}|\psi(0)\rangle, \tag{1.40}$$

without explicit circuit decomposition. Examples include trapped-ion platforms[29, 30, 31]

and superconducting bosonic systems such as Kerr-type nonlinear oscillators,[32, 33, 34, 35, 36] where the device Hamiltonian is designed to emulate the desired model and does so with tunable parameters.[37, 38]

The evolution of a closed quantum system is generated by a Hermitian Hamiltonian and is therefore unitary. In contrast, open-system dynamics arising from coupling to environmental degrees of freedom is generally non-unitary when viewed as an effective evolution on the system Hilbert space. For linear quantum master equations, the generator does not possess the anti-Hermitian structure required to produce a unitary propagator. Consequently, the formal solution defines a non-unitary evolution operator that cannot be directly implemented within the unitary gate model of digital quantum computation.

Digital quantum devices realize only unitary transformations. Consequently, the simulation of non-unitary dynamics requires embedding the effective propagator into a larger unitary operation acting on an extended Hilbert space. Two principal strategies are commonly employed: linear combination of unitaries (LCU) constructions and unitary dilation methods.

In the LCU framework, a non-unitary operator M is expressed as a weighted sum of unitary operators,

$$M = \sum_j \alpha_j U_j, \tag{1.41}$$

where U_j are unitary matrices and α_j are complex coefficients. The implementation proceeds by introducing an ancilla register that encodes the coefficients α_j, followed by applications of the unitaries U_j acting on the joint system–ancilla Hilbert space.[39, 40, 41]

An alternative approach is unitary dilation. In this strategy, the operator M is embedded directly into a larger unitary matrix acting on the tensor product of the system and an ancilla. The desired non-unitary evolution appears as a sub-block of the enlarged unitary.

A particularly transparent example is provided by the Sz.-Nagy dilation of a contraction.[42] Given a matrix M satisfying $\|M\| \leq 1$, one may construct the unitary

$$U_M = \begin{pmatrix} M & \sqrt{I - MM^\dagger} \\ \sqrt{I - M^\dagger M} & -M^\dagger \end{pmatrix}. \tag{1.42}$$

Acting on an initial vector of the form $(v, 0)^{\mathrm{T}}$ yields

$$U_M \begin{pmatrix} v \\ 0 \end{pmatrix} = \begin{pmatrix} Mv \\ v' \end{pmatrix}, \tag{1.43}$$

where v' lies in the ancilla subspace. The action of M on the system is therefore recovered by restricting attention to the system component of the enlarged state. In this way, non-unitary evolution on the system Hilbert space is realized as part of a unitary transformation on a composite space.[43, 44, 45]

Several dilation constructions have been developed, including Stinespring dilation,[46, 47, 48] Sz.-Nagy dilation, and singular-value-decomposition (SVD) based embeddings.[49, 50] These approaches differ in how the enlarged unitary is constructed and in their circuit realizations, but share the common principle that non-unitary operators can be implemented through unitary dynamics in an extended Hilbert space.

Analog quantum simulators offer a complementary perspective. In certain platforms, system–bath Hamiltonians can be engineered explicitly, allowing dissipative dynamics to emerge naturally from the unitary evolution of the full device.[51] In other architectures, dissipation is implemented through experimentally controllable interactions with auxiliary modes, resulting in an effective Lindblad description for the system.[35] The corresponding dissipative rates, such as friction coefficients or effective temperatures, can be adjusted through device parameters.[52] In such platforms, the physical hardware itself supplies the additional degrees of freedom that mediate the open-system dynamics.

Analog quantum computing provides a promising new frontier compared to semiclassical and mixed quantum–classical methods. Its key advantage is the ability to directly implement the quantum dynamics of the full chemical Hamiltonian in a scalable manner. In contrast, semiclassical approaches such as the linearized semiclassical (LSC) method[53, 54, 55, 56] and mapping-based methods like Meyer–Miller,[57, 58, 59, 60] as well as mixed quantum–classical approaches including the mixed quantum–classical Liouville (MQCL) method,[61, 62] Tully's surface hopping,[63, 64] and mean-field dynamics,[65, 66] rely on approximate treatments. In these approaches, certain degrees of freedom are treated classically, leading to approximations whose validity must be assessed on a case-by-case basis.

While analog quantum computers are typically limited to a narrower class of Hamiltonians than these more general methods, they offer a fundamentally different and potentially more accurate route for simulating quantum dynamics within this domain, opening a new avenue for chemical simulation.

In this work, we pursue digital and analog strategies for simulating chemical dynamics. On digital devices, we evolve the factors for the construction of unitary dilations of non-unitary propagators derived from quantum master equations. On the Kerr-cat analog platform, we engineer an effective controllable chemical double-well potential and exploit experimentally tunable dissipation to realize the target dynamics directly within the physical hardware.

1.4 Overview of the Dissertation

The remainder of this dissertation is organized as follows. In Chapter 2, we compute nonequilibrium Fermi's Golden Rule rate coefficients for a photoinduced charge-transfer reaction in the carotenoid–porphyrin–C_{60} (CPC_{60}) molecular triad dissolved in liquid tetrahydrofuran (THF), and apply the p-tcl-OD-QME framework outlined in Section 1.1 to simulate the population dynamics. In Chapter 3, we develop a quantum algorithm for the integration of a generic linear nonautonomous ordinary differential equation (ODE), using the cavity-free case of Chapter 2 as a testbed. In Chapter 4, we demonstrate how a bosonic quantum device can be tuned to approximate a chemical double-well potential and use it to simulate condensed-phase ground-state reactivity in several physically relevant chemical systems. Finally, Chapter 5 provides a summary of the dissertation and discusses the future directions of these research programs.

CHAPTER 2

Cavity-Modified Nonequilibrium Fermi's Golden Rule Rate Coefficients from Cavity-Free Inputs

2.1 Statement of Collaboration

This work was conducted in collaboration with Professor Eitan Geva. Professor Geva provided overall supervision of the research, guidance on the scientific direction of the project, and editorial feedback on the manuscript.

All theoretical development, analytical derivations, numerical implementation, data generation, analysis, and preparation of the initial manuscript draft were carried out by Pouya Khazaei.

This chapter is based on the following published work:

Khazaei, P.; Geva, E. Cavity-Modified Nonequilibrium Fermi's Golden Rule Rate Coefficients from Cavity-Free Inputs. *The Journal of Chemical Physics* **2025**, 163 (24), 244116. https://doi.org/10.1063/5.0300893.

2.2 Introduction

Charge transfer (CT) in donor-acceptor molecular systems represents an important class of chemical reactions.[67, 68, 69, 70, 71] They can occur spontaneously, as in redox reactions, or induced by electron injection, as in electrochemical devices, or by photoexcitation, as in photochemical and photovoltaic devices.[72, 73, 74, 75, 76, 77, 78, 79, 80, 10, 81, 82, 83, 84, 85, 86, 87, 88, 89] In the case of photoexcitation from the ground electronic state to an excited bright donor state, the nuclear degrees of freedom (DOF) start out in a nonequilibrium initial state. For example, in the case of impulsive excitation, the initial state of the nuclear DOF would correspond to equilibrium on the ground state potential energy surface (PES), which is typically significantly different from that corresponding to equilibrium on the excited donor PES.

A convenient way for describing the rate of photoinduced CT that starts out at the aforementioned nonequilibrium initial state is via the nonequilibrium Fermi's golden rule (NE-FGR).[90, 91, 92, 54, 93, 94, 95] Similarly to equilibrium FGR (E-FGR),[96, 97, 98, 99, 100, 67, 71, 79, 101, 71, 102, 103, 104, 10, 81, 105] NE-FGR is based on the assumption of weak electronic coupling between donor and acceptor states (within the framework of second-order time-dependent perturbation theory). However, unlike E-FGR, NE-FGR allows for an arbitrary nonequilibrium initial state of the nuclear DOF and is able to capture the transient nonequilibrium dynamics prior to establishing E-FGR rate kinetics. This is manifested by the fact that NE-FGR describes the CT dynamics in terms of a time-dependent rate coefficient, as opposed to a time-independent rate constant. It should also be noted that NE-FGR is not limited to CT processes, and can be applied to other types of electronic transitions, such as electronic excitation energy transfer processes.[106]

NE-FGR is based on assuming that the dynamics of the nuclear DOF is governed by quantum mechanics. However, a fully quantum-mechanical calculation of NE-FGR rates is only possible when the donor and acceptor PESs are parabolic. For those cases, the fully quantum-mechanical expression for the NE-FGR can be obtained in closed form and calculated in a feasible manner.[96, 71, 107, 108, 90, 109, 92, 110, 80, 10, 81] It should also be noted that the case of shifted, but otherwise identical, parabolic donor and acceptor PESs and constant donor-acceptor electronic coupling (the Condon approximation) corresponds to the canonical Marcus model for CT.[111, 112, 113] Calculating NE-FGR CT rates for complex systems described by anharmonic force fields, for which a quantum-mechanically exact calculation of the NE-FGR is not feasible, can be accomplished by utilizing semiclassical approximations.[54, 93, 94]

Recent experimental work has demonstrated that coupling the molecular electronic and vibrational DOF to the electromagnetic field modes of a microcavity can modify a wide range of chemical phenomena, including chemical reactivity and selectivity, photochemistry, catalysis, and electronic energy and charge transfer. [114, 115, 116, 117, 118, 119, 120, 121, 122, 123] Those experimental advances call for the development of theoretical models for estimating such cavity-induced modifications. Most recent theoretical studies of molecular matter in cavities assume that strong coupling between the molecular system and cavity modes is necessary for a significant cavity-induced effect to occur. The resulting strong-coupling models necessitate incorporating the cavity DOF into the model and explicitly simulating the molecular system inside the cavity. [124, 125, 126, 127, 128, 129, 130, 131, 132, 133, 134, 135, 136, 137, 138, 139]

However, even relatively weak coupling between molecular and cavity DOF can give rise to significant cavity-enabled effects. This is particularly true in the case of electronic energy

and CT processes whose kinetics can be described in terms of FGR, which is based on treating the coupling between electronic states as a small perturbation. Coupling between the electronic DOF and cavity modes can modify the coupling between electronic states when the molecular system is placed inside a cavity. Treating this additional electronic coupling as a small perturbation can therefore still give rise to significant modifications of the corresponding FGR-based rates.

In a recent paper,[140] we pursued such an approach to show how cavity-modified E-FGR rate constants can be estimated from inputs obtainable exclusively from a simulation of the cavity-free molecular system, thereby bypassing the need for an explicit simulation of the molecular system inside the cavity. We also demonstrated the usefulness of this framework in the case where the cavity-free kinetics is governed by Marcus theory, which corresponds to a semiclassical limit of E-FGR.

In this chapter, we extend the work in Ref. 140 to the case of the NE-FGR. We show that, similarly to the E-FGR case, the NE-FGR rate can be calculated from the same cavity-free inputs used for calculating the corresponding cavity-free NE-FGR rate for the same molecular system. This in turn allows us to bypass the need for an explicit simulation of the molecular system inside the cavity in order to estimate cavity-induced modifications. We also introduce an approximation of the cavity-modified NE-FGR, which we denote cavity-modified Instantaneous Marcus Theory (IMT), since it is based on the same assumptions underlying Marcus theory.

The remainder of this chapter is organized as follows. The theoretical framework for calculating cavity modified NE-FGR rates is presented and its asymptotic behavior analyzed in Sec. 2.3. In Sec. 2.4, the proposed framework is used to calculate cavity-modified NE-FGR CT rates in the photoexcited carotenoid-porphyrin-C_{60} (CPC_{60}) molecular triad dissolved in liquid tetrahydrofuran (THF). [141, 95, 104] Another application to the benchmark Garg-Onuchic-Ambegaokar (GOA) model for CT in the condensed phase[142] is provided in Sec. 2.5, which also considers the effect of temperature and friction. A summary of the main results and concluding remarks are provided in Sec. 2.6.

2.3 Theory

2.3.1 Preliminary considerations

Adopting the same terminology as in Ref. 140, we consider a donor-acceptor molecular system that can undergo electronic CT, which is placed inside an electromagnetic cavity.

The Hamiltonian of the system under consideration has the following form:

$$\hat{H} = \hat{H}_D^{np} |D\rangle\langle D| + \hat{H}_A^{np} |A\rangle\langle A| + \hat{V}_{DA}^{np}[|D\rangle\langle A| + |A\rangle\langle D|] \quad . \tag{2.1}$$

Here, $\hat{H}_j^{np}$ is the Hamiltonian of the nuclear (denoted by the superscript n) and photonic (denoted by the superscript p) DOF when the system is in the diabatic electronic state $|j\rangle$, where $j = D, A$ (D and A correspond to the donor and acceptor diabatic states, respectively):

$$\hat{H}_j^{np} = \hat{H}_j^n + \hat{H}^p \quad . \tag{2.2}$$

It should be noted that $\hat{H}_j^{np}$ consists of a sum of a purely nuclear Hamiltonian, $\hat{H}_j^n$, which is electronic-state specific (i.e. dependent on j), and a purely photonic term, $\hat{H}^p$, which is the same regardless of the electronic state (i.e. independent of j). $\hat{V}_{DA}^{np}$ in the second term in Eq. 2.1 is the coupling between the donor and acceptor states, which also consists of a sum of a purely nuclear and a purely photonic terms:

$$\hat{V}_{DA}^{np} = \hat{V}_{DA}^n + \hat{V}_{DA}^p \quad . \tag{2.3}$$

The explicit forms of $\hat{H}_D^n$, $\hat{H}_A^n$, $\hat{H}^p$, $\hat{V}_{DA}^n$ and $\hat{V}_{DA}^p$ are model-specific. Explicit examples for specific models will be presented below. However, for now, the derivation will remain general so as to be applicable to any form those operators may take.

Focusing on the case where CT occurs between a photoexcited bright donor electronic state and a dark acceptor electronic state, the initial state of the overall system is assumed to be given by a density operator of the form:

$$\hat{\rho}(0) = \hat{\rho}_B(0) \otimes |D\rangle\langle D| \quad . \tag{2.4}$$

Here, $\hat{\rho}_B(0)$ is the initial state of the bath, which in our case consists of the nuclear and photonic DOF. Further assuming that the initial state was created by impulsive photoexcitation from the ground state to an excited donor state, $\hat{\rho}_B(0)$ corresponds to the nuclear and photonic DOF being in thermal equilibrium with respect to the ground electronic state whose Hamiltonian is given by $\hat{H}_G^{np} = \hat{H}_G^n + \hat{H}^p$ (where $\hat{H}_G^n$ is assumed to be significantly different than $\hat{H}_D^n$):

$$\hat{\rho}_B(0) = \hat{\rho}_n(0) \otimes \hat{\rho}_p(0) = \frac{e^{-\beta \hat{H}_G^n}}{\mathrm{Tr}_n\left[e^{-\beta \hat{H}_G^n}\right]} \otimes \frac{e^{-\beta \hat{H}^p}}{\mathrm{Tr}_p\left[e^{-\beta \hat{H}^p}\right]} \quad . \tag{2.5}$$

2.3.2 Cavity-modified population-only off-diagonal quantum master equation and nonequilibrium Fermi's golden rule rates

In the next step, we cast the Hamiltonian in Eq. 2.1 in the form $\hat{H} = \hat{H}_0 + \hat{H}_I$, where the zero-order Hamiltonian, $\hat{H}_0$, and the interaction Hamiltonian, $\hat{H}_I$, are given by:

$$\hat{H}_0 = \hat{H}_D^{np} \left|D\right\rangle\!\left\langle D\right| + \hat{H}_A^{np} \left|A\right\rangle\!\left\langle A\right| \quad . \tag{2.6}$$

$$\hat{H}_I = \hat{V}_{DA}^{np}[\left|D\right\rangle\!\left\langle A\right| + \left|A\right\rangle\!\left\langle D\right|] \quad . \tag{2.7}$$

Treating $\hat{H}_I$ as a small perturbation within the framework of second-order perturbation theory and using projection operator techniques, one can derive the following equations of motion for the populations of the D and A states [$\sigma_{DD}(t)$ and $\sigma_{AA}(t)$, respectively):[24]

$$\frac{d}{dt}\sigma_{DD}(t) = -\frac{d}{dt}\sigma_{AA}(t) = -k_{D\to A}(t)\sigma_{DD}(t) + k_{A\to D}(t)\sigma_{AA}(t) \quad . \tag{2.8}$$

Adopting the same terminology as in Ref. 24, in what follows, we will refer to Eq. 2.8 as the population-only time-convolutionless off-diagonal quantum master equation (p-tcl-OD-QME). Within the p-tcl-OD-QME, $k_{j\to k}(t)$ is the NE-FGR rate coefficient for population transfer from state j to state k: [90, 91, 92, 54, 93, 94, 24]

$$\begin{aligned} &k_{j\to k}(t) = \\ &\frac{2}{\hbar^2}\,\mathrm{Re}\int_0^t \mathrm{d}\tau\ \mathrm{Tr}_B\left[e^{-\frac{i}{\hbar}\hat{H}_j^{np}t}\hat{\rho}_B(0)e^{\frac{i}{\hbar}\hat{H}_j^{np}t}\hat{V}_{jk}^{np}e^{-\frac{i}{\hbar}\hat{H}_k^{np}\tau}\hat{V}_{kj}^{np}e^{\frac{i}{\hbar}\hat{H}_j^{np}\tau}\right] \quad . \end{aligned} \tag{2.9}$$

Here, $\mathrm{Tr}_B[\cdot] = Tr_n Tr_p[\cdot]$ is the partial trace over the bath, which in our case corresponds to partially tracing over the nuclear and photonic Hilbert spaces.

It should be noted that the quantum master equation in Eq. 2.8 relies on a certain choice of projection operator and the procedure used for deriving it. Other quantum master equations can be derived based on other choices of projection operators and following alternative procedures, which are not convolutionless and account for the dynamics of the coherences in addition to that of the populations (e.g., see Refs. 18, 143, 24 for a more detailed discussion). In what follows, we choose to focus on the p-tcl-OD-QME due to its relative simplicity compared to the other aforementioned variations and the fact that the dynamics is insensitive to the choice of equation for the parameter range characteristic of CT reactions.[18]

Inserting Eqs. 2.2 and 2.3 into Eq. 2.9, we obtain the following expression for the

integrand on the R.H.S. of Eq. 2.9:

$$
\begin{aligned}
&\mathrm{Tr}_B\left[e^{-\frac{i}{\hbar}\hat{H}_j^{np}t}\hat{\rho}_B(0)e^{\frac{i}{\hbar}\hat{H}_j^{np}t}\hat{V}_{jk}^{np}e^{-\frac{i}{\hbar}\hat{H}_k^{np}\tau}\hat{V}_{kj}^{np}e^{\frac{i}{\hbar}\hat{H}_j^{np}\tau}\right]\\
&=\mathrm{Tr}_n\left[e^{-\frac{i}{\hbar}\hat{H}_j^{n}t}\hat{\rho}_n(0)e^{\frac{i}{\hbar}\hat{H}_j^{n}t}\hat{V}_{jk}^{n}e^{-\frac{i}{\hbar}\hat{H}_k^{n}\tau}\hat{V}_{kj}^{n}e^{\frac{i}{\hbar}\hat{H}_j^{n}\tau}\right]\\
&\mathrm{Tr}_p\left[e^{-\frac{i}{\hbar}\hat{H}^{p}t}\hat{\rho}_p(0)e^{\frac{i}{\hbar}\hat{H}^{p}t}e^{-\frac{i}{\hbar}\hat{H}^{p}\tau}e^{\frac{i}{\hbar}\hat{H}^{p}\tau}\right]\\
&+\mathrm{Tr}_n\left[e^{-\frac{i}{\hbar}\hat{H}_j^{n}t}\hat{\rho}_n(0)e^{\frac{i}{\hbar}\hat{H}_j^{n}t}e^{-\frac{i}{\hbar}\hat{H}_k^{n}\tau}e^{\frac{i}{\hbar}\hat{H}_j^{n}\tau}\right]\\
&\mathrm{Tr}_p\left[e^{-\frac{i}{\hbar}\hat{H}^{p}t}\hat{\rho}_p(0)e^{\frac{i}{\hbar}\hat{H}^{p}t}\hat{V}^{p}e^{-\frac{i}{\hbar}\hat{H}^{p}\tau}\hat{V}^{p}e^{\frac{i}{\hbar}\hat{H}^{p}\tau}\right]\\
&+\mathrm{Tr}_n\left[e^{-\frac{i}{\hbar}\hat{H}_j^{n}t}\hat{\rho}_n(0)e^{\frac{i}{\hbar}\hat{H}_j^{n}t}\hat{V}_{jk}^{n}e^{-\frac{i}{\hbar}\hat{H}_k^{n}\tau}e^{\frac{i}{\hbar}\hat{H}_j^{n}\tau}\right]\\
&\mathrm{Tr}_p\left[e^{-\frac{i}{\hbar}\hat{H}^{p}t}\hat{\rho}_p(0)e^{\frac{i}{\hbar}\hat{H}^{p}t}\hat{V}^{p}e^{-\frac{i}{\hbar}\hat{H}^{p}\tau}e^{\frac{i}{\hbar}\hat{H}^{p}\tau}\right]\\
&+\mathrm{Tr}_n\left[e^{-\frac{i}{\hbar}\hat{H}_j^{n}t}\hat{\rho}_n(0)e^{\frac{i}{\hbar}\hat{H}_j^{n}t}e^{-\frac{i}{\hbar}\hat{H}_k^{n}\tau}\hat{V}_{kj}^{n}e^{\frac{i}{\hbar}\hat{H}_j^{n}\tau}\right]\\
&\mathrm{Tr}_p\left[e^{-\frac{i}{\hbar}\hat{H}^{p}t}\hat{\rho}_p(0)e^{\frac{i}{\hbar}\hat{H}^{p}t}e^{-\frac{i}{\hbar}\hat{H}^{p}\tau}\hat{V}^{p}e^{\frac{i}{\hbar}\hat{H}^{p}\tau}\right] \quad .
\end{aligned}
\tag{2.10}
$$

Importantly, according to Eq. 2.10, cavity-modified NE-FGR rate coefficients can be obtained from purely nuclear and purely photonic time correlation functions as inputs and therefore do not necessitate an explicit simulation of the molecular system inside the cavity. Furthermore, as we will show below, the purely photonic time correlation functions can be obtained in closed form, while the purely nuclear correlation functions can be obtained from cavity-free models. In other words, cavity-modified NE-FGR rate coefficients are obtainable from cavity-free inputs.

To further demonstrate the implications of the aforementioned separability between nuclear and photonic time correlation functions, consider the case where the molecular system is coupled to a single cavity mode[140] (the extension to multiple modes is straightforward and leads to additive contributions to the NE-FGR rate from each of the modes[144]):

$$
\hat{H}^p = \frac{\hat{p}_p^2}{2} + \frac{\omega_p^2\hat{q}_p^2}{2} \quad . \tag{2.11}
$$

Here, ω_p is the cavity mode's frequency, $\hat{q}_p$ is the photonic position operator and $\hat{p}_p$ is the photonic momentum operator. The electronic-photonic coupling in this case is given by[140]

$$
\hat{V}_{DA}^p = \sqrt{2\hbar\omega_p}g_p\hat{q}_p = G\hat{q}_p \quad . \tag{2.12}
$$

where,

$$
g_p = \sqrt{\frac{\mu_{DA}^2\omega_p}{2\hbar\epsilon_0 V}} \quad . \tag{2.13}
$$

Here, μ_{DA} is the donor-acceptor transition dipole moment and V is the volume of the cavity.

Given Eqs. 2.11 and 2.12, the photonic terms in Eq. 2.10 can be obtained in closed form:

$$\begin{aligned}
&\mathrm{Tr}_p\left[e^{-\frac{i}{\hbar}\hat{H}^p t}\hat{\rho}_p(0)e^{\frac{i}{\hbar}\hat{H}^p t}e^{-\frac{i}{\hbar}\hat{H}^p \tau}e^{\frac{i}{\hbar}\hat{H}^p \tau}\right] = 1 \quad , \\
&\mathrm{Tr}_p\left[e^{-\frac{i}{\hbar}\hat{H}^p t}\hat{\rho}_p(0)e^{\frac{i}{\hbar}\hat{H}^p t}\hat{V}^p e^{-\frac{i}{\hbar}\hat{H}^p \tau}e^{\frac{i}{\hbar}\hat{H}^p \tau}\right] = 0 \quad , \\
&\mathrm{Tr}_p\left[e^{-\frac{i}{\hbar}\hat{H}^p t}\hat{\rho}_p(0)e^{\frac{i}{\hbar}\hat{H}^p t}e^{-\frac{i}{\hbar}\hat{H}^p \tau}\hat{V}^p e^{\frac{i}{\hbar}\hat{H}^p \tau}\right] = 0 \quad , \\
&\mathrm{Tr}_p\left[e^{-\frac{i}{\hbar}\hat{H}^p t}\hat{\rho}_p(0)e^{\frac{i}{\hbar}\hat{H}^p t}\hat{V}^p e^{-\frac{i}{\hbar}\hat{H}^p \tau}\hat{V}^p e^{\frac{i}{\hbar}\hat{H}^p \tau}\right] \\
&= \frac{\hbar G^2}{2\omega_p}\cosh[\frac{\beta\hbar\omega_p}{2} - i\omega_p\tau]\,\mathrm{csch}[\frac{\beta\hbar\omega_p}{2}] \quad .
\end{aligned} \tag{2.14}$$

Substituting the identities in Eq. 2.14 back into Eq. 2.10, making the Condon approximation such that $\hat{V}^n_{jk} \to \Gamma$ (where Γ is a constant, as opposed to a nuclear operator), and substituting the result back into Eq. 2.9, the cavity modified NE-FGR rate coefficient can be cast in the following form:

$$k_{j\to k}(t) = \frac{2}{\hbar^2}\,\mathrm{Re}\int_0^t \mathrm{d}\tau\, C^p(\tau)C^n_{jk}(t,\tau) \quad . \tag{2.15}$$

where

$$C^n_{jk}(t,\tau) = \Gamma^2\,\mathrm{Tr}_n\left[e^{-\frac{i}{\hbar}\hat{H}^n_j t}\hat{\rho}_n(0)e^{\frac{i}{\hbar}\hat{H}^n_j t}e^{-\frac{i}{\hbar}\hat{H}^n_k \tau}e^{\frac{i}{\hbar}\hat{H}^n_j \tau}\right] \quad . \tag{2.16}$$

and

$$C^p(\tau) = 1 + \frac{\hbar G^2}{2\omega_p\Gamma^2}\cosh[\frac{\beta\hbar\omega_p}{2} - i\omega_p\tau]\,\mathrm{csch}[\frac{\beta\hbar\omega_p}{2}] \quad . \tag{2.17}$$

Here, $C^n_{jk}(t,\tau)$ captures the cavity-free nuclear dynamics and $C^p(\tau)$ captures the cavity effect. More specifically, decoupling the molecular system from the cavity mode, which corresponds to setting G to 0, implies that $C^p(\tau) \to 1$, such that $k_{j\to k}(t)$ reverts to the cavity-free NE-FGR rate coefficient:[90, 91, 92, 54, 93, 94]

$$k^m_{j\to k}(t) = \frac{2}{\hbar^2}\,\mathrm{Re}\int_0^t \mathrm{d}\tau\, C^n_{jk}(t,\tau) \quad . \tag{2.18}$$

Here, the superscript m refers to the fact that this is the NE-FGR rate coefficient for the cavity-free molecular system.

Further insight can be obtained by writing $C^p(\tau)$ in the following alternative, yet completely equivalent, form:

$$C^p(\tau) = 1 + \alpha\langle n_{eq}\rangle\left(e^{i\omega_p\tau} + e^{\beta\hbar\omega_p}e^{-i\omega_p\tau}\right) \quad . \tag{2.19}$$

Here,

$$\langle n_{eq} \rangle = \frac{1}{e^{\beta\hbar\omega_p} - 1} \quad . \tag{2.20}$$

is the average number of photons in the cavity mode in thermal equilibrium and

$$\alpha = \frac{G^2\hbar}{2\Gamma^2\omega_p} \quad . \tag{2.21}$$

Substituting Eq. 2.19 into Eq 2.15, we obtain:

$$\begin{aligned} k_{j\to k}(t) &= k^m_{j\to k}(t) \\ &\quad + \alpha\langle n_{eq}\rangle \left[k^m_{j\to k}(t,\omega_p) + e^{\beta\hbar\omega_p} k^m_{j\to k}(t,-\omega_p)\right] \quad . \end{aligned} \tag{2.22}$$

Here, $k^m_{j\to k}(t)$ is as in Eq. 2.18 and $k^m_{j\to k}(t,\pm\omega_p)$ is the NE-FGR rate coefficient for the dressed molecular system, where the PES of state j is shifted by $\pm\hbar\omega_p$:

$$\begin{aligned} k^m_{j\to k}(t,\pm\omega_p) &= \frac{2}{\hbar^2}\,\mathrm{Re}\int_0^t \mathrm{d}\tau\, e^{\pm i\omega_p\tau} C_n(t,\tau) \\ &= \frac{2}{\hbar^2}\,\mathrm{Re}\int_0^t \mathrm{d}\tau\ \mathrm{Tr}_n\left[e^{-\frac{i}{\hbar}(\hat{H}^n_j \pm\hbar\omega_p)t}\hat{\rho}_n(0) e^{\frac{i}{\hbar}(\hat{H}^n_j\pm\hbar\omega_p)t}\hat{V}^n_{jk} e^{-\frac{i}{\hbar}\hat{H}^n_k\tau}\hat{V}^n_{kj} e^{\frac{i}{\hbar}(\hat{H}^n_j\pm\hbar\omega_p)\tau}\right] \end{aligned} \tag{2.23}$$

2.3.3 Asymptotic behavior and cavity-modified instantaneous Marcus theory

Several limits of the cavity-modified NE-FGR rate coefficient in Eq. 2.22 are noteworthy. One such limit corresponds to the case where the CT dynamics can be described in terms of the E-FGR rate constant. This corresponds to the case where the nuclear DOF start out at equilibrium on the parent state's PES, i.e. $\hat{\rho}_n(0) = \hat{\rho}^{eq}_{n,j} = \frac{e^{-\beta\hat{H}^n_j}}{\mathrm{Tr}_n\left[e^{-\beta\hat{H}^n_j}\right]}$, which implies that

$$C^n_{jk}(t,\tau) \to C^n_{jk}(\tau) = \Gamma^2\,\mathrm{Tr}_n\left[\hat{\rho}^{eq}_{n,j} e^{-\frac{i}{\hbar}\hat{H}^n_k\tau} e^{\frac{i}{\hbar}\hat{H}^n_j\tau}\right] \quad . \tag{2.24}$$

such that:

$$k_{j\to k}(t) \to \frac{2}{\hbar^2}\,\mathrm{Re}\int_0^t \mathrm{d}\tau\, C^p(\tau) C^n_{jk}(\tau) \quad . \tag{2.25}$$

Further assuming that the lifetime of the correlation function $C^n_{jk}(\tau)$ is much shorter than the timescale of CT then allows one to extend the upper limit of the integral to infinity, such that it can be described by the E-FGR rate constant (as opposed to a time-dependent

NE-FGR rate coefficient):

$$k_{j\to k}^{eq} = \frac{2}{\hbar^2}\,\mathrm{Re}\int_0^\infty \mathrm{d}\tau\, C^p(\tau) C_{jk}^n(\tau) \tag{2.26}$$

A detailed analysis of the cavity-modified E-FGR rate constant in Eq. 2.26 has been recently reported in Ref. 140.

Another noteworthy limit of Eq. 2.22 is that of the Instantaneous Marcus Theory (IMT).[141, 95] To derive IMT, one starts with the short-time and high-temperature limit of the linearized semiclassical (LSC) approximation for the cavity-free NE-FGR rate coefficient:[94]

$$k_{j\to k}^{m}(t) \approx \frac{2}{\hbar^2}\Gamma^2\,\mathrm{Re}\int_0^t d\tau \left\langle \exp\left[\frac{i}{\hbar}U_{jk}(\mathbf{R}_t)\tau\right]\right\rangle \quad . \tag{2.27}$$

Here, $U_{jk}(\mathbf{R}_t) = V_j(\mathbf{R}_t) - V_k(\mathbf{R}_t)$, where $V_j(\mathbf{R})$ and $V_k(\mathbf{R})$ are the PESs of the j-th and k-th states, respectively, and $\left\langle \exp\left[\frac{i}{\hbar}U_{jk}(\mathbf{R}_t)\tau\right]\right\rangle$ corresponds to averaging $\exp\left[\frac{i}{\hbar}U_{jk}(\mathbf{R}_t)\tau\right]$ over classical trajectories of the nuclear DOF, $\{\mathbf{R}_t, \mathbf{P}_t\}$, whose initial state, $\{\mathbf{R}_0, \mathbf{P}_0\}$, is sampled from $\rho_n^{Cl}(0, \mathbf{R}_0, \mathbf{P}_0)$ [the classical limit of $\hat{\rho}_n(0)$] and whose dynamics is dictated by $V_j(\mathbf{R})$ (here, $\{\mathbf{R}, \mathbf{P}\}$ correspond to the nuclear coordinates and momenta which are treated as classical variables). IMT is obtained by assuming that the nuclear dynamics also satisfies Gaussian statistics. This translates into substituting $\left\langle \exp\left[\frac{i}{\hbar}U_{jk}(\mathbf{R}_t)\tau\right]\right\rangle$ with its second-order cumulant expansion.[145, 146] Since the time integral is over a Gaussian integrand in this case, $k_{j\to k}^m(t)$ can be given in terms of an error function (erf):

$$\begin{aligned} k_{j\to k}^{m,IMT}(t) =& \Gamma^2 \frac{\sqrt{2\pi}}{\sigma_{jk,t}}\,\mathrm{Re}\left(\mathrm{erf}\left[\frac{\sigma_{jk,t}^2\, t - i\hbar\,\langle U_{jk}\rangle_t}{\sqrt{2}\,\hbar\sigma_{jk,t}}\right]\right) \\ & \exp\left[-\frac{\langle U_{jk}(y_t)\rangle^2}{2\sigma_{U_{jk}(y_t)}^2}\right] \end{aligned} \tag{2.28}$$

where, $\langle U_{jk}\rangle_t = \langle U_{jk}(\mathbf{R}_t)\rangle$ and $\sigma_{jk,t}^2 = \langle U_{jk}^2(\mathbf{R}_t)\rangle - \langle U_{jk}(\mathbf{R}_t)\rangle^2$.

The IMT expression in Eq. 2.28 can be further simplified by setting the upper limit of the time integral in Eq. 2.27 to ∞. This is justified for times longer than the (typically rather short) lifetime of $\left\langle \exp\left[-\frac{i}{\hbar}U_{jk}(\mathbf{R}_t)\tau\right]\right\rangle$, and leads for the following expression for the IMT NE-FGR rate coefficient, which was previously reported and discussed in Refs. 141, 95:

$$k_{j\to k}^{m,LT-IMT}(t) = \frac{\Gamma^2}{\hbar}\sqrt{\frac{2\pi}{\sigma_{jk,t}^2}}\exp\left[-\frac{\langle U_{jk}\rangle_t^2}{2\sigma_{jk,t}^2}\right] \tag{2.29}$$

In what follows, we will refer to the IMT expression in Eq. 2.29 by LT-IMT, to denote that

it is the long-time (LT) limit of the IMT rate coefficient in Eq. 2.28. We also note that obtaining the cavity-modified IMT NE-FGR rate coefficients based on Eq 2.22, also requires calculating the IMT and LT-IMT approximations for $k^m_{j\to k}(t, \pm\omega_p)$, which can be obtained by replacing $\langle U_{jk}\rangle_t$ by $\langle U_{jk}\rangle_t \pm \hbar\omega_p$ in Eqs. 2.28 and 2.29.

It should be noted that the assumptions underlying IMT are expected to be valid for a wide range of chemical systems, as evidenced by the success of Marcus theory (which is based on similar assumptions). The IMT approximation is expected to be particularly useful in the case of complex molecular systems, for which there is no computationally feasible path for calculating the fully quantum-mechanical NE-FGR rates. For such systems, IMT, which can be calculated via classical molecular dynamics simulations, provides a feasible and accurate alternative. It should also be noted that the computational cost of integrating the p-tcl-OD-QME is significantly reduced when IMT rates are used. This is because the time integrals can be obtained in closed form in this case, thereby eliminating the need for numerical integration at each point in time.

2.4 Cavity-modified rates for photo-induced charge transfer in the Carotenoid-Porphyrin-C_{60} Triad dissolved in liquid Tetrahydrofuran

The next two sections provide demonstrative applications of the theoretical framework developed in Sec. 2.3 to model systems. We start out in this section, by demonstrating the effect of coupling to a cavity on photo-induced CT rates in the CPC_{60} molecular triad dissolved in liquid THF (CPC_{60}/THF, see Fig. 2.1).[104, 94, 95] We focus on the $\pi\pi^*$ $\rightarrow$CT1 transition in this system, where $\pi\pi^*$ is the bright non-CT Porphyrin-localized excited state (CP^*C_{60}) and CT1 is the dark excited CT state ($CP^+C^-_{60}$). To this end, we employ the three-state harmonic model that was developed for this system in Ref. 95. The triad is assumed to be in a bent conformation and to be impulsively photoexcited from the ground state to the $\pi\pi^*$ state, so that the initial nuclear configurations correspond to thermal equilibrium on the ground state PES. This choice is motivated by the fact that previous studies have found that the cavity-free $\pi\pi^*$ $\rightarrow$CT1 NE-FGR rate is significantly enhanced relative to that predicted by E-FGR.[94, 95] This enhancement was traced back to the nonequilibrium initial state of the nuclear DOF due to implusive photoexcitation from the ground state.[94, 95] In what follows, we investigate the effect of coupling to the cavity on the $\pi\pi^*$ $\rightarrow$CT1 NE-FGR transition rate in CPC_{60}/THF.

The results reported below were based on the following harmonic nuclear model Hamil-

tonians for the ground (CPC_{60}), donor (CP^*C_{60}) and acceptor ($CP^+C_{60}^-$) states:

$$\begin{aligned}
\hat{H}_D^n &= \hbar\omega_{DA} + \sum_{j=1}^{N}\left[\frac{1}{2}\hat{P}_j^2 + \frac{1}{2}\omega_j^2\hat{R}_j^2\right], \\
\hat{H}_A^n &= \sum_{j=1}^{N}\left[\frac{1}{2}\hat{P}_j^2 + \frac{1}{2}\omega_j^2(\hat{R}_j - R_j^{\mathrm{eq}})^2\right] \\
\hat{H}_G^n &= E_G + \sum_{j=1}^{N}\left[\frac{1}{2}\hat{P}_j^2 + \frac{1}{2}\omega_j^2(\hat{R}_j + S_j)^2\right]
\end{aligned} \tag{2.30}$$

Here, $\{\hat{R}_j, \hat{P}_j, \omega_j \,|\, j = 1, \ldots, N\}$ are the normal mode coordinates, momenta, and frequencies. $\{R_j^{\mathrm{eq}} \,|\, j = 1, \ldots, N\}$ and $\{S_j \,|\, j = 1, \ldots, N\}$ are the donor-to-acceptor and donor-to-ground shifts in the equilibrium geometry along the normal mode coordinates. The parameters E_G and $\hbar\omega_{DA}$ are shifts in equilibrium geometry energies of the ground state and donor state relative to the acceptor state, respectively.

The model Hamiltonians in Eq. 2.30 were parametrized in Ref. 95 based on inputs from all-atom molecular dynamics simulations. More specifically, the values of $\{\omega_j, R_j^{eq}, S_j\}$ we use here correspond to the ones obtained via the procedure referred to in Ref. 95 as model 2. The coupling strength to the cavity mode was set to $\hbar g_p = 10$meV, which is comparable to the cavity-free $\pi\pi^*$-CT1 electronic coupling coefficient, $V_{DA}^n = \Gamma = 24$meV, which was previously obtained from electronic structure calculations.[104, 94, 95] The cavity frequency was set to $\hbar\omega_p = 591$meV, which is the value that maximizes the cavity-induced enhancement of E-FGR for this system based on the procedure proposed in Ref. 140. Finally, $\hbar\omega_{DA}$ was set to 1014 meV[94, 95] and the temperature was set to 300K.

Importantly, $C_{jk}^n(t,\tau)$ can be obtained in closed form for the model under consideration:[24]

$$C_{DA}^n(t,\tau) = \Gamma^2 e^{i\omega_{DA}\tau}\exp\left(\sum_j \mathcal{F}_j^{(DA)}(t,\tau)\right), \tag{2.31}$$

$$\begin{aligned}
\mathcal{F}_j^{(DA)}(t,\tau) = \frac{-i\,R_j^{\mathrm{eq}}\,\omega_j}{\hbar\,\sinh\!\left(\frac{\beta\hbar\omega_j}{2}\right)}\sin\!\left(\frac{\tau\omega_j}{2}\right)\Bigg[R_j^{\mathrm{eq}}\,\sinh\!\left(\frac{\beta\hbar - i\tau}{2}\,\omega_j\right) \\
+ S_j\left(\sinh\!\left(\frac{\beta\hbar - i(t-\tau)}{2}\,\omega_j\right) + \sinh\!\left(\frac{\beta\hbar + i(t-\tau)}{2}\,\omega_j\right)\right)\Bigg].
\end{aligned}$$

$$C_{AD}^{n}(t,\tau) = \Gamma^2 e^{-i\omega_{DA}\tau} \exp\left(\sum_j \mathcal{F}_j^{(AD)}(t,\tau)\right), \tag{2.32}$$

$$\mathcal{F}_j^{(AD)}(t,\tau) = \frac{i\, R_j^{\mathrm{eq}}\, \omega_j}{\hbar\, \sinh\!\left(\frac{\beta\hbar\omega_j}{2}\right)} \sin\!\left(\frac{\tau\omega_j}{2}\right) \Bigg[-\, R_j^{\mathrm{eq}}\, \sinh\!\left(\frac{\beta\hbar - i\tau}{2}\,\omega_j\right) + (R_j^{\mathrm{eq}} + S_j)\left(\sinh\!\left(\frac{\beta\hbar - i(t-\tau)}{2}\,\omega_j\right) + \sinh\!\left(\frac{\beta\hbar + i(t-\tau)}{2}\,\omega_j\right)\right)\Bigg].$$

The main quantities that determine the IMT rates can also be obtained in closed form:

$$\langle U_{DA}\rangle_t = \hbar\omega_{DA} - \sum_j \left[\frac{1}{2}\omega_j^2 \left(R_j^{\mathrm{eq}}\right)^2 + \omega_j^2 R_j^{\mathrm{eq}} S_j \cos\left(\omega_j t\right)\right] \tag{2.33}$$

$$\langle U_{AD}\rangle_t = -\hbar\omega_{DA} + \sum_j \left[\omega_j^2 R_j^{\mathrm{eq}} \left(R_j^{\mathrm{eq}} + S_j\right) \cos\left(\omega_j t\right) - \frac{1}{2}\omega_j^2 \left(R_j^{\mathrm{eq}}\right)^2\right] \tag{2.34}$$

$$\sigma_{DA,t}^2 = \sigma_{AD,t}^2 = \sum_{j=1}^{N} \frac{\omega_j^2 \left(R_j^{\mathrm{eq}}\right)^2}{\beta} \tag{2.35}$$

Finally, we note that closed-form expressions for the donor-to-acceptor E-FGR rate constant, $k_{D\to A}^{eq}$, can be found in Ref. 140, and that $k_{A\to D}^{eq}$ can be obtained from $k_{D\to A}^{eq}$ by using detailed balance, $k_{A\to D}^{eq} = \exp(-\beta\hbar\omega_{DA}) k_{D\to A}^{eq}$.

The effect of coupling to the cavity on the $\pi\pi^* \to$ CT1 CT dynamics in CPC_{60}/THF simulated based on the p-tcl-OD-QME, Eq. 2.8, is shown in Fig. 2.1. The lower panel of this figure depicts the population of the donor state as a function of time, $P_D(t)$, while the middle panel shows the CT rate coefficient as a function of time, $k_{D\to A}(t)$.

A close inspection of Fig. 2.1 gives rise to several noteworthy observations. First, both cavity-free and cavity-modified NE-FGR rate coefficients, $k_{D\to A}(t)$, reach a plateau following a nonequilibrium transient period, with the plateau value given by the corresponding E-FGR rate constant. This is the expected behavior in condensed-phase systems, where the nonequilibrium initial state equilibrates (often on a time scale comparable to that of CT). Since the effect of the cavity on the E-FGR rate constant was already reported and analyzed

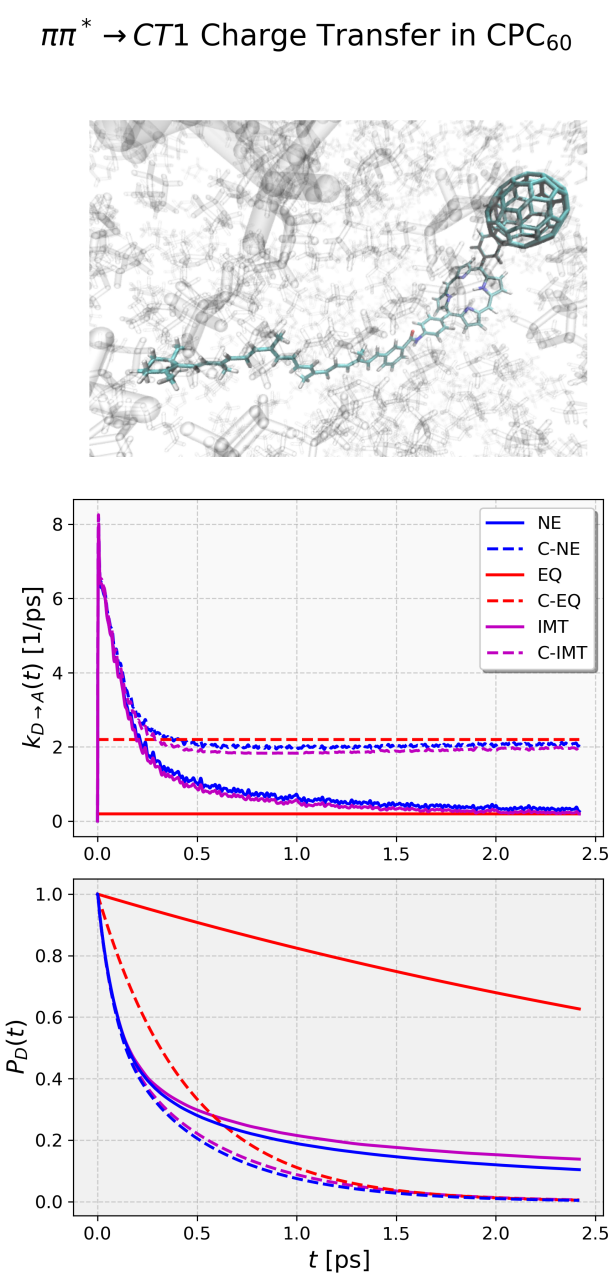


Figure 2.1: Top panel: A schematic view of CPC_{60}/THF. Middle panel: The NE-FGR rate coefficient, $k_{D\rightarrow A}(t)$, for the $\pi\pi^* \rightarrow$CT1 transition when CPC_{60} is in its bent conformation. Bottom panel: The population of the $\pi\pi^*$ donor state as a function of time, $P_D(t)$, simulated based on the p-tcl-OD-QME, Eq. 2.8. Shown are results based NE-FGR (NE), E-FGR (EQ) and the IMT approximation for NE-FGR (IMT). C indicates "in-cavity", while lack of C indicates "cavity-free". E.g., NE and C-NE corresponds to cavity-free and cavity-modified NE-FGR, respectively.

in Ref. 140, we will focus here on the effect of the cavity on the nonequilibrium portion of the dynamics.

The cavity-free NE-FGR rate of the $\pi\pi^* \rightarrow$ CT1 transition in CPC_{60}/THF is seen to be much faster than the rate predicted by E-FGR. This behavior has been reported previously, and traced back to the large deviation between the nuclear configurations in the ground state and the $\pi\pi^*$ state, and the fact that the ground state nuclear configurations are in closer proximity to the crossing region between the $\pi\pi^*$ and CT1 PESs, which leads to the observed enhancement in the CT rate.[94] However, placing the CPC_{60}/THF system in a resonant cavity makes the difference between NE-FGR and E-FGR rates smaller. This can be traced back to the fact that the cavity-modified enhancement of the NE-FGR rates involves $k^m_{\pi\pi^*\rightarrow CT1}(t, \pm\omega_p)$, that corresponds to shifting the $\pi\pi^*$ PES by $\pm\hbar\omega_p$, which in turn moves the crossing point between the $\pi\pi^*$ and CT1 PESs relative to the ground state nuclear configurations. As a result, the ground state equilibrium nuclear configurations end up being further away from the crossing point between the dressed $\pi\pi^*$ and CT1 PESs, thereby decreasing the nonequilibrium effects, as measured by the difference between E-FGR and NE-FGR rates.

The IMT approximation is observed to accurately reproduce the NE-FGR CT dynamics. Thus, the high temperature and short time limits it is based on appear to be justified for this prototypical photo-induced CT reaction at room temperature.

2.5 Cavity-modified rates for the Garg-Onuchic-Ambegaokar (GOA) model of an electron transfer reaction in the condensed phase

In this section, we apply the theoretical framework developed in Sec. 2.3 to the GOA model for CT in the condensed phase.[142] To this end, we compare and contrast the CT dynamics inside and outside of the cavity based on the p-tcl-OD-QME, Eq. 2.8. We do so in the case of a nonequilibrium initial state at different temperatures and frictions (see below).

The cavity-free Hamiltonian for the GOA model is given by:

$$\begin{aligned} \hat{H}^m &= \Gamma\hat{\sigma}_x + \frac{\hbar\omega_{DA}}{2}\hat{\sigma}_z + \frac{\hat{P}_y^2}{2} + \frac{1}{2}\Omega^2(\hat{y} + y_0\sigma_z)^2 \\ &\quad + \sum_{\alpha=1}^{N-1}\left[\frac{\hat{p}_\alpha^2}{2} + \frac{1}{2}\omega_\alpha^2\left(\hat{x}_\alpha + \frac{c_\alpha\hat{y}}{\omega_\alpha^2}\right)^2\right] \end{aligned} \tag{2.36}$$

Here, $\hat{\sigma}_x = |D\rangle\langle A| + |A\rangle\langle D|$ and $\hat{\sigma}_z = |D\rangle\langle D| - |A\rangle\langle A|$, where $|D\rangle$ and $|A\rangle$ are the donor and acceptor electronic states; $V^n_{DA} = \Gamma$ is the electronic coupling coefficient (constant within the

Condon approximation); $-\hbar\omega_{DA}$ is the donor-to-acceptor CT reaction energy; $\hat{y}$, $\hat{P}_y$, and Ω are the mass-weighted primary mode coordinate, momentum, and frequency, respectively; $\{\hat{x}_j, \hat{p}_j, \omega_j | j = 1, ..., N-1\}$ are the mass-weighted coordinates, momenta and frequencies, respectively, of the secondary bath modes; $\{c_j | j = 1, ..., N-1\}$ are the coupling coefficients between the secondary modes and the primary mode; $2y_0$ is the shift in equilibrium geometry between the donor and acceptor states along the primary mode, such that the reorganization energy is given by $E_r = 2\Omega^2 y_0^2$. Finally, the bath of secondary modes is described by an Ohmic spectral density with exponential cutoff:

$$J(\omega) = \frac{\pi}{2} \sum_{j=1}^{N-1} \frac{c_j^2}{\omega_j} \delta(\omega - \omega_j) = \tilde{\eta} \omega e^{-\omega/\omega_c} \quad . \tag{2.37}$$

Here, $\tilde{\eta}$ is the friction coefficient, which determines the coupling strength between the primary and secondary modes, and ω_c is the cutoff frequency. The form of the Hamiltonian in Eq. 2.36 requires representing the continuous spectral density in Eq. 2.37 in terms of a set of discrete secondary bath modes. To this end, we followed the procedure outlined in Refs. 147, 130, with the number of secondary modes set to $N_s = N - 1 = 1000$.

The parameters for the GOA model under consideration in this section were adopted from Refs. 130, 148. However, it should be noted that the Hamiltonian in Refs. 130, 148 is not given in terms of mass-weighted coordinates. It therefore needed to be put in terms of mass-weighted coordinates in order to be consistent with Eq. 2.36. More specifically, we set $y_0 = \sqrt{M_s}(R_{A,0} - R_{D,0})/2$ and $\tilde{\eta} = f_i \eta / M_s = f_i \eta_0$ (the reader is referred to Ref. 130 for the definitions of $R_{A,0}$, $R_{D,0}$, M_s and η). Here f_i is a scaling factor, $f_i \in \{0.1, 1.0\}$, used to adjust the friction (the model in Ref. 130 corresponds to $f_i = 1.0$).

The nonequilibrium initial state of the nuclear DOF (see Eq. 2.5) is obtained by assuming that the equilibrium geometry of the ground state is shifted by s along the primary mode coordinate relative to the equilibrium geometry of the D state, such that

$$\hat{\rho}_n(0) = \frac{e^{-\beta \hat{H}_G^n}}{\mathrm{Tr}_n \left[e^{-\beta \hat{H}_G^n} \right]} \quad . \tag{2.38}$$

where

$$\begin{aligned} \hat{H}_G^n &= E_G + \frac{\hat{P}_y^2}{2} + \frac{1}{2}\Omega^2 (\hat{y} + y_0 + s)^2 \\ &\quad + \sum_{\alpha=1}^{N-1} \left[\frac{\hat{p}_\alpha^2}{2} + \frac{1}{2}\omega_\alpha^2 \left(\hat{x}_\alpha + \frac{c_\alpha \hat{y}}{\omega_\alpha^2} \right)^2 \right] \quad . \end{aligned} \tag{2.39}$$

Here, $E_G < 0$ is the energy of the ground state at its equilibrium geometry relative to the acceptor energy in its equilibrium geometry.

The fact that the primary and secondary modes are bilineraly coupled implies that the nuclear coordinates can be cast in terms of the corresponding normal modes instead of in terms of the primary mode and secondary modes. [102, 149, 54] Doing so allows for casting the GOA Hamiltonian in the following alternative and yet completely equivalent form:

$$\hat{H}^m = \hat{H}^n_D \left|D\right\rangle\!\left\langle D\right| + \hat{H}^n_A \left|A\right\rangle\!\left\langle A\right| + \Gamma[\left|D\right\rangle\!\left\langle A\right| + \left|A\right\rangle\!\left\langle D\right|] \quad . \tag{2.40}$$

where,

$$\begin{aligned} \hat{H}^n_D &= \hbar\omega_{DA} + \sum_{j=1}^{N}\left[\frac{1}{2}\tilde{P}_j^2 + \frac{1}{2}\tilde{\omega}_j^2\tilde{R}_j^2\right], \\ \hat{H}^n_A &= \sum_{j=1}^{N}\left[\frac{1}{2}\tilde{P}_j^2 + \frac{1}{2}\tilde{\omega}_j^2(\tilde{R}_j - \tilde{R}_j^{eq})^2\right] \end{aligned} \tag{2.41}$$

Here, $\{\tilde{R}_j, \tilde{P}_j, \tilde{\omega}_j | j = 1, ..., N\}$ are the normal mode coordinates, momenta, and frequencies, and $\{\tilde{R}_j^{eq} | n = 1, ..., N\}$ are the donor-to-acceptor shifts in the equilibrium geometry along the normal mode coordinates. The cavity-free nuclear Hamiltonian for the ground electronic state can also be cast in terms of the normal modes coordinates and momenta:

$$\hat{H}^n_G = E_G + \sum_k \left[\frac{1}{2}\tilde{P}_k^2 + \frac{1}{2}\tilde{\omega}_j^2(\tilde{R}_j + \tilde{s}_j)^2\right] \tag{2.42}$$

where $\{\tilde{s}_j | n = 1, ..., N\}$ are the donor-to-ground shifts in the equilibrium geometry along the normal mode coordinates. The closed form expressions for the NE-FGR correlation functions, IMT average energy gaps, and IMT variances derived for CPC_{60} can be used for the GOA model by replacing $\{\omega_j,\ S_j,\ R_j^{eq}\}$ with $\{\tilde{\omega}_j,\ \tilde{s}_j,\ \tilde{R}_j^{eq}\}$ (see Eqs. 2.31-2.35).

The results reported below were obtained for the parameters in Table 2.1, which correspond to model II in Ref 130. We choose a value of $\hbar\omega_{DA} = 800$ meV, which was used to generate Figure 5 of Ref 130. Those model parameters correspond to a typical electron transfer reaction, where the system is in the inverted region with a relatively small donor-to-acceptor activation energy along the primary bath coordinate (see Fig. 2.2). We consider the CT dynamics inside and outside the cavity for an initial nonequilibrium state that corresponds to $s = 2\,y_0$ (see Fig. 2.2). The dependence of the cavity-free and cavity-modified CT dynamics on $\tilde{\eta}$ and T ($T = \{100\,\mathrm{K},\ 300\,\mathrm{K}\}$ and $\tilde{\eta} = \{0.1\,\eta_0,\ 1.0\,\eta_0\}$) is shown in Fig 2.3.

Inspection of Fig. 2.3 reveals that for the GOA model parameters under consideration, the NE-FGR-based overall CT rate is slower than the E-FGR-based CT rate, both inside

$\hbar g_p$	5.0 meV
$\hbar\omega_p$	200.0 meV
Γ	5.0 meV
$\hbar\Omega$	9.5 meV
$\hbar\omega_{DA}$	200.0 meV
y_0	312.0 meV$^{1/2}$
T	100.0, 300.0 K
s/y_0	2.0
$\tilde{\eta}$	97.3, 9.73 ps^{-1}
ω_c	9.5 meV
ω_{max}/ω_c	3.0
N_s	1000

Table 2.1: The GOA model parameters used in this work.

and outside the cavity. This trend is opposite to that observed for the triad model, where the NE-FGR-based CT rate was faster than the E-FGR-based CT rate (see Fig. 2.1). The trend reversal can be traced back to the fact that for the GOA model parameters under consideration, the nonequilibrium initial state is relatively far from the crossing point between the donor and acceptor PESs, while the equilibrium state on the donor PES is in the close vicinity of the crossing point. Given that proximity to the crossing point corresponds to faster CT rates, the E-FGR-based rate would be expected to be faster than the NE-FGR-based rate. Note that the NE-FGR rate oscillates. Those oscillations reflect the nonequilibrium dynamics of the wave packet on the donor PES. More specifically, the rate is enhanced when the wavepacket passes in the close vicinity of the crossing point and diminishes when it moves further away from it. In contrast, the equilibrium state stays close to the crossing point at all times, which leads to faster overall rates.

As expected, placing the system in the cavity is seen to increase both E-FGR and NE-FGR rates. Placing the system in the cavity is also seen to increase the difference between the NE-FGR-based CT rate and the E-FGR-based CT rate. This suggests that coupling to the cavity effectively pushes the nonequilibrium initial state even further away from the crossing point compared to the equilibrium state. This is because the cavity-modified enhancement of the NE-FGR rates involves $k^m_{j\to k}(t, \pm\omega_p)$, which corresponds to shifting the donor PES by $\pm\hbar\omega_p$. The crossing point between the dressed donor and acceptor PESs would shift accordingly. For the model parameters under consideration, this translates into the initial nonequilibrium state being further away from the crossing point than the initial equilibrium state, thereby leading to further suppression of the NE-FGR rate relative to the cavity-free case.

Decreasing friction has the expected effect of enhancing the oscillatory behavior of the NE-FGR rate and lengthening the time it takes for it to settle into its E-FGR plateau value. This is due to lower coupling strength of the primary mode coordinate to the bath secondary modes, slowing energy dissipation into these modes. As expected, the effect of friction is insensitive to the presence of the cavity.

Decreasing the temperature from 300 K to 100 K is seen to produce a somewhat larger cavity enhancement. More specifically, while the cavity-modified E-FGR rate is about twice as large as the cavity-free E-FGR rate at 300 K, it is three times as large at 100 K. This can be traced back to the fact that the equilibrium thermal distribution is broader at 300 K compared to that at 100 K. When one places the system in the cavity, the dressed donor PES is shifted down by $-\hbar\omega_p$, thereby enhancing its barrierless character. The fact that the distribution is narrower at 100 K means that the resulting enhancement of the CT rate is more pronounced since it is more "focused" around the crossing point. Otherwise, the rates are seen to be relatively insensitive to the temperature, which is consistent with the fact that the CT reaction is essentially barrierless in this case.

Finally, IMT is seen to reproduce the NE-FGR rates remarkably well. Given that the model parameters are representative of typical CT reactions, this suggests that IMT can provide accurate estimates in cases where there is no computationally feasible path for calculating the fully quantum-mechanical NE-FGR rates.

2.6 Summary and concluding remarks

FGR-based rate theories have proven to be extremely useful for modeling the dynamics of a wide range of chemical processes. In this chapter, we introduced a general-purpose framework for estimating cavity-modified NE-FGR rates of the transition rate between a photoexcited bright donor electronic state and a dark acceptor electronic state, when the nuclear degrees of freedom start out in a nonequilibrium initial state. Importantly, the proposed framework requires the same inputs needed for estimating the corresponding cavity-free NE-FGR rates. Using this framework therefore makes it possible to bypass the need for an explicit simulation of the molecular system inside the cavity.

The proposed framework is based on the fact that the photonic DOF can be added to the Hamiltonian as nuclear-like DOF, as well as on assuming that the photonic and nuclear DOF are coupled to the electronic DOF, but not to each other. Taking advantage of the resulting separability of the nuclear/photonic terms in the Hamiltonian into purely nuclear and purely photonic terms then makes it possible to calculate cavity-modified NE-FGR rates from cavity-free inputs.

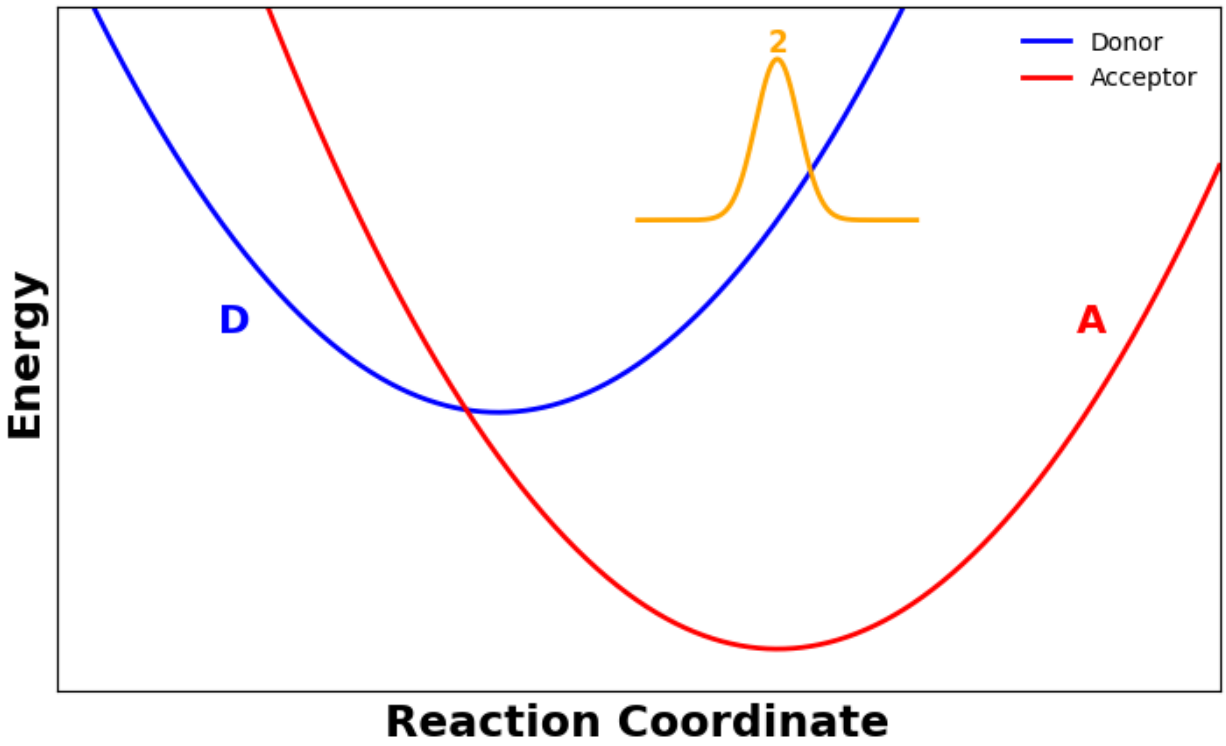


Figure 2.2: A schematic view of the GOA model under consideration and the nonequilibrium initial state. The donor (blue) and acceptor (red) PESs are plotted along the GOA model's primary mode coordinate. The number 2 corresponds to the shift, $s/y_0 = 2.0$, of the ground state equilibrium geometry elative to the donor's equilibrium geometry (orange, see Eq. 2.39).

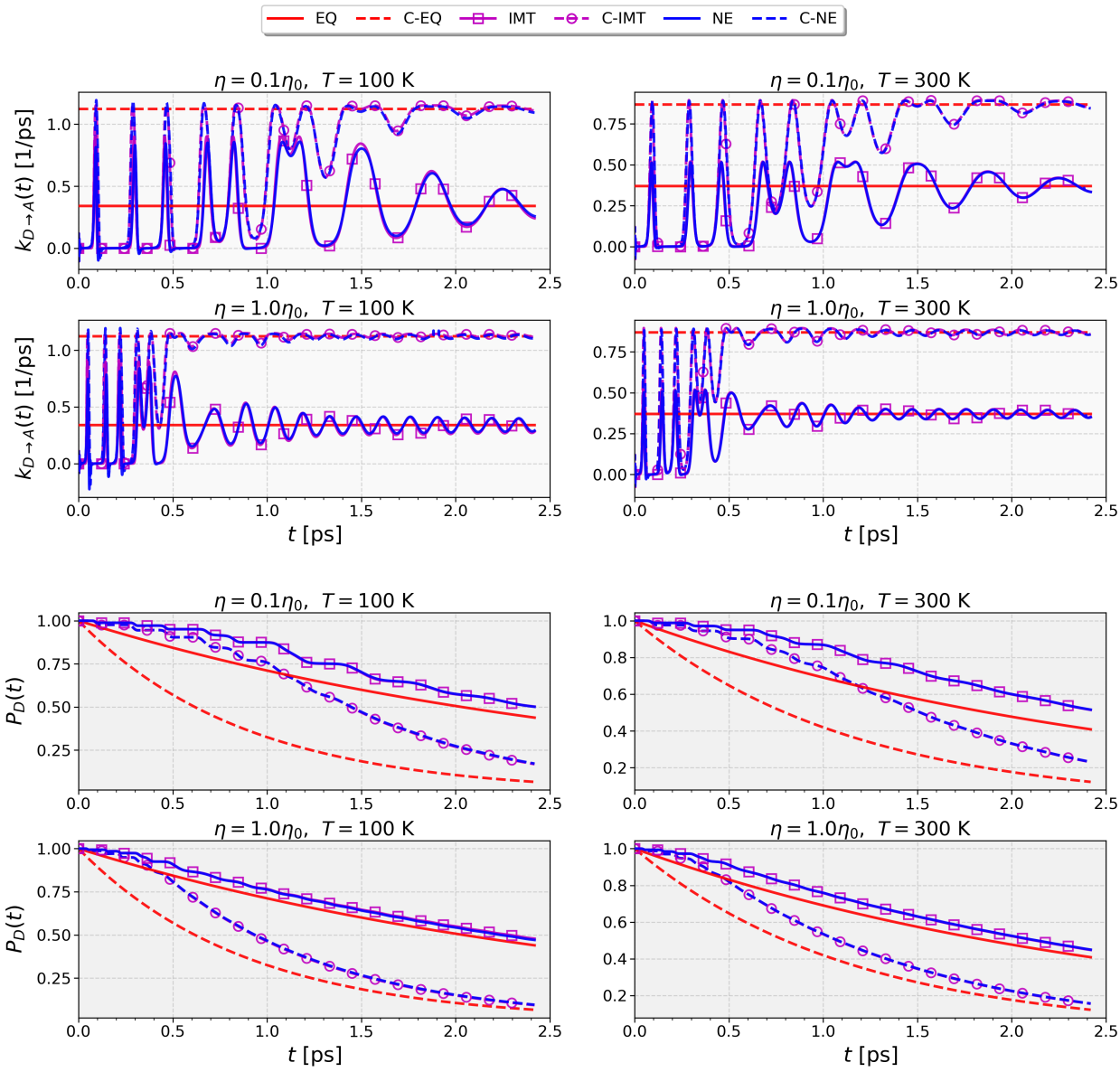


Figure 2.3: Comparison of donor-to-acceptor transition rates, $k_{D\to A}(t)$, (top panels) and donor population, $P_D(t)$, (bottom panels) as a function of time, at different temperatures and frictions, for the GOA model. Shown are results based NE-FGR (NE), E-FGR (EQ) and the IMT approximation for NE-FGR (IMT). C indicates "in-cavity", while lack of C indicates "cavity-free". For example, NE and C-NE corresponds to cavity-free and cavity-modified NE-FGR, respectively.

Unlike other cavity-enabled effects, relatively weak coupling between molecular and cavity DOF can give rise to significant cavity-induced effects on the NE-FGR rates. This is because NE-FGR is already based on treating the coupling between electronic states as a small perturbation (within the framework of second-order perturbation theory). More specifically, coupling between the electronic DOF and cavity modes modifies the coupling between electronic states when the molecular system is placed inside a cavity. Thus, treating this additional electronic coupling as a small perturbation can still give rise to significant modifications of the corresponding NE-FGR rates.

We also introduced a generalization of IMT for cavity-modified photoinduced CT reactions. IMT corresponds to the shot-time and high-temperature limit of the LSC approximation of NE-FGR with the additional assumption that the fluctuations of the donor-acceptor energy gap satisfy Gaussian statistics. Given the wide range of applicability of those assumptions, cavity-modified IMT opens the door to applications to realistic models.

In addition to significantly modifying the rates, coupling to the cavity was also observed to be capable of affecting the nonequilibrium effects by shifting the dressed donor PES by $\pm\hbar\omega_p$, which in turn modifies the nonequilibrium nature of the initial state.

While being rather general, the proposed framework is still based on a number of assumptions, including restricting ourselves to two electronic states, assuming that the molecular system is coupled to a single cavity mode and has no permanent dipole moment and not accounting to the effect of the cavity of the lifetime of the donor state. Work on extending the framework beyond those restrictive assumptions, while still maintaining its ability to produce cavity-modified rates from cavity-free inputs, is currently underway and will be reported in forthcoming publications.

CHAPTER 3

Solution of Nonautonomous Linear Ordinary Differential Equations on a Quantum Device

3.1 Statement of Collaboration

This work was conducted while Pouya Khazaei was advised by Professor Eitan Geva. The central idea, theoretical framework, and overall direction of the project were conceived and developed by Pouya Khazaei.

Regular meetings were held with Professor Geva during the course of the work, during which progress and results were discussed. Professor Geva provided general feedback on the research. He will review and provide editorial feedback on the manuscript prior to submission.

All theoretical development, analytical derivations, numerical implementation, data generation, analysis, and preparation of the manuscript were carried out by Pouya Khazaei. This chapter is based on work currently in preparation with the following authors and working title:

Khazaei, P.; Geva, E. Solution of Nonautonomous Linear Ordinary Differential Equations on a Quantum Device.

3.2 Introduction

Real, nonautonomous linear ordinary differential equations (ODEs) form a broad and fundamental class of evolution equations in physics, chemistry, and applied mathematics. Any complex-valued linear ODE can be decomposed into coupled equations for its real and imaginary parts, yielding an equivalent real-valued linear system. Many partial differential equations likewise reduce to systems of linear nonautonomous ODEs upon spatial discretization. For example, the Fokker–Planck equation governing classical open-system dynamics becomes a linear ODE system after discretization and is explicitly nonautonomous when the potential

energy surface is time dependent. In this real representation, the dynamics are nonunitary whenever the generator of time evolution is not skew-symmetric.

Current noisy intermediate-scale quantum (NISQ) devices natively implement only unitary transformations. Consequently, nonunitary time evolution must be embedded into a larger Hilbert space in which the overall evolution is unitary—a procedure known as dilation. In such approaches, the nonunitary operator is realized as a subblock of a higher-dimensional unitary matrix and recovered through measurement and post-selection [43]. The Sz.-Nagy construction [42] provides one general dilation strategy, though at the cost of increased Hilbert-space dimension and circuit depth, and has been explored in chemically motivated simulations [45, 44]. More recently, singular value decomposition (SVD)-based dilation schemes [50, 49] factorize the propagator into orthogonal matrices and a diagonal matrix of singular values, often reducing circuit depth and improving suitability for NISQ implementations.

In existing SVD-based approaches, however, the nonunitary propagator is first computed classically and subsequently decomposed at each time step via a numerical SVD before being implemented on quantum hardware. For an N-dimensional system, this procedure requires classical propagation of an $N \times N$ matrix and repeated $\mathcal{O}(N^3)$ SVD computations, effectively treating each time slice independently and discarding the smooth geometric structure of the underlying matrix flow. As a result, the quantum device applies a sequence of precomputed operators, while the dominant computational cost remains classical.

Here we extend the SVD-based framework beyond the application of a precomputed nonunitary propagator. Rather than repeatedly computing and dilating the full propagator at each time step, we derive coupled equations of motion for the SVD factors of the time-dependent propagator and evolve these factors directly. The orthogonal components evolve under skew-symmetric generators and therefore remain on the orthogonal group manifold, enabling hardware-native implementation through unitary quantum gates. The remaining diagonal component admits a unitary embedding as well. In this formulation, the smooth evolution of the singular vectors is preserved, repeated numerical SVDs are eliminated, and classical propagation of the full nonunitary operator is avoided. Instead, the nonunitary dynamics are recast as structured unitary flows supplemented by a single scalar ODE for the largest singular value.

An important instance of real nonautonomous linear ODEs arises in quantum master equations (QMEs), which describe the reduced dynamics of open quantum systems [18]. QMEs have been used to model processes ranging from adiabatic proton-transfer reactions [52, 150, 15] to nonadiabatic energy-transfer dynamics [151, 152]. As a demonstration, we apply the algorithm to a non-Markovian time-convolutionless QME describing photoinduced

charge transfer in the carotenoid–porphyrin–C_{60} (CPC_{60}) molecular triad dissolved in liquid tetrahydrofuran (THF) [141, 95, 104]. While chemically motivated, the proposed framework applies generally to arbitrary real nonautonomous linear ODEs and provides a route toward quantum simulation of open-system dynamics beyond precomputed dilation strategies.

This chapter is organized as follows. In Sec. II we develop the theoretical framework, deriving the equations of motion for the SVD factors and describing their implementation on a quantum device. In Sec. III we apply the method to the population-only time-convolutionless off-diagonal quantum master equation for photoinduced charge transfer in the CPC_{60} molecular triad dissolved in THF and assess performance under realistic noise models. Section IV summarizes the results and discusses implications and future directions.

3.3 Theory

3.3.1 Linear Nonautonomous Ordinary Differential Equations

A linear ordinary differential equation (ODE) is said to be nonautonomous when its coefficient matrix depends explicitly on time. In the real-valued case, the equation takes the form

$$\dot{v}(t) = A(t)\, v(t), \tag{3.1}$$

where $v(t) \in \mathbb{R}^N$ describes the state of the system at time t, and $A(t) \in \mathbb{R}^{N\times N}$ is a time-dependent coefficient matrix. If A is time-independent, the equation is said to be autonomous.

Many evolution equations of interest in physics and chemistry can be written in this form. For example, a vectorized time-convolutionless quantum master equation (tcl-QME) reduces to Eq. (3.1). In contrast, commonly used Markovian quantum master equations such as the Redfield or Lindblad equations typically involve time-independent generators and therefore correspond to autonomous linear ODEs. The algorithm developed here applies generally to nonautonomous linear ODEs and is not restricted to quantum dynamical problems.

Let $\Phi(t)$ denote the propagator, also known as the principal fundamental matrix solution of Eq. (3.1). It satisfies

$$\dot{\Phi}(t) = A(t)\, \Phi(t), \qquad \Phi(0) = I, \tag{3.2}$$

where I is the identity matrix. The solution of the original system can then be expressed as

$$v(t) = \Phi(t)\, v(0). \tag{3.3}$$

In general, when $A(t)$ is not skew-symmetric (or skew-Hermitian in the complex case), the propagator $\Phi(t)$ is nonunitary and therefore cannot be directly implemented on quantum hardware.

3.3.2 Quantum Algorithm for the System Dynamics

Because the propagator $\Phi(t)$ is generally nonunitary, its direct implementation on a quantum device requires a dilation procedure. The method employed here is based on the singular-value decomposition (SVD) of the propagator. We reiterate the procedure detailed in Ref. 49.

We begin with the SVD of $\Phi(t)$:

$$\Phi(t) = U(t)\, \Sigma(t)\, V^{\dagger}(t), \tag{3.4}$$

where $U(t)$ and $V(t)$ are unitary matrices that can be implemented directly using quantum gates. The matrix

$$\Sigma(t) = \mathrm{diag}\Big(\sigma_1(t), \ldots, \sigma_N(t)\Big) \tag{3.5}$$

contains non-negative real singular values $\sigma_j(t)$ and is therefore nonunitary in general.

We order the singular values by magnitude:

$$\sigma_1(t) \geq \sigma_2(t) \geq \cdots \geq \sigma_N(t), \tag{3.6}$$

and rescale them relative to the largest singular value:

$$\tilde{\sigma}_j(t) = \frac{\sigma_j(t)}{\sigma_1(t)}, \qquad 0 \leq \tilde{\sigma}_j(t) \leq 1. \tag{3.7}$$

The diagonal matrix $\Sigma(t)$ can then be written as

$$\Sigma(t) = \frac{\sigma_1(t)}{2} \left(\Sigma^{+}(t) + \Sigma^{-}(t)\right), \tag{3.8}$$

where the diagonal elements of the unitary matrices $\Sigma^{\pm}(t)$ are defined by

$$\Big(\Sigma^{\pm}(t)\Big)_{jj} = \tilde{\sigma}_j(t) \pm i\sqrt{1 - \tilde{\sigma}_j^2(t)}. \tag{3.9}$$

Since each $\tilde{\sigma}_j(t) \in [0,1]$, the quantities $\tilde{\sigma}_j(t) \pm i\sqrt{1-\tilde{\sigma}_j^2(t)}$ lie on the unit circle, ensuring that $\Sigma^{\pm}(t)$ are unitary.

We define a block-diagonal unitary acting on the joint system–ancilla Hilbert space:

$$U_\Sigma(t) = \Sigma^+(t) \oplus \Sigma^-(t). \tag{3.10}$$

To implement the evolution, the system state must first be encoded into a normalized quantum state. Thus, we require

$$\|v(0)\| = 1, \tag{3.11}$$

so that $|v(0)\rangle$ is a valid quantum state. If $v(0)$ is not normalized, it must be rescaled prior to state preparation.

The full time evolution governed by Eq. (3.1) is implemented by introducing a single ancilla qubit and applying the circuit shown in Fig. 3.1. The Hadamard gates prepare and recombine the ancilla superposition required to interfere the two dilation branches.

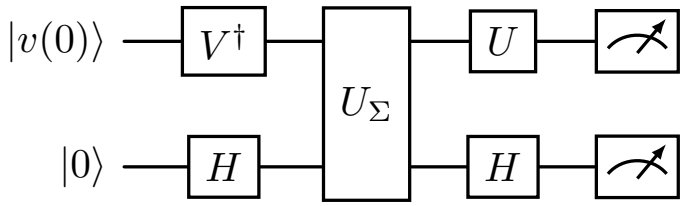


Figure 3.1: Quantum circuit implementing the SVD-based dilation using $V^\dagger$, U_Σ, and U on the system register and Hadamard gates on the ancilla.

Acting on the initial joint state $|v(0)\rangle \otimes |0\rangle$, the circuit produces

$$\frac{1}{2}\begin{pmatrix} U(t)\left(\Sigma^+(t) + \Sigma^-(t)\right) V^\dagger(t)\,|v(0)\rangle \\ U(t)\left(\Sigma^+(t) - \Sigma^-(t)\right) V^\dagger(t)\,|v(0)\rangle \end{pmatrix}. \tag{3.12}$$

Post-selecting the ancilla outcome $|0\rangle$ yields

$$\frac{\Phi(t)\,|v(0)\rangle}{\sigma_1(t)}, \tag{3.13}$$

while the $|1\rangle$ branch is discarded.

3.3.3 Summary of the EOM for SVD of $\Phi(t)$

Although the propagator $\Phi(t)$ is nonunitary and therefore cannot be directly integrated on a quantum device, we can instead derive equations of motion (EOM) for the orthogonal factors obtained from its SVD. Differentiating Eq. (3.4) with respect to time yields coupled EOM for the factors $\{U(t), V(t), \Sigma(t)\}$. These differential equations for the SVD of $\Phi(t)$ were derived in Ref. 153 and are given by

$$\dot{U}(t) = U(t)\, Z(t), \tag{3.14}$$

$$\dot{V}(t) = V(t)\, W(t), \tag{3.15}$$

$$\dot{\sigma}_i(t) = G_{ii}(t)\, \sigma_i(t), \tag{3.16}$$

where

$$G(t) = U^T(t)\, A(t)\, U(t), \tag{3.17}$$

and the matrix elements of $Z(t)$ and $W(t)$ are

$$Z_{jk}(t) = \frac{\sigma_k^2(t)\, G_{jk}(t) + \sigma_j^2(t)\, G_{kj}(t)}{\sigma_k^2(t) - \sigma_j^2(t)}, \tag{3.18}$$

$$W_{jk}(t) = \frac{\sigma_k(t)\sigma_j(t)\, (G_{kj}(t) + G_{jk}(t))}{\sigma_k^2(t) - \sigma_j^2(t)}. \tag{3.19}$$

These EOM have been studied extensively in dynamical systems theory, including applications to the computation of Lyapunov exponents and exponential dichotomy spectra [154, 155, 156, 157]. We use them here to develop a quantum algorithm for the evolution of real nonautonomous linear ODEs.

Importantly, the evolution equations (3.14) and (3.15) preserve orthogonality. The generators $Z(t)$ and $W(t)$ are real skew-symmetric matrices, i.e.,

$$Z^T(t) = -Z(t), \qquad W^T(t) = -W(t), \tag{3.20}$$

which guarantees that

$$U^T(t)U(t) = I, \qquad V^T(t)V(t) = I \tag{3.21}$$

for all time. Thus, $U(t)$ and $V(t)$ remain orthogonal matrices throughout the evolution.

Because skew-symmetric generators produce orthogonal time evolution, Eqs. (3.14) and

(3.15) can be integrated directly on a quantum device using Lie-group integrators, such as Magnus-expansion-based methods (see Sec. 3.3.6), which generate orthogonal transformations by construction.

In contrast, $\Sigma(t)$ is not orthogonal, and its generator does not produce orthogonal evolution. Rather than evolving $\Sigma(t)$ directly, we instead evolve the orthogonal matrices $\{\Sigma^+(t), \Sigma^-(t)\}$ introduced in the previous subsection. Because $\Sigma^\pm(t)$ are orthogonal by construction, their dynamics can be implemented on a quantum device. To accomplish this, we now derive the corresponding equations of motion for $\Sigma^\pm(t)$.

3.3.4 EOM for $\Sigma^\pm$

An equation of motion for the orthogonal factors $\Sigma^\pm(t)$ can be obtained by differentiating their diagonal elements defined in Eq. (3.9). For clarity, we restate the definition:

$$\sigma^\pm_{jj}(t) = \tilde{\sigma}_j(t) \pm i\sqrt{1-\tilde{\sigma}_j^2(t)}. \tag{3.22}$$

Taking the time derivative gives

$$\dot{\sigma}^\pm_j(t) = \left(1 \mp \frac{i\,\tilde{\sigma}_j(t)}{\sqrt{1-\tilde{\sigma}_j^2(t)}}\right)\dot{\tilde{\sigma}}_j(t). \tag{3.23}$$

Recall that

$$\tilde{\sigma}_j(t) = \frac{\sigma_j(t)}{\sigma_1(t)}. \tag{3.24}$$

Differentiating this expression yields

$$\dot{\tilde{\sigma}}_j(t) = \frac{\dot{\sigma}_j(t)}{\sigma_1(t)} - \frac{\dot{\sigma}_1(t)\,\sigma_j(t)}{\sigma_1^2(t)}. \tag{3.25}$$

Using Eq. (3.16), $\dot{\sigma}_i(t) = G_{ii}(t)\,\sigma_i(t)$, we obtain

$$\dot{\tilde{\sigma}}_j(t) = \Big(G_{jj}(t) - G_{11}(t)\Big)\tilde{\sigma}_j(t). \tag{3.26}$$

Substituting Eq. (3.26) into Eq. (3.23) gives the EOM for the elements of $\Sigma^\pm(t)$:

$$\dot{\sigma}^\pm_j(t) = \Big(G_{jj}(t) - G_{11}(t)\Big)\tilde{\sigma}_j(t)\left(1 \mp \frac{i\,\tilde{\sigma}_j(t)}{\sqrt{1-\tilde{\sigma}_j^2(t)}}\right). \tag{3.27}$$

This equation can be written in Liouville form with a time-dependent generator:

$$\dot{\Sigma}^{\pm}(t) = -\,i\,L^{\pm}(t)\,\Sigma^{\pm}(t), \tag{3.28}$$

where $L^{\pm}(t)$ is diagonal with elements

$$L^{\pm}_{jj}(t) = \pm\Big(G_{jj}(t) - G_{11}(t)\Big)\frac{\tilde{\sigma}_j(t)}{\sqrt{1-\tilde{\sigma}_j^2(t)}}. \tag{3.29}$$

For $j = 1$, we have $\tilde{\sigma}_1(t) = 1$, which implies $\sigma^{\pm}_{11}(t) = 1$ for all time. Consequently,

$$L^{\pm}_{11}(t) = 0. \tag{3.30}$$

Thus, all factors $U(t), V(t), \Sigma^{\pm}(t)$ evolve under generators that produce orthogonal transformations, enabling the full SVD-based dynamics to be implemented using unitary quantum gates.

3.3.5 Summary: SVD-EOM for Quantum Evolution of Nonautonomous Linear ODEs

We now summarize the set of equations of motion used to evolve the real nonautonomous linear homogeneous ODE $\dot{v}(t) = A(t)v(t)$ on a quantum device. We refer to this system as the SVD-EOM.

The orthogonal factors $\{U(t), V(t), \Sigma^{\pm}(t)\}$ evolve under generators that produce unitary (orthogonal) propagators and can therefore be implemented directly on a quantum device. The associated equations of motion are

$$\dot{U}(t) = U(t)\,Z(t), \tag{3.31}$$

$$\dot{V}(t) = V(t)\,W(t), \tag{3.32}$$

$$\dot{\Sigma}^{\pm}(t) = -\,i\,L^{\pm}(t)\,\Sigma^{\pm}(t), \tag{3.33}$$

where

$$G(t) = U^T(t)\,A(t)\,U(t). \tag{3.34}$$

The matrix elements of the generators are

$$Z_{jk}(t) = \frac{\tilde{\sigma}_k^2(t)\, G_{jk}(t) + \tilde{\sigma}_j^2(t)\, G_{kj}(t)}{\tilde{\sigma}_k^2(t) - \tilde{\sigma}_j^2(t)}, \tag{3.35}$$

$$W_{jk}(t) = \frac{\tilde{\sigma}_k(t)\tilde{\sigma}_j(t)\,(G_{kj}(t) + G_{jk}(t))}{\tilde{\sigma}_k^2(t) - \tilde{\sigma}_j^2(t)}, \tag{3.36}$$

$$L_{jj}^{\pm}(t) = \begin{cases} 0, & j = 1, \\ \pm\dfrac{\tilde{\sigma}_j(t)\Big(G_{jj}(t) - G_{11}(t)\Big)}{\sqrt{1 - \tilde{\sigma}_j^2(t)}}, & j \neq 1. \end{cases} \tag{3.37}$$

In addition to the quantum evolution, a single scalar ODE is propagated classically:

$$\dot{\sigma}_1(t) = G_{11}(t)\, \sigma_1(t). \tag{3.38}$$

Each $N \times N$ matrix is vectorized in Liouville space and encoded as a normalized quantum state. For an orthogonal matrix $U \in \mathbb{R}^{N\times N}$,

$$\langle\langle U \mid U \rangle\rangle = \mathrm{Tr}(U^T U) = N. \tag{3.39}$$

Thus, the normalized encoding is

$$|U\rangle\rangle = \frac{1}{\sqrt{N}}\, \mathrm{vec}(U), \tag{3.40}$$

and similarly for V and $\Sigma^{\pm}$. The original matrix elements are recovered by multiplying the measured amplitudes by $\sqrt{N}$.

3.3.6 Quantum Algorithm for U and V

We focus on the ODE for U, as the treatment for V is completely analogous. The equation of motion

$$\dot{U}(t) = U(t)\, Z(t), \tag{3.41}$$

generates orthogonal evolution since $Z(t)$ is skew-symmetric.

The exact solution can formally be written using the Magnus expansion,

$$U(t) = U(t_0) \exp\Big(\Omega(t)\Big), \tag{3.42}$$

where $\Omega(t)$ consists of nested commutators and time-ordered integrals. In practice, we discretize time and approximate the short-time propagator over $t_i \to t_i + h$ using the Cayley transform [158]:

$$\mathrm{cay}(Z) = \left[I - \tfrac{h}{2}\, Z\Big(t_i + \tfrac{h}{2}\Big)\right]^{-1} \left[I + \tfrac{h}{2}\, Z\Big(t_i + \tfrac{h}{2}\Big)\right]. \tag{3.43}$$

For skew-symmetric Z, the Cayley transform is orthogonal and therefore corresponds to a unitary gate on a quantum device.

Because $Z(t)$ depends on $U(t)$ and $\sigma(t)$, we approximate the midpoint value $Z(t_i + \frac{h}{2})$ using the midpoint extrapolation method (MPEA) of Ref. 159:

$$Z(t_i + \tfrac{h}{2})_{\mathrm{MPEA}} = \tfrac{23}{12}\, Z(t_i) - \tfrac{16}{12}\, Z(t_{i-1}) + \tfrac{5}{12}\, Z(t_{i-2}). \tag{3.44}$$

Vectorizing in Liouville space, the Cayley update $U \mapsto U\ \mathrm{cay}(Z)$ corresponds to

$$U\ \mathrm{cay}(Z)\ \longleftrightarrow\ \Big(\mathrm{cay}(Z)^T \otimes I\Big)\, |U\rangle\rangle. \tag{3.45}$$

As discussed in the previous subsection, $|U\rangle\rangle$ is encoded as a normalized quantum state.

The circuit in Fig. 3.2 implements the single-step Cayley update.

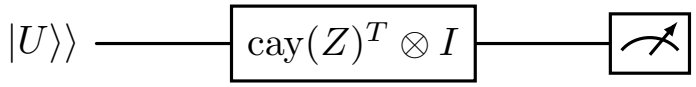


Figure 3.2: Quantum circuit illustrating the application of the single-step Cayley update $\mathrm{cay}(Z)^T \otimes I$ to the vectorized state $|U\rangle\rangle$.

Measurement yields the absolute squares of the matrix elements of $U(t_{i+1})$. Since U is real and orthogonal, relative phases are restricted to $\{\pm 1\}$. Assuming no sign changes over a sufficiently small time step, we reconstruct $U(t_{i+1})$ from the measured magnitudes and the signs from $U(t_i)$, thereby avoiding full quantum state tomography.

Due to device noise, the reconstructed matrix $\tilde{U}(t_{i+1})$ is generally not exactly orthogonal. We project onto the nearest orthogonal matrix via $U^{\mathrm{proj}}(t_{i+1}) = U_u V_u^T$,where U_u and V_u are obtained from the singular value decomposition of $\tilde{U}(t_{i+1})$. Alternative projection schemes, such as polar decomposition or Gram–Schmidt orthogonalization, may also be employed.

3.3.7 Quantum Algorithm for $\Sigma^{\pm}$

The treatment of $\Sigma^{\pm}$ differs from that of $\{U, V\}$ because $\Sigma^{\pm}$ are complex-valued diagonal matrices whose generators are also diagonal. Since $\Sigma^{-} = \Sigma^{+*}$, it suffices to evolve Σ^{+}.

Rather than vectorizing the full $N \times N$ matrix, we exploit its diagonal structure and encode only its diagonal elements:

$$|\Sigma^{+}\rangle = \mathrm{diag}(\Sigma^{+}). \tag{3.46}$$

This reduces the Hilbert-space dimension from N^2 to N.

Because each diagonal element of Σ^{+} has unit magnitude,

$$\langle \Sigma^{+} | \Sigma^{+} \rangle = N, \tag{3.47}$$

so the normalized encoding is obtained by dividing by $\sqrt{N}$.

The vectorized equation of motion is

$$|\dot{\Sigma}^{+}\rangle = -iL^{+}|\Sigma^{+}\rangle, \tag{3.48}$$

where L^{+} is diagonal. Time evolution over a step $t_i \to t_i + h$ is implemented via the Cayley transform,

$$|\Sigma^{+}_{i+1}\rangle = \mathrm{cay}(-iL^{+})|\Sigma^{+}_{i}\rangle. \tag{3.49}$$

Because the generator is diagonal, the Cayley update does not mix computational basis states. The normalized state therefore remains

$$|\Sigma^{+}\rangle = \frac{1}{\sqrt{N}} \sum_{j=1}^{N} e^{i\phi_j} |j\rangle, \tag{3.50}$$

so the evolution affects only the phases $\{\phi_j\}$. Since global phase is irrelevant, we fix $\phi_1 = 0$, so that the first diagonal element equals unity and all other phases are defined relative to this reference component.

The reconstruction problem thus reduces to determining the relative phases $\{\phi_j\}_{j=2}^{N}$. For each $j \geq 2$, we perform an interferometric measurement between the reference component $|1\rangle$ and $|j\rangle$. This is achieved by applying a Hadamard-type rotation in the two-dimensional subspace spanned by $\{|1\rangle, |j\rangle\}$, which mixes the two amplitudes and converts their relative phase into measurable probability differences. To access the remaining phase information, we first apply a phase rotation (e.g., $S^{\dagger}$) to $|j\rangle$ before the Hadamard mixing, which shifts

the relative phase so that a second measurement reveals the complementary information. Repeating this procedure for each j yields all relative phases.

Because the magnitudes of the amplitudes are known a priori and only $N-1$ independent phases must be determined, full quantum state tomography is unnecessary. The reconstruction cost therefore scales linearly with N.

Finally, the diagonal unitary is reconstructed as

$$\Sigma^{+} = \mathrm{diag}\Big(1, e^{i\phi_2}, \ldots, e^{i\phi_N}\Big), \tag{3.51}$$

and $\Sigma^{-} = \Sigma^{+*}$.

3.4 Results & Discussion

3.4.1 Noise Model

To assess performance under realistic hardware imperfections, we simulate noisy execution using Qiskit's `AerSimulator` with a custom `NoiseModel` incorporating depolarizing gate errors, thermal relaxation (T_1/T_2), and readout errors. Calibration data are obtained from the `FakeHanoiV2` backend and summarized in Table 3.1.

Single- and two-qubit gate error rates are extracted from the backend-reported average gate infidelities of the calibrated S_x and C_x gates, respectively. Coherence times T_1 and T_2, as well as gate durations t_1, t_2, and measurement time t_m, are obtained from the backend calibration properties and averaged over all qubits. Readout error probabilities p_{10} and p_{01} are taken from the reported measurement assignment errors and used to construct the confusion matrix.

To probe a range of noise regimes, we introduce a scaling factor $f \in \{10^{-3}, 5\times 10^{-3}, 10^{-2}, 5\times 10^{-2}, 10^{-1}, 5\times 10^{-1}, 1\}$. Gate and readout error probabilities $\{p_1, p_2, p_{10}, p_{01}\}$ are multiplied by f, while coherence times $\{T_1, T_2\}$ are divided by f, thereby scaling decoherence rates proportionally.

Backend-reported gate errors correspond to average infidelities $r_{\mathrm{RB}} = 1 - F_{\mathrm{avg}}$. Because finite gate durations contribute to infidelity through thermal relaxation, we first estimate the relaxation-induced infidelity r_{relax} from the calibrated T_1, T_2 values and gate durations. The residual contribution, $r_{\mathrm{res}} = r_{\mathrm{RB}} - r_{\mathrm{relax}}$, is attributed to a depolarizing channel,[160]

$$\Lambda_p(\rho) = (1-p_n)\rho + p_n\,\frac{\mathbb{I}}{d}, \tag{3.52}$$

where $d = 2^n$ is the Hilbert-space dimension of an n-qubit gate and ρ is a density matrix.

p_1	2.12856e-4
p_2	5.36524e-2
T_1	136546 ns
T_2	138534 ns
t_1	32 ns
t_2	383 ns
t_m	817 ns
p_{10}	8.6e-3
p_{01}	6.6e-2

Table 3.1: Noise parameters extracted from the `FakeHanoiV2` backend. p_1 and p_2 denote single- and two-qubit depolarizing probabilities, T_1 and T_2 are coherence times, t_1, t_2, and t_m are gate and measurement durations, and p_{10}, p_{01} define the readout confusion matrix R.

Substituting this channel into the definition of the average gate fidelity,

$$F_{\text{avg}} = \int d\psi \, \langle\psi|\Lambda_p(|\psi\rangle\langle\psi|)|\psi\rangle, \tag{3.53}$$

yields $F_{\text{avg}} = 1 - \frac{d-1}{d} p_n$, and therefore

$$p_n = \frac{d}{d-1} \, r_{\text{res}}, \tag{3.54}$$

Depolarizing and relaxation errors are applied to the single-qubit gates $\{R_z, S_x, X\}$ and the two-qubit gate C_x using the calibrated gate durations. Readout errors are incorporated through the confusion matrix

$$R = \begin{pmatrix} 1 - p_{10} & p_{10} \\ p_{01} & 1 - p_{01} \end{pmatrix}. \tag{3.55}$$

3.4.2 Results

As a demonstrative example, we adopt the cavity-free charge-transfer model of the CPC_{60} molecular triad dissolved in tetrahydrofuran (THF), introduced in Chapter 2. This model serves as a benchmark system for both the classical and quantum simulations developed in this chapter. The molecular structure of the solvated CPC_{60} triad is shown in Fig. 3.3.

The donor population dynamics are first obtained by direct numerical integration of the p-tcl-OD-QME on a classical computer, which serves as the reference solution. Independently, the same dynamics are generated on a noisy quantum simulator via propagation using the SVD-EOM framework. This enables a controlled comparison between the classi-

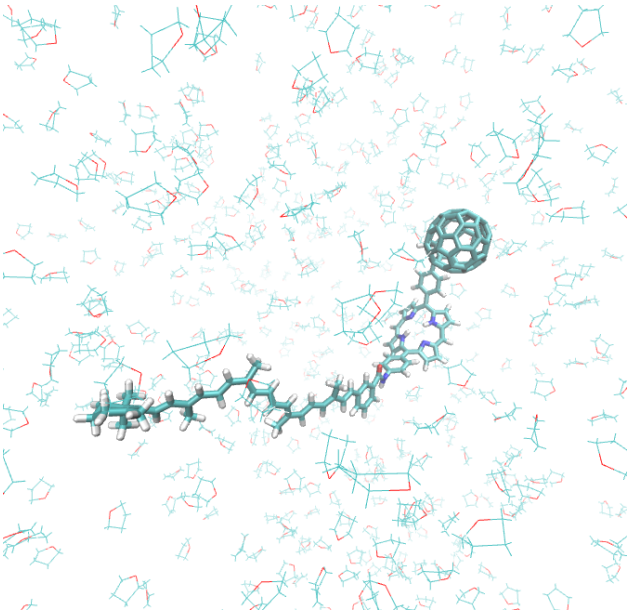


Figure 3.3: Molecular structure of the CPC_{60} triad solvated in tetrahydrofuran (THF).

cal integration of the quantum master equation and its implementation through quantum propagation.

The total simulation time is $t_f = 10^4$ atomic units, discretized using $N_t = 400$ time steps. Each quantum circuit is executed with $N_s = 10^6$ shots. Because the SVD-EOM require nondegenerate singular values (the coefficients $\{z_{jk}, w_{jk}\}$ diverge when singular values coincide), the SVD cannot be initialized at $t = 0$. The rescaled singular values $\tilde{\sigma}_j(t)$ become distinct only after a short transient period. Accordingly, we first integrate the QME for the full propagator $\Phi(t)$ classically from $t = 0$ to $\tilde{t} = 50$ atomic units using $N_{t1} = 50$ time steps. At $t = \tilde{t}$, a numerical SVD of $\Phi(\tilde{t})$ provides the initial values for $U(\tilde{t})$, $V(\tilde{t})$, and $\Sigma^{\pm}(\tilde{t})$. The SVD-EOM are then propagated from $\tilde{t}$ to t_f using N_t time steps and N_s measurement shots per step.

The donor population is reconstructed from the SVD factors as

$$\hat{\rho}(t) = \frac{\sigma_1(t)}{2} U(t)\Big(\Sigma^{+}(t) + \Sigma^{-}(t)\Big)V^{\dagger}(t)\,\hat{\rho}(0). \tag{3.56}$$

Figure 3.4 compares the classical p-tcl-OD-QME solution (propagated using an RK2 integrator) with the noisy quantum simulation of the SVD-EOM for different noise scaling factors f.

We observe that the algorithm remains stable and accurate for moderate noise levels. In particular, for $f \leq 0.1$, the quantum simulation follows the classical reference trajectory to a reasonable extent. These values correspond to optimistic but physically meaningful coher-

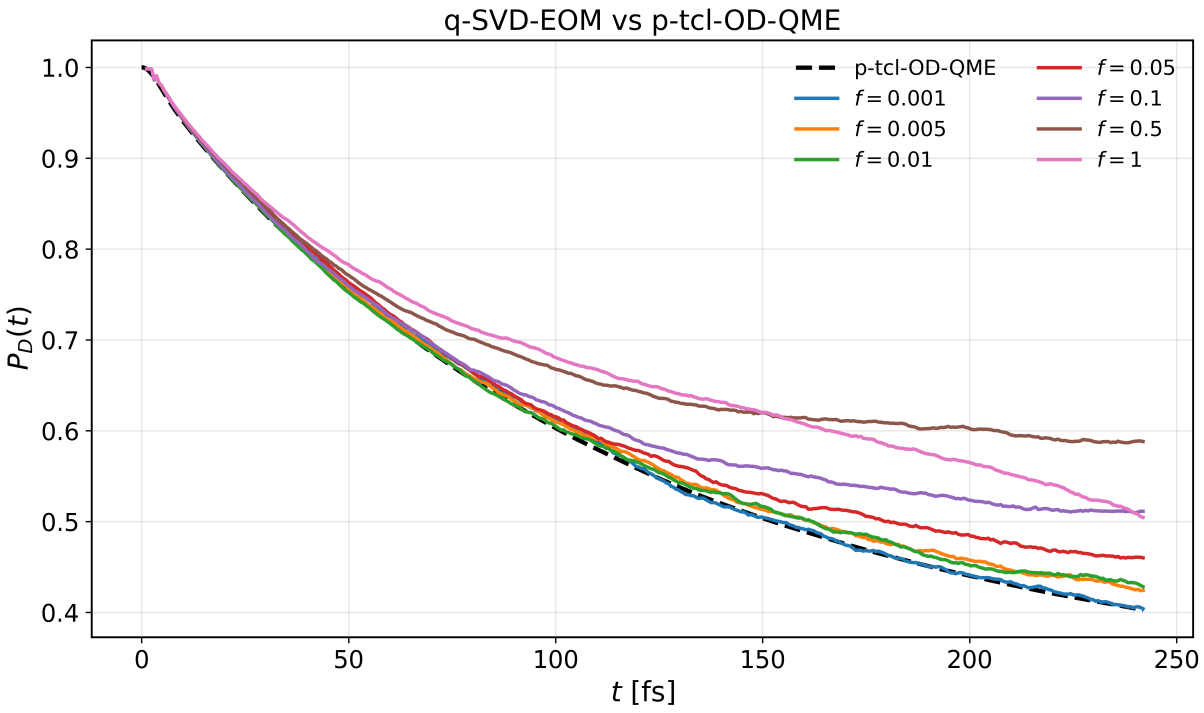


Figure 3.4: Comparison of donor population dynamics obtained from the p-tcl-OD-QME (classical RK2 integration) and the SVD-EOM propagated on a noisy quantum simulator. The noise strength is scaled by $f \in \{10^{-3}, 5 \times 10^{-3}, 10^{-2}, 5 \times 10^{-2}, 10^{-1}, 5 \times 10^{-1}, 1\}$.

ence times and gate fidelities at the present circuit depth. At larger noise levels, deviations accumulate over time, reflecting the sensitivity of Liouville-space propagation to coherent gate errors and decoherence.

The dominant algorithmic cost arises from the Liouville-space updates of U and V. Further improvements could be achieved through error mitigation or error correction techniques, as well as reductions in circuit depth. For example, Walsh–Gray synthesis may reduce the cost of diagonal unitaries, and alternative encodings that propagate columns of U and V individually could lower the effective matrix dimension relative to full vectorization.

We observe that deviations from the classical reference increase with both noise strength and propagation time. At each time step, the quantum device produces a slightly noisy approximation to the intended unitary update. Because this reconstructed operator serves as the initial condition for the subsequent step, errors are carried forward and compound throughout the propagation. As a result, per-step imperfections accumulate over time, leading to increasingly pronounced deviations at longer times. This cumulative error growth reflects the sensitivity of iterative Liouville-space evolution to both coherent gate errors and incoherent decoherence processes.

3.5 Summary and Conclusions

In this chapter, we introduced a quantum algorithm for the integration of real nonautonomous linear ordinary differential equations based on the singular value decomposition (SVD) of the time-dependent propagator. Rather than directly implementing a nonunitary evolution through dilation at each time step, we derived equations of motion for the unitary factors arising from the SVD. Because these factors evolve unitarily, their dynamics can be implemented directly on quantum hardware. The largest singular value is propagated classically, yielding an algorithm that avoids repeated numerical SVDs and eliminates the need to evolve the full nonunitary propagator on a classical device, significantly reducing the classical overhead.

We applied the method to the population-only time-convolutionless off-diagonal quantum master equation (p-tcl-OD-QME) describing photoinduced charge transfer in the CPC_{60} molecular triad dissolved in THF. Comparison with classical integration of the QME demonstrates that, in the absence of noise, the SVD-EOM reproduces the reference dynamics. When realistic noise models are included, we find that the algorithm remains accurate for moderate noise strengths, while deviations grow with increasing noise and propagation time. This behavior arises because per-step errors are carried forward during iterative time evolution, leading to cumulative error growth at longer times.

The dominant computational cost stems from Liouville-space propagation of the unitary factors U and V. Although the present implementation is limited by circuit depth and noise, the results indicate that improvements in gate fidelity, coherence time, and circuit optimization would directly extend the accessible time scales and system sizes. Further efficiency gains may be achieved through improved synthesis of structured unitaries and alternative encodings that reduce effective matrix dimension.

More broadly, the SVD-EOM framework provides a general strategy for simulating nonunitary dynamics on quantum devices by converting the problem into coupled unitary evolutions. Because any complex-valued linear ODE can be recast in real form, the method is applicable beyond quantum master equations and may be extended to other time-dependent linear dynamical systems in physics and chemistry. This work therefore establishes a proof of principle for quantum simulation of open-system dynamics and provides a foundation for future exploration of larger and more complex nonautonomous systems.

CHAPTER 4

A Roadmap for Simulating Chemical Dynamics on a Parametrically Driven Bosonic Quantum Device

4.1 Statement of Collaboration

This work was conducted as a collaboration between members of the Geva, Batista, Santos, and Devoret research groups. The first four authors contributed equally to the published article.

The overall research direction and conceptual framework were developed in collaboration with Professors Eitan Geva and Victor S. Batista.

Pouya Khazaei carried out the primary technical implementation of the project. He implemented the Hamiltonian mapping between the chemical double-well model and the Kerr-cat device Hamiltonian, developed and executed the numerical simulation framework for the open-system dynamics, and resolved technical challenges required to obtain stable and physically meaningful results. Generated the numerical results and prepared the initial versions of Fig. 4.3, Fig. 4.4, and Fig. 4.5. He contributed substantially to drafting and revising the manuscript.

Delmar G. A. Cabral, Brandon C. Allen, and Pablo E. Videla contributed equally to the development of the project, including theoretical analysis, numerical simulations, and manuscript preparation.

Max Schäfer, Rodrigo G. Cortinas, and Alejandro Cros Carrillo de Albornoz provided guidance on the experimental implementation of the Kerr-cat device, including feasibility considerations and realistic parameter regimes accessible on current cQED platforms.

Jorge Chávez-Carlos contributed to theoretical discussions and interpretation of the results.

Professor Lea F. Santos provided senior theoretical guidance and contributed to interpretation of the results.

Professors Eitan Geva and Victor S. Batista provided overall scientific guidance, project supervision, and editorial feedback.

This chapter is based on the following published work:

Cabral, D. G. A.[#]; Khazaei, P.[#]; Allen, B. C.[#]; Videla, P. E.[#]; Schäfer, M.; Cortiñas, R. G.; Carrillo De Albornoz, A. C.; Chávez-Carlos, J.; Santos, L. F.; Geva, E.; Batista, V. S.

[#]These authors contributed equally to this work.

A Roadmap for Simulating Chemical Dynamics on a Parametrically Driven Bosonic Quantum Device. *The Journal of Physical Chemistry Letters* **2024**, 15 (48), 12042–12050. https://doi.org/10.1021/acs.jpclett.4c02864.

4.2 Introduction and Motivation

Computational modeling of reaction dynamics offers insights into the time scales and mechanisms of molecular transformations in chemical reactions, revealing the factors that determine the reaction rates and efficiencies. Most chemical reactions are multi-step processes, with each step described by the reactive flux transferring across a barrier of a double-well potential energy surface along the reaction coordinate. However, simulating these elementary steps can be challenging, especially when barrier recrossing and significant quantum effects are involved, such as tunneling, zero-point energy, and interference. These factors lead to a complex interplay between coherence and dissipative dynamics, which are not accounted for by traditional rate theories, such as transition-state theory. [161, 162, 5, 163, 164, 165]

Recent advances in quantum engineering have generated interest in developing quantum devices to simulate the quantum dynamics of atoms, molecules and condensed phase systems. [38, 37] Such analog quantum simulators can offer significant hardware efficiency advantage over general-purpose quantum computers, especially when the device Hamiltonian can be efficiently mapped onto the molecular system of interest. In this study, we explore the feasibility of using a Superconducting Nonlinear Asymmetric Inductive eLement (SNAIL) transmon [166] to simulate quantum dynamics of elementary chemical reactions. The SNAIL device develops a double-well structure when operated under a continuous drive with frequency close to twice the SNAIL transmon resonance. This system is experimentally realizable in a superconducting quantum circuit and is referred to as Kerr-cat device. [167] Its controllable parameters can be adjusted to model the asymmetric double-well free energy profiles of various molecular systems across a wide range of external conditions, including temperature and coupling strength between the system and the thermal bath of non-reactive degrees of freedom. Here, we explore the capabilities of SNAIL devices by simulating the chemical dynamics of prototypical proton transfer reactions in hydrogen-bonded complexes,

using the SNAIL Hamiltonian parametrized for malonaldehyde dimers and DNA base pairs, as could be experimentally implemented today on currently available platforms. These simulations are currently unattainable with noisy intermediate-scale quantum (NISQ) computers, including state-of-the-art conventional superconducting quantum computers, due to their circuit depth limitations. In contrast, we show that the SNAIL device could accurately capture the dynamics of these chemical reactions, effectively accounting for the delicate interplay between tunneling, zero-point energy, resonance, interference, and dissipative effects.

In transition-state theory (TST),[161, 162, 5] the reaction rate constant is given by the Eyring-Polanyi equation: $k_{TST} = \frac{k_B T}{h} e^{-\Delta G^{\ddagger}/k_B T}$. Here, $\Delta G^{\ddagger}$ is the Gibbs free energy of activation (the barrier height as measured from the minimum of the reactant well to the transition state configuration that corresponds to the barrier top), k_B is the Boltzmann constant, T is the absolute temperature, and h is the Plank constant. The Gibbs free energy of activation can be divided into enthalpy and entropy contributions: $\Delta G^{\ddagger} = \Delta H^{\ddagger} - T\Delta S^{\ddagger}$, where $\Delta H^{\ddagger}$ is the activation enthalpy and $\Delta S^{\ddagger}$ is the activation entropy. Identifying $\Delta H^{\ddagger}$ as the activation energy (E_a), the TST rate constant can be expressed by Arrhenius' law, $k_{TST} = A\ e^{-E_a/k_B T}$, with $A = \frac{k_B T}{h} e^{\Delta S^{\ddagger}/k_B}$ the rate constant for the barrierless case (i.e., when $\Delta H^{\ddagger} = E_a = 0$).

Deviations from TST and the Arrhenius law occur when the assumptions of these theories become invalid.[168, 169] Recrossing events and quantum phenomena like tunneling, quantum interference, and zero-point energy effects can lead to deviations from TST by introducing reactive pathways beyond classical barrier crossing.[170] Some of those deviations can be approximately accounted for by the transmission coefficient κ, modifying the reaction rate constant to $k = \kappa k_{TST}$. This approach assumes that the reaction dynamics follows rate kinetics with a single well-defined rate constant. Another breakdown of TST occurs when the concept of a rate constant becomes invalid, such as when the barrier height is comparable to $k_B T$ or when the coupling between the reaction coordinate and other non-reactive molecular degrees of freedom (DOF) is weak.[171] These forms of TST breakdown often stem from the inherently quantum-mechanical nature of chemical dynamics.[172, 173, 174]

A prime example of an elementary chemical reaction of fundamental biological importance, which is often modeled using a double-well potential energy surface, is the adenine-thymine proton transfer reaction in DNA. [175, 176, 177] The free energy profile for this reaction varies with physiological conditions. Under normal cell conditions, the profile favors the hydrogen-bonded adenine-thymine complex form. However, during cell replication, this hydrogen bond must be broken to allow the DNA strands to duplicate. Proton transfer during this process has been suggested to cause spontaneous mutations due to bases occasionally adopting less likely tautomeric forms. [178] Therefore, simulating the dynamics

of proton transfer in the adenine-thymine complex across a broad range of double-well free energy profiles can provide insights into the potential influence of quantum effects on the interconversion between tautomeric forms of the bases.

The traditional method for testing and validating chemical rate theories, including both TST/Arrhenius and post-TST/non-Arrhenius approaches, has relied on extensive experimental measurements of chemical dynamics across a diverse range of molecular systems and external conditions to cover both chemical space and parameters influencing chemical dynamics, such as temperature and the interactions between the reaction coordinate and the non-reactive DOF. However, this approach is highly challenging and labor-intensive. This is because experimentally monitoring reactant and product populations in real time may prove difficult, and changing from one chemical system to another often involves altering multiple parameters with complex and sometimes opposite effects. A notable example of the difficulty of this traditional approach is the 30-year delay between the theoretical prediction of the inverted region in the Marcus rate theory for electron transfer reactions and its experimental validation. [179, 180, 181]

A promising alternative for experimentally testing and validating chemical rate theories has emerged with the advent of controllable and highly tunable fully quantum-mechanical platforms. These platforms can allow the exploration of quantum dynamics in various complex model systems across a broad range of parameter space.[37, 38, 3] Considering that chemical dynamics is inherently quantum mechanical in nature and that the most underexplored regimes of chemical dynamics exhibit significant quantum effects, these platforms can offer valuable simulation tools to investigate chemical reactivity under conditions that could be challenging for spectroscopic methods applied to molecular systems.[38]

Recent studies that exemplify this innovative approach of using quantum devices to explore chemical reactivityinclude the use of an ion trap platform as an analog simulator of the chemical dynamics underlying redox electron transfer reactions. [182, 183] Marcus theory, which describes the electron transfer rate constant with a double-well model, is analogous to TST for non-redox chemical reactions. It employs a TST-like argument with an Arrhenius-type expression for the rate constant.[5] In Marcus theory, the transition state is the molecular configuration at the crossing point between the diabatic free energy profiles of the donor (reactant) and acceptor (product) states along the reaction coordinate associated with the reorganization of the nuclear DOF upon electron transfer. Like TST, Marcus theory treats the activation to the transition state as a classical process and assumes weak electronic coupling between the donor and acceptor states. Schlawin et al. demonstrated that an ion-trap device could reproduce the predictions of Marcus theory, including the inverted regime. [182] They also showed how this device could explore deviations from Marcus

theory because of quantum (low-temperature) and strong electronic coupling effects. This enables the study of unconventional electron transfer regimes that are challenging to capture using traditional methods.

In this chapter, we propose a novel strategy for simulating the dynamics of elementary reactions using a quantum platform. We explore the superconducting circuit quantum electrodynamics (cQED) Kerr-cat device. [36, 33, 184, 34, 185, 186, 187, 3] We begin by introducing the Kerr-cat device and highlighting the features that make it ideally suited for analog simulations of chemical dynamics. Next, we consider examples of molecular systems to demonstrate its capabilities as applied to simulating proton transfer dynamics.

4.3 Kerr-Cat Device and Effective Hamiltonian

We begin by considering the effective Hamiltonian of the cQED Kerr-cat device, which constitutes of an arrangement of a few Josephson junctions schematically shown in Fig. 4.1: [36, 188]

$$\hat{H}_{KC} = \Delta \hat{a}^\dagger \hat{a} - K(\hat{a}^\dagger)^2(\hat{a})^2 + \epsilon_2(\hat{a}^2 + \hat{a}^{\dagger 2}) + \epsilon_1(\hat{a} + \hat{a}^\dagger). \tag{4.1}$$

Here, $\hat{a}^\dagger$ and $\hat{a}$ are the ladder operators for the device bosonic mode, satisfying the usual bosonic commutator relation $[\hat{a}, \hat{a}^\dagger] = 1$. The Hamiltonian $\hat{H}_{KC}$ includes adjustable parameters, namely the Kerr non-linearity, K, the detuning parameter, Δ, and the drive coefficients, ϵ_1 and ϵ_2. These parameters can be experimentally altered by adjusting the magnetic flux and the amplitudes and frequencies of the microwave drives within the quantum device.[4]

Following Venkatraman et al., [33] we assume that the noisy dynamics of the device can be described by the following Lindblad equation:

$$\frac{\partial \hat{\rho}}{\partial t} = -\frac{i}{\hbar}[\hat{H}_{KC}, \hat{\rho}] + \kappa\ (1 + n_{\text{th}}) \left(\hat{a}\hat{\rho}\hat{a}^\dagger - \frac{1}{2} \left\{ \hat{a}^\dagger \hat{a}, \hat{\rho} \right\} \right) + \kappa\ n_{\text{th}} \left(\hat{a}^\dagger \hat{\rho} \hat{a} - \frac{1}{2} \left\{ \hat{a}\hat{a}^\dagger, \hat{\rho} \right\} \right), \tag{4.2}$$

where κ sets the photon loss rate corresponding to an effective dissipation rate due to coupling of the system with a surrounding environment and n_{th} defines the effective temperature. Like $\{K, \Delta, \epsilon_1, \epsilon_2\}$, the parameters κ and n_{th} are experimentally tunable and determine the noise associated with the experimental device. [189]

Consider also the model Hamiltonian for systems with a double-well potential energy surface given by

$$\hat{H}_{DW} = \frac{\hat{p}^2}{2m} + k_4\hat{x}^4 - k_2\hat{x}^2 + k_1\hat{x}, \tag{4.3}$$

which is commonly used to simulate hydrogen bonded complexes. [175] The position and

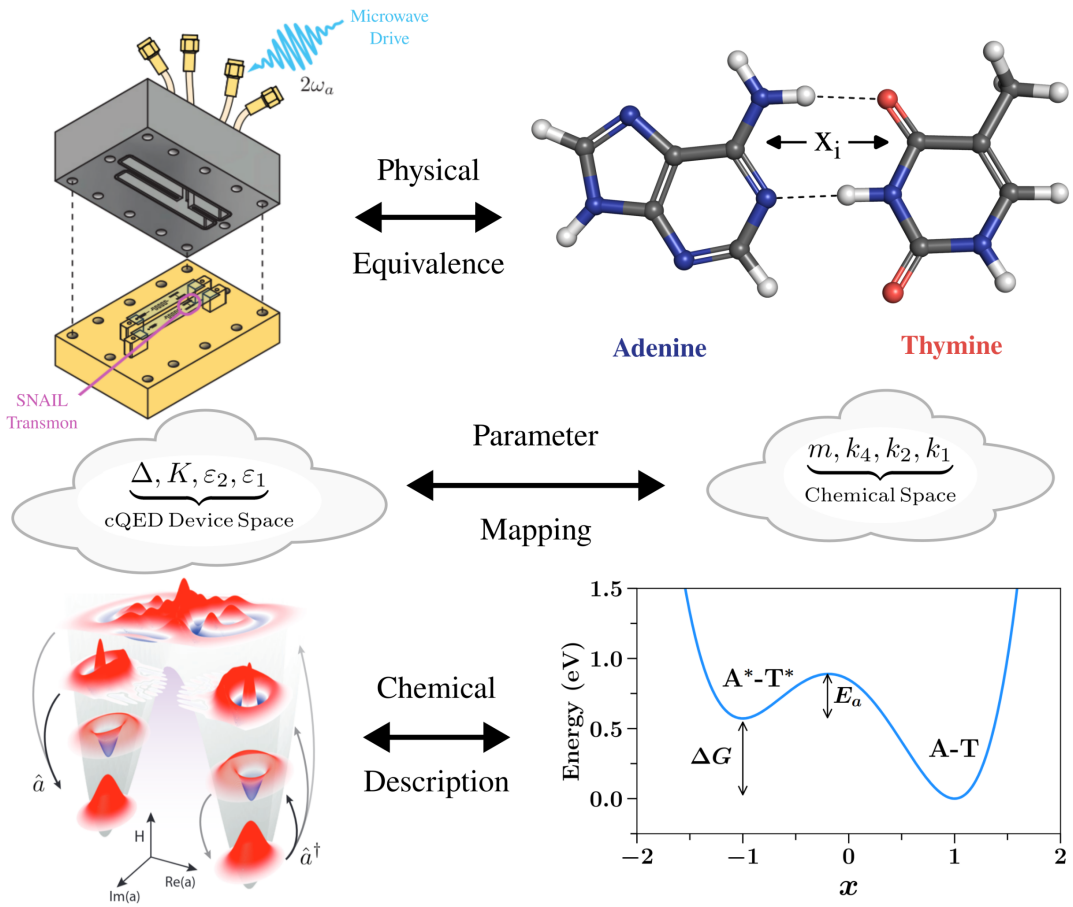


Figure 4.1: Schematic of Bosonic cQED Device for Quantum Dynamics Simulations in Hydrogen-Bonded Complexes. Adapted from Ref. 3. Copyright (2024) American Chemical Society. The device is a half-aluminum, half-copper cavity resonator containing two sapphire chips with a SNAIL-transmon, readout resonator, and Purcell filter (top left).[4] A strong microwave drive at twice the resonance frequency converts the SNAIL-transmon Hamiltonian into the bi-stable Kerr-cat parametric oscillator Hamiltonian for analog simulations of quantum dynamics in molecular systems, such as the adenine-thymine dimer (top right). Parameters $\Delta, K, \epsilon_1, \epsilon_2$ (middle left) are adjusted to map the effective Hamiltonian $\hat{H}_{KC}$ to the double-well Hamiltonian modeling the molecular system (middle right). The bottom left shows the Wigner transform phase space representation of the device quantum states, which are analogous to the states in molecular the double-well potential in the bottom right.

momentum operators of the reaction coordinate, $\hat{x}$ and $\hat{p}$, satisfy the commutation relation $[\hat{x}, \hat{p}] = i\hbar$. In the equation above, m represents the effective mass associated with motion along the reaction coordinate. The parameters $\{k_1, k_2, k_4\}$ are positive and real, typically determined by fitting the ab initio potential energy surface. This fitting process ensures the accurate representation of the barrier height, the curvature of the surface at the reactant

and product wells, and the relative stability of reactants and products as parametrized by k_1. Table 4.1 lists the parameters $\{k_1, k_2, k_4\}$ used in this study for numerical simulations of proton transfer dynamics (with $m = 1836$ amu) in the four model systems illustrated in Fig. 4.2.

System	k_4 [E_h/a_0^4]	k_2 [E_h/a_0^2]	k_1 [E_h/a_0]
Adenine-Thymine (DNA) [190]	1.4×10^{-3}	1.08×10^{-2}	5.2×10^{-3}
Guanine-Cytosine (DNA) [15]	7.7×10^{-4}	6.9×10^{-3}	4.5×10^{-3}
Malonaldehyde (cis-trans) [191, 192]	9.4×10^{-5}	3.0×10^{-3}	2.9×10^{-3}
Malonaldehyde (cis-cis) [191, 192]	7.1×10^{-4}	4.0×10^{-3}	0

Table 4.1: Parameters used to simulate double-well potentials for proton transfer in molecular systems, according to the equation $V = k_4 x^4 - k_2 x^2 + k_1 x$.

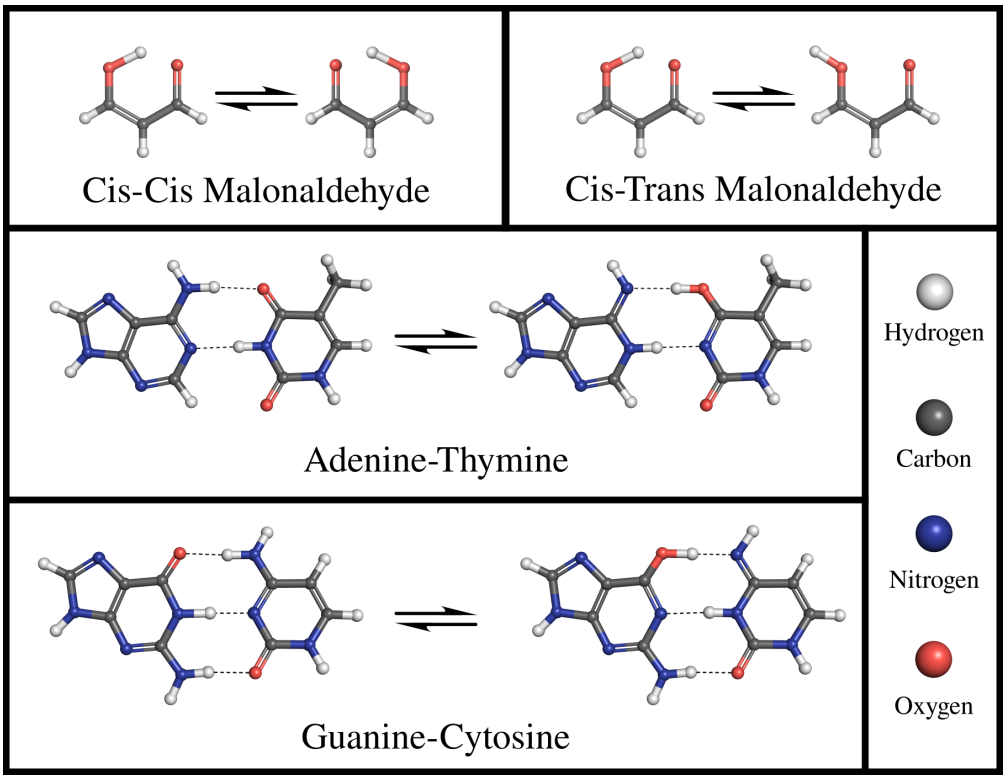


Figure 4.2: Hydrogen bonded complexes studied to analyze intramolecular proton transfer in cis-cis and cis-trans malonaldehyde (top), intramolecular proton transfer in adenine-thymine (amine, pyrimidine) (middle), and guanine-cytosine (amine, pyrimidine) base pairs.

The next step is to map the Kerr-cat Hamiltonian, introduced in Eq. (4.1), onto the model Hamiltonian of the molecular system presented in Eq. (4.3). This requires mapping the photonic operators, $\{\hat{a}, \hat{a}^\dagger\}$, onto the reaction coordinate operators, $\{\hat{x}, \hat{p}\}$. To ensure

the correct dynamics, this mapping must preserve the commutation relations: $[\hat{x}, \hat{p}] = i\hbar$ and $[\hat{a}, \hat{a}^\dagger] = \hat{1}$. A mapping that satisfies these conditions is given by:

$$\hat{a} = \frac{1}{\sqrt{2}}\left(\frac{1}{c}\hat{x} + \frac{ic}{\hbar}\hat{p}\right), \qquad \hat{a}^\dagger = \frac{1}{\sqrt{2}}\left(\frac{1}{c}\hat{x} - \frac{ic}{\hbar}\hat{p}\right), \tag{4.4}$$

where c is an arbitrary parameter with the same units as $\hat{x}$. Thus, the mapping of $\{\hat{a}, \hat{a}^\dagger\}$ onto $\{\hat{x}, \hat{p}\}$ is not unique. This flexibility in choosing c plays a crucial role in mapping the Kerr-cat Hamiltonian in Eq. (4.1) onto the chemical double-well Hamiltonian in Eq. (4.3). It should be noted that the value of c can be equivalent to the zero-point spread, $\sqrt{\hbar Z}$, if we define $\hat{x}$ and $\hat{p}$ as in reference 33.

Substituting the expressions for $\hat{a}$ and $\hat{a}^\dagger$ in terms of $\hat{x}$ and $\hat{p}$ from Eq. (4.4) into Eq. (4.1), we can recast the negative of the Kerr-cat Hamiltonian in terms of $\hat{x}$ and $\hat{p}$, omitting constant terms that do not impact the dynamics:

$$\begin{aligned} -\hat{H}_{KC} = &\frac{c^2}{\hbar^2}\left(\epsilon_2 - K - \Delta/2\right)\hat{p}^2 + \frac{K}{4c^4}\hat{x}^4 - \frac{1}{c^2}\left(\epsilon_2 + K + \Delta/2\right)\hat{x}^2 - \frac{\epsilon_1\sqrt{2}}{c}\hat{x} \\ &+ \frac{Kc^4}{4\hbar^4}\hat{p}^4 + \frac{K}{4\hbar^2}\left(\hat{x}^2\hat{p}^2 + \hat{p}^2\hat{x}^2\right). \end{aligned} \tag{4.5}$$

Comparing Eq. (4.5) with Eq. (4.3), we see that while $-\hat{H}_{KC}$ includes $\hat{p}^2$, $\hat{x}^4$, $\hat{x}^2$ and $\hat{x}$ terms that can be mapped to the corresponding terms in the chemical double-well Hamiltonian (Eq. (4.3)), it also contains additional terms ($\hat{p}^4$, $\hat{x}^2\hat{p}^2$ and $\hat{p}^2\hat{x}^2$) that are absent in Eq. (4.3).

We now map the parameters $\{\Delta, K, \epsilon_2, \epsilon_1\}$ onto $\{m, k_1, k_2, k_4\}$ by ensuring consistency between the $\hat{p}^2$, $\hat{x}^4$, $\hat{x}^2$ and $\hat{x}$ terms in Eqs. (4.3) and (4.5). This leads to the following mapping relations:

$$K = 4c^4 k_4, \tag{4.6}$$

$$\epsilon_2 = \frac{\hbar^2}{4c^2 m} + \frac{c^2 k_2}{2}, \tag{4.7}$$

$$\Delta = -\frac{\hbar^2}{2c^2 m} + c^2 k_2 - 8c^4 k_4, \tag{4.8}$$

$$\epsilon_1 = -\frac{ck_1}{\sqrt{2}}. \tag{4.9}$$

Clearly, according to Eqs. (4.6)-(4.9), the values of $\{K, \Delta, \epsilon_1, \epsilon_2\}$ depend on the value of c. We then utilize the flexibility in choosing the value of c to minimize the effect of the additional terms $\hat{p}^4$, $\hat{x}^2\hat{p}^2$ and $\hat{x}^2\hat{p}^2$ in Eq. (4.3). As demonstrated in the SI, this requires

choosing a value of c small enough to satisfy the following inequality:

$$\frac{\hbar^2}{mk_2c^4} \gg 1. \tag{4.10}$$

Next, we compare the energy levels of the Kerr-cat and double-well Hamiltonians, given by Eq. (4.5) and Eq. (4.3), respectively. In general, these energy levels are expected to be different due to the additional terms $\hat{p}^4$, $\hat{x}^2\hat{p}^2$ and $\hat{p}^2\hat{x}^2$ of the Kerr-cat Hamiltonian that are missing in the double-well Hamiltonian. However, the deviations between the energy levels of both Hamiltonians are expected to decrease as c becomes smaller [see Eq. (4.10) and Fig. 4.4, which is explained below].

To establish an acceptable value of c, we set the tolerance for deviations between the energy levels of the Kerr-cat and double-well Hamiltonians at 1.5 $\mathrm{mE_h}$ = 0.941 kcal mol^{-1}, a standard measure of chemical accuracy. It is crucial to note that accurate descriptions of barrier crossing dynamics require this level of accuracy not only for the ground state but also for energy levels up to the top of the barrier.

For example, the number of states required to capture accurate dynamics in the molecular model systems analyzed in this work is as follows: 6 for cis-cis malonaldehyde (Fig. 4.3.A), 24 for cis-trans malonaldehyde (Fig. 4.3.B), 12 for adenine-thymine (Fig. 4.3.C), and 14 for guanine-cytosine (Fig. 4.3.D). Ensuring that the energy levels of the Kerr-cat device, E_{KC}, and chemical double-well Hamiltonians, E_{DW}, are within chemical accuracy of each other ($E_{KC} - E_{DW}$ is below the horizontal dashed line in the panels I of Fig. 4.4) also results in excellent agreement between their corresponding eigenfunctions, as shown in Fig. 4.3.

Using the cQED device to encode $\hat{H}_{\mathrm{DW}}$ requires a finite, non-zero value for the Kerr nonlinearity K, so the units of Δ, ϵ_2 and ϵ_1 are expressed in terms of K. For vanishingly small values of c, the ratios $\frac{\Delta}{K}$,$\frac{\epsilon_2}{K}$, and $\frac{\epsilon_1}{K}$ become very large (panels II of Fig. 4.4), so they are experimentally unfeasible with current cQED platforms. [4] However, there exists a range of values of c for which the parameters are experimentally accessible, while maintaining a useful degree of accuracy for the energies and stationary states. In particular, the Hamiltonian for the cis-cis malonaldehyde is both experimentally accessible and meets the chemical accuracy criterion for stationary states and energies (see Fig. 4.4A). Chemical systems with asymmetric free energy profiles pose greater challenges due to the higher number of eigenstates required for addressing kinetic questions. Expanding the range of experimental parameters could enable an accurate simulation of these more challenging double-well problems, although it may also risk a breakdown of the effective Hamiltonian approximation.[4]

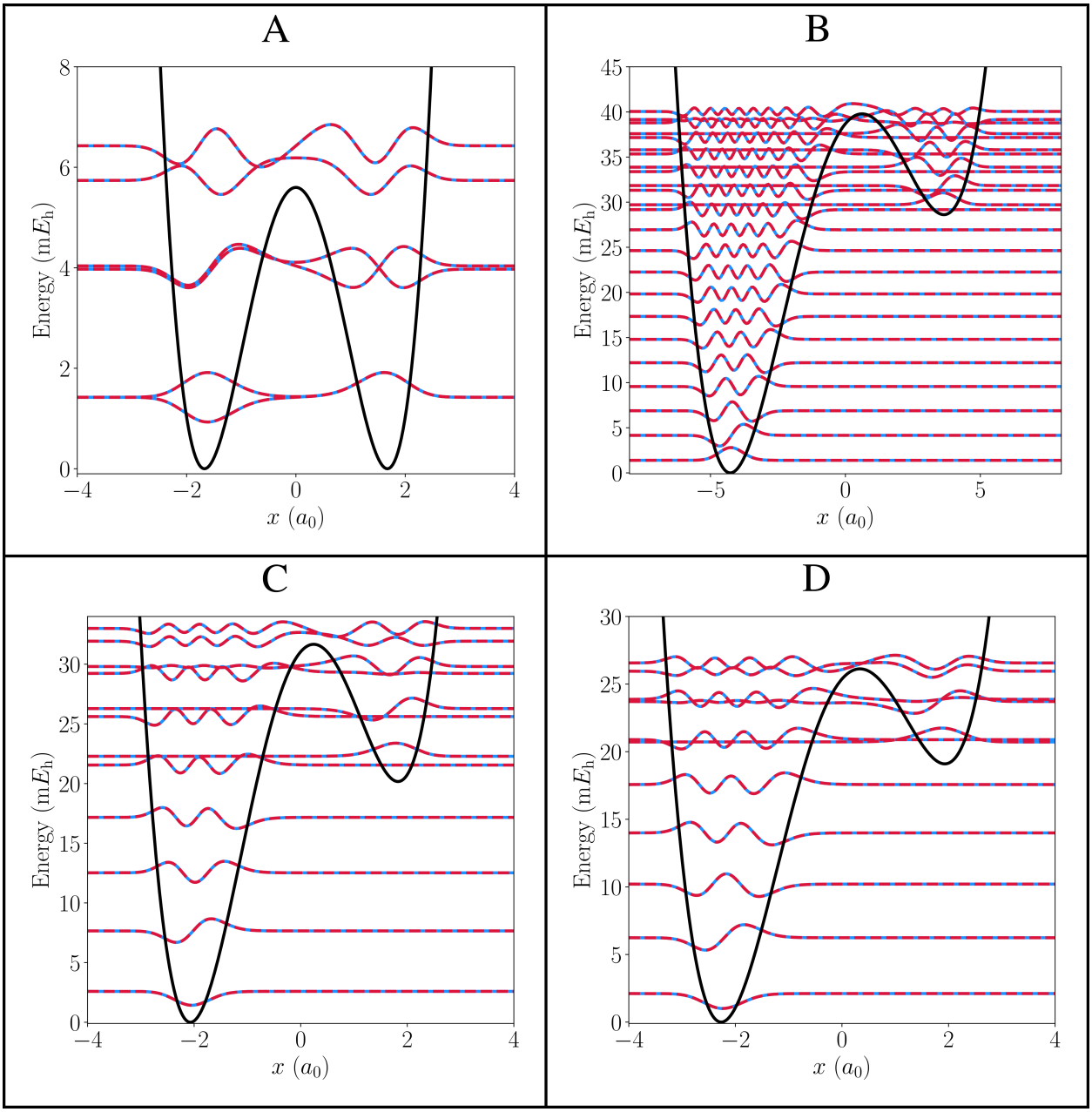


Figure 4.3: Eigenstates obtained by diagonalization of the model Hamiltonians for cis-cis malonaldehyde (A), cis-trans malonaldehyde (B), adenine-thymine (C), and guanine-cytosine (D), based on either the chemical double-well Hamiltonian (blue) or the Kerr-cat Hamiltonian (red) with $c = 0.1\,\mathrm{a_0}$. Eigenstates are shown together with the potential energy surface as a function of the reaction coordinate 'x'.

4.4 Device Dynamics versus Chemical Dynamics

Consistency between the energy levels of the $\hat{H}_{KC}$ and $\hat{H}_{DW}$ Hamiltonians is necessary, but not sufficient to ensure that analog simulations on the Kerr-cat device accurately capture

the chemical dynamics. This is because the reaction rate is also influenced by the coupling of the reaction coordinate to the thermal bath of nonreactive DOF. Consequently, the actual reaction rate constant depends not only on the eigenvalues and eigenfunctions of the Hamiltonian but also on the temperature and dissipation rate of the bath. Therefore, being able to simulate chemical dynamics on the Kerr-cat device requires that the dynamics of the device be dissipative (noisy), which is indeed the case. The noisy dynamics of Kerr-cat device are described by the Lindblad equation in Eq. (4.2) with adjustable photon loss rate constant κ and temperature set by n_{th}.

In what follows, we consider a chemical system that experiences the same type of dissipation as the Kerr-cat device. This dissipative model is useful as it results in chemical dynamics characterized by a reaction rate constant. However, other dissipation models could also be useful, as long as they capture the dissipation of the chemical system typically determined by the nature of its chemical environment and the way the reaction coordinate is coupled to the environment (e.g., the surrounding can correspond to liquid solution, biological environment, or solid-state environment). Hence, characterizing the dissipation of specific chemical systems and replicating it on a Kerr-cat device remains a subject of future studies that will focus on bath engineering. [193, 194] It is noteworthy that Markovian and exotic dissipative channels can be engineered to a great extent in circuit QED [195]. The strength of dissipation in the squeezed Kerr oscillator experiment of Frattini and coworkers[36] is, for example, readily tunable by the amplitude of the microwave readout drive, and exotic forms of dissipation have been already demonstrated [196, 197].

Assuming that the chemical system undergoes the same type of dissipation as the Kerr-cat device, we use Eq. (4.4) to express the dissipator in Eq. (4.2) in terms of the operators $\hat{x}$ and $\hat{p}$, which form the basis of the chemical double-well Hamiltonian in Eq. (4.3). This results in the following Lindblad equation for the chemical system:

$$\begin{aligned}\frac{\partial\hat{\rho}}{\partial t} = &-\frac{i}{\hbar}[\hat{H}_{DW},\hat{\rho}] + \frac{\kappa\,(1+2n_{\mathrm{th}})}{4}\left[\frac{1}{c^2}\left([\hat{x}\hat{\rho},\hat{x}]+[\hat{x},\hat{\rho}\hat{x}]\right)+\frac{c^2}{\hbar^2}\left([\hat{p}\hat{\rho},\hat{p}]+[\hat{p},\hat{\rho}\hat{p}]\right)\right]\\ &-\frac{i\kappa}{4\hbar}\left([\hat{x}\hat{\rho},\hat{p}]+[\hat{x},\hat{\rho}\hat{p}]-[\hat{p}\hat{\rho},\hat{x}]-[\hat{p},\hat{\rho}\hat{x}]\right). \qquad (4.11)\end{aligned}$$

The complete methodology for the numerical simulation of the open quantum dynamics is outlined in the SI. Here, we clarify that the initial state for dynamics propagation is localized in the reactant well of the above-mentioned chemical reactions. To generate this state, we diagonalize the system Hamiltonian and select the first eigenstate with more than 50% density in the reactant well. We then apply a sigmoidal filter function to remove the excess density outside of it (see SI for implementation details). This general localization

method typically creates a localized Gaussian state and avoids the need to identify the critical points of each potential energy surface. By integrating Eq. (4.11) with an initial state $\hat{\rho}(0)$ localized in the reactant well, we obtain the time-evolved state $\hat{\rho}(t)$, which can be used to compute the product population at time t, as follows:

$$P_P(t) = \mathrm{Tr}\{\hat{\rho}(t)\hat{\Theta}_X\}, \tag{4.12}$$

where $\hat{\Theta}_X$ is the Heaviside function:

$$\langle x|\hat{\Theta}_X|x'\rangle = \begin{cases} 0 & \text{for } x < 0, \\ \delta(x - x') & \text{for } x > 0. \end{cases} \tag{4.13}$$

The reactant-to-product reaction rate constant, $k = 1/T_X$, is obtained by fitting $P_P(t)$ to an exponential decay, as described below. The top subpanels of Fig. 4.5 show the time evolution of $P_P(t)$ for the four proton transfer reactions – cis malonaldehyde, cis-trans malonaldehyde, adenine-thymine, and guanine-cytosine – obtained by solving Eq. (4.11) for different values of c (solid lines). These top subpanels also include results where the chemical double-well Hamiltonian in Eq. (4.11), $\hat{H}_{DW}$, is replaced by the corresponding device Hamiltonian $-\hat{H}_{KC}$ with additional terms $\hat{p}^4$, $\hat{x}^2\hat{p}^2$ and $\hat{p}^2\hat{x}^2$ (diamonds). The bottom subpanels of Fig. 4.5 show the dependence of the inverse reaction rate constant, T_X, on c for both $\hat{H}_{DW}$ (solid line) and $-\hat{H}_{KC}$ (diamonds).

A close examination of the results in Fig. 4.5 reveals that the dynamics of both the chemical system and the Kerr-cat device align well with the rate kinetics described by a rate constant. Additionally, the reaction rate constant shows significantly less sensitivity to the value of c compared to the energy levels and eigenfunctions of $\hat{H}_{DW}$ and $\hat{H}_{KC}$. Specifically, the rate constant predicted by the device matches that predicted for the chemical system at values of c as high as 0.4 a_0, much higher than the value of $c = 0.1\,\mathrm{a}_0$ required to match energy levels and eigenfunctions near the top of the barrier. This is likely due to the effect of dissipation, making the overall dynamics less sensitive to small differences in the potential energy surface.

The results in Fig. 4.5 were obtained with $\kappa = 0.1$ and $n_{\mathrm{th}} = 0.1$, which are illustrative of the dissipation on the quantum device. However, the observed trends are insensitive to these specific values, as demonstrated by the rate constants obtained for various values of κ and n_{th} shown in Table 4.2 for $c = 0.1\,\mathrm{a}_0$. As expected, T_X increases (i.e., the reaction slows down) when κ and n_{th} decrease. Nonetheless, the actual values of T_X for the chemical double-well and the Kerr-cat device are consistent, regardless of the κ and n_{th} values.

Dissipation Constants (κ, n_{th})	$(0.1, 0.1)$	$(0.1, 0.05)$	$(0.025, 0.1)$	$(0.025, 0.05)$
Cis-cis Malonaldehyde (KC)	91 ± 1	91 ± 1	303 ± 4	295 ± 4
Cis-cis Malonaldehyde (DW)	91 ± 1	91 ± 1	303 ± 4	295 ± 4
Cis-trans Malonaldehyde (KC)	147 ± 2	142 ± 2	527 ± 7	499 ± 6
Cis-trans Malonaldehyde (DW)	147 ± 2	142 ± 2	528 ± 7	500 ± 6
Adenine-Thymine (KC)	95 ± 1	94 ± 1	323 ± 4	314 ± 4
Adenine-Thymine (DW)	95 ± 1	94 ± 1	323 ± 4	314 ± 4
Guanine-Cytosine (KC)	96 ± 1	95 ± 1	325 ± 4	316 ± 4
Guanine-Cytosine (DW)	96 ± 1	95 ± 1	325 ± 4	316 ± 4

Table 4.2: Table of inverse reaction rate constants T_X (in $\hbar/\mathrm{E_h}$) for each chemical system obtained with the $\hat{H}_{DW}$ and $\hat{H}_{KC}$ Hamiltonians, for various κ and n_{th} values with $c = 0.1\,\mathrm{a_0}$

4.5 Concluding Remarks

In this chapter, we proposed a novel approach to simulating chemical dynamics using a tunable Kerr-cat quantum device. This method allows for precise control over the parameters defining double-well potential energy surfaces, as well as external factors such as temperature and dissipation rates. We demonstrated the efficacy of this approach by applying it to proton transfer in four prototypical hydrogen-bonded model complexes, showing that the underlying chemical dynamics can be accurately simulated on a quantum device.

Simulating chemical dynamics on a Kerr-cat device requires overcoming several challenges. A primary challenge, addressed in this chapter, is mapping the chemical double-well Hamiltonian onto the Kerr-cat device Hamiltonian. This mapping is nontrivial, because the Kerr-cat device Hamiltonian includes additional terms ($\hat{p}^4$, $\hat{x}^2\hat{p}^2$ and $\hat{p}^2\hat{x}^2$), that are absent in the chemical Hamiltonian. We resolved this challenge by introducing a method that minimizes the impact of those additional terms by adjusting the parameter c in the mapping of the photonic operators $\hat{a}$ and $\hat{a}^\dagger$ to the chemical operators $\hat{x}$ and $\hat{p}$. Specifically, we demonstrated that the energy levels and stationary states of the Kerr-cat and chemical Hamiltonians can be aligned (within chemical accuracy tolerance) by selecting a sufficiently small value of c. Furthermore, we found that reaction rate constants are even less sensitive to the value of c than the energy levels and stationary states, making them easier to reproduce when simulating chemical dynamics on the Kerr-cat device.

The approach proposed in this chapter represents a significant first step towards enabling simulations of chemical dynamics on bosonic quantum simulators, which is beyond the capabilities of currently available NISQ computers. Remaining challenges include characterizing and engineering dissipation, and designing devices that can reliably emulate more complex free energy surfaces beyond the one-dimensional asymmetric double-well free energy sur-

faces considered in this chapter. Ongoing work addressing these challenges will be reported in future papers, paving the way for even more advanced simulations of quantum chemical dynamics on quantum devices.

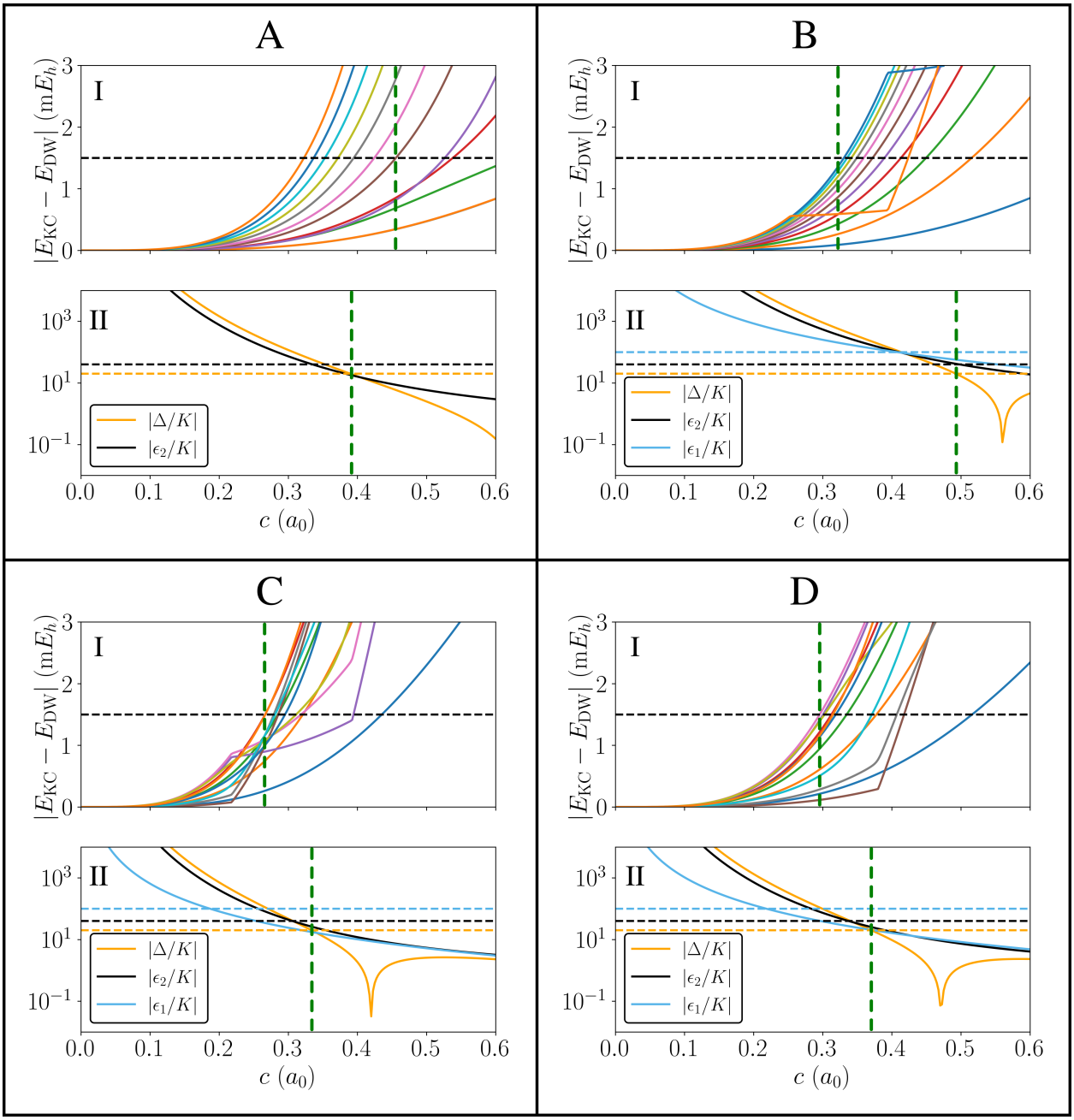


Figure 4.4: Absolute energy differences for the lower lying eigenstates of the chemical double-well and Kerr-cat Hamiltonian (panels I) and cQED device parameters (panels II) as a function of the scaling parameter c for cis-cis malonaldehyde (A), cis-trans malonaldehyde (B), adenine-thymine (C) and guanine-cytosine (D). The horizontal black dashed line in panels I indicates the threshold of chemical accuracy at 1.5 $\mathrm{mE_h}$. The horizontal dashed lines in panels II indicate the maximum values of the parameters available in current cQED devices. The vertical dashed line indicates the maximum value of c recommended for accurate dynamics simulations (panels I) and minimum value of c ensuring experimental parameters available in existing cQED Kerr-cat platforms (panels II). [4]

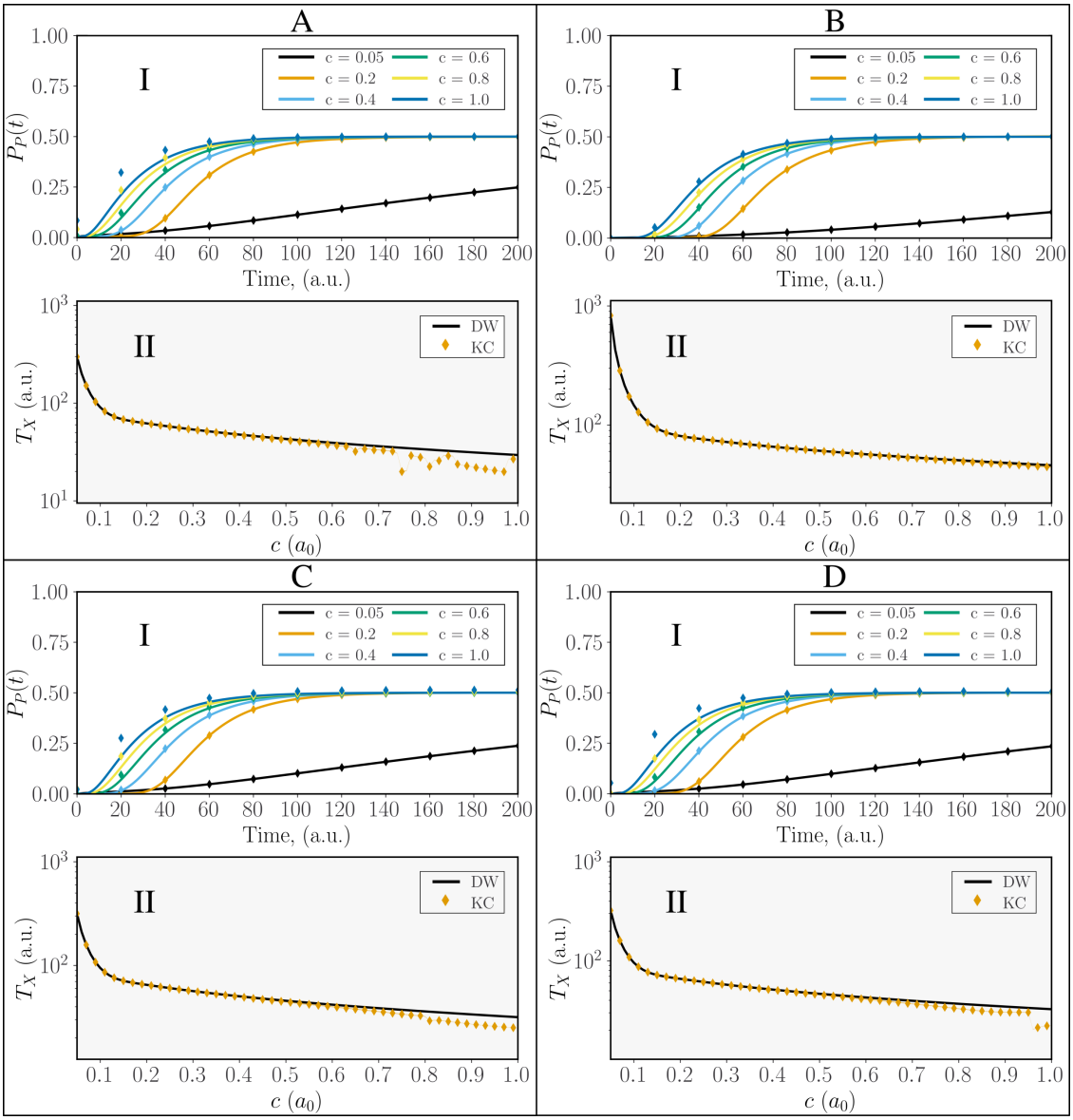


Figure 4.5: Comparison of observables obtained with $\hat{H}_{DW}$ (solid lines) and $\hat{H}_{KC}$ (diamonds) as a function of c, using $\kappa = 0.1$ and $n_{\text{th}} = 0.1$, for cis-cis malonaldehyde (A), cis-trans malonaldehyde (B), adenine-thymine (C) and guanine-cytosine (D). The time evolution of the product population is shown in the top subpanels (I), while the corresponding inverse reaction rate constants are shown in the bottom subpanels (II).

CHAPTER 5

Conclusion

5.1 Summary

Quantum devices provide a promising avenue for simulating chemically relevant systems. Realizing this potential requires both continued refinement of theoretical frameworks for chemical reaction dynamics and the development of hardware and algorithms compatible with their structure. In this dissertation, we advance both directions by developing open-system theoretical descriptions and constructing digital and analog quantum strategies tailored for their implementation.

A central theme of this work is the use of quantum master equations (QMEs) as a compact and efficient framework for incorporating environmental effects. QMEs enable the reduction of high-dimensional condensed-phase systems to effective dynamical descriptions, in which non-reactive modes are integrated out while their influence on the reactive subsystem is retained.

In Chapter 2, we develop a nonequilibrium Fermi's Golden Rule (NE-FGR) framework that incorporates cavity effects using only cavity-free inputs. We further derive an Instantaneous Marcus Theory (IMT) expression that closely reproduces the full NE-FGR dynamics at significantly reduced computational cost while preserving a simple physical interpretation. This work bridges the gap between prior studies of cavity-modified equilibrium Fermi's Golden Rule[140] and cavity-free nonequilibrium Fermi's Golden Rule.[198, 54]

We apply this framework to a condensed-phase charge-transfer reaction, $\pi\pi^* \rightarrow$ CT1, in the CPC_{60} molecular triad dissolved in tetrahydrofuran and coupled to a single electromagnetic cavity mode. The dynamics are initiated from the ground-state nuclear distribution on the donor potential energy surface, consistent with photoexcitation under nonequilibrium conditions. These results demonstrate that cavity–matter coupling can substantially modify nonequilibrium charge-transfer kinetics in condensed-phase systems.

In Chapter 3, we address the problem of implementing open-system models, such as those

developed in Chapter 2, on digital quantum hardware. Previous approaches to simulating open-system dynamics on quantum devices relied on substantial classical preprocessing, including explicit time propagation and factorization of the propagator prior to dilation.[50, 49]

Here, we eliminate this separation between classical integration and quantum time evolution by deriving differential equations for the singular value decomposition (SVD) factors of the propagator and transferring the propagation procedure itself to the quantum device. The resulting algorithm remains broadly applicable to linear nonautonomous ordinary differential equations while significantly reducing the classical overhead associated with propagation.

In Chapter 4, we explore the use of analog quantum devices as a platform for simulating chemically relevant reaction dynamics. To this end, we construct a mapping between parametrically driven bosonic Kerr-cat devices and effective chemical Hamiltonians. Specifically, we show that, in the limit of small c, the device Hamiltonian approximates a double-well potential characteristic of ground-state chemical reaction landscapes. This mapping enables the simulation of benchmark reactions, including double proton transfer in hydrogen-bonded DNA base pairs.

Crucially, dissipation arises naturally from the coupling between the bosonic mode and its environment, yielding an effective Lindbladian description and the emergence of rate kinetics without additional engineering. Together, these results demonstrate that currently accessible superconducting bosonic devices can directly realize open-system chemical dynamics, establishing a concrete pathway toward analog quantum simulation of chemically relevant processes.

Taken together, the results of this dissertation establish complementary digital and analog quantum strategies for the simulation of chemically relevant open-system dynamics. The development of nonequilibrium rate theory for cavity-modified reactions, the formulation of a quantum-compatible propagation algorithm for linear nonautonomous ODEs, and the mapping of chemical double-well potentials onto bosonic Kerr-cat hardware collectively demonstrate that chemically grounded models can be systematically adapted to emerging quantum platforms. These contributions clarify both the theoretical structure of the underlying dynamics and the practical considerations required for their implementation on modern quantum devices.

5.2 Outlook

The research directions developed in this dissertation open several promising avenues for future work. The simulation of chemical dynamics remains a natural and compelling application of quantum hardware, as the exponential dimensionality of quantum mechanical

systems makes them particularly well suited for quantum representations. Realizing this potential requires continued development of both theoretical frameworks for describing chemical systems and practical methods for implementing those frameworks on quantum devices.

The theory of nonequilibrium chemical dynamics in optical cavities developed in Chapter 2 admits several important extensions. One key direction is the generalization of the nonequilibrium Fermi's Golden Rule (NE-FGR) framework to collectively coupled systems, in which many molecules interact with a common cavity mode. This would enable the treatment of experimentally relevant regimes where light–matter coupling is enhanced by collective effects, scaling as $\sqrt{N}$ with the number of molecules N.[199]

Another natural extension is to move beyond the single-mode approximation. In realistic settings, molecular systems interact not with an isolated cavity mode but with a structured photonic environment comprising multiple modes.[140] Moreover, these cavity modes are not perfectly isolated and must be coupled to a dissipative environment, leading to photon loss and additional decoherence channels.[200]

Taken together, these extensions would enable a unified theoretical framework that incorporates nonequilibrium preparation, collective coupling, multimode structure, and dissipation, thereby providing a more direct connection between microscopic theory and experimentally observed cavity-modified dynamics.

The framework developed in Chapter 3 for integrating nonautonomous linear ordinary differential equations can be extended in several directions. Most immediately, improving implementation efficiency is essential for simulations on current noisy hardware. In particular, Walsh–Gray decompositions can be employed to reduce circuit depth in the implementation of propagators,[201] especially when combined with error mitigation and correction techniques. This framework can then be applied to simulate the cavity-modified dynamics described in Chapter 2.

More broadly, the methodology may be generalized to treat time-convolution equations by embedding them into an enlarged Markovian space via pseudomode constructions.[202] This approach transforms nonlocal memory effects into local dynamics in an extended Hilbert space, thereby making them compatible with the quantum algorithm developed here.

Finally, the Kerr-cat platform explored in Chapter 4 presents substantial opportunities for refinement and expansion. A particularly important development would be the derivation of a Redfield-type quantum master equation starting from the full driven system–bath Hamiltonian. In this approach, the driven Hamiltonian would be transformed into an effective frame that removes the explicit drive-induced time dependence from the system Hamiltonian and transfers it to the system–bath coupling.[203] Treating this time-dependent coupling within a Redfield framework would replace the phenomenological dissipator with rates that satisfy

detailed balance, ensuring proper thermalization to the Boltzmann distribution.

Moreover, extending the Kerr-cat architecture to higher-dimensional, multimode systems would enable the simulation of fully anharmonic barrier-crossing dynamics involving multiple coupled degrees of freedom. Such extensions could ultimately access regimes of chemical dynamics that are intractable with classical computational methods.

Taken together, the projects presented in this dissertation establish a foundation for the systematic development of chemical theory on both digital and analog quantum platforms. Continued progress along these directions has the potential to bridge fundamental chemical dynamics with emerging quantum technologies.

BIBLIOGRAPHY

[1] Ningyi Lyu, Alessandro Miano, Ioannis Tsioutsios, Rodrigo Cortiñas, Kenneth Jung, Yuchen Wang, Zixuan Hu, Eitan Geva, Sabre Kais, and Victor S. Batista. Mapping molecular hamiltonians into hamiltonians of modular cqed processors. arXiv preprint arXiv:2306.06341, 2023.

[2] Louie Slocombe, Marco Sacchi, and Jim Al-Khalili. An open quantum systems approach to proton tunnelling in dna. arXiv preprint arXiv:2110.00113, 2021.

[3] Rishab Dutta, Delmar G. A. Cabral, Ningyi Lyu, Nam P. Vu, Yuchen Wang, Brandon Allen, Xiaohan Dan, Rodrigo G. Cortiñas, Pouya Khazaei, Max Schäfer, Alejandro C. C. d. Albornoz, Scott E. Smart, Scott Nie, Michel H. Devoret, David A. Mazziotti, Prineha Narang, Chen Wang, James D. Whitfield, Angela K. Wilson, Heidi P. Hendrickson, Daniel A. Lidar, Francisco Pérez-Bernal, Lea F. Santos, Sabre Kais, Eitan Geva, and Victor S. Batista. Simulating chemistry on bosonic quantum devices. J. Chem. Theory Comput., 20(15):6426–6441, Aug 2024.

[4] Alejandro Cros Carrillo de Albornoz, Rodrigo G. Cortiñas, Max Schäfer, Nicholas E. Frattini, Brandon Allen, Delmar G. A. Cabral, Pablo E. Videla, Pouya Khazaei, Eitan Geva, Victor S. Batista, and Michel H. Devoret. Oscillatory dissipative tunneling in an asymmetric double-well potential. arXiv:2409.13113, 2024. http://arxiv.org/abs/2409.13113 (accessed 2024-10-30).

[5] Abraham Nitzan. Chemical dynamics in condensed phases: relaxation, transfer and reactions in condensed molecular systems. Oxford University Press, New York, 2006.

[6] D. J. Tannor. Introduction to Quantum Mechanics: A Time Dependent Perspective. University Science Books, Sausalito, CA, 2006.

[7] Ellen Mulvihill, Kristina M. Lenn, Xing Gao, Alexander Schubert, Barry D. Dunietz, and Eitan Geva. Simulating energy transfer dynamics in the fenna–matthews–olson complex via the modified generalized quantum master equation. 154(20):204109.

[8] Zixuan Hu, Kade Head-Marsden, David A. Mazziotti, Prineha Narang, and Sabre Kais. A general quantum algorithm for open quantum dynamics demonstrated with the fenna-matthews-olson complex. 6:726.

[9] Belen Torrado, Bruno Pannunzio, Leonel Malacrida, and Michelle A. Digman. Fluorescence lifetime imaging microscopy. 4(1):80.

[10] M. H. Lee, B. D. Dunietz, and E. Geva. Calculation from first principles of golden-rule rate constants for photo-induced subphthalocyanine/fullerene interfacial charge transfer and recombination in organic photovoltaic cells. J. Phys. Chem. C, 118:9780–9789, 2014.

[11] Myeong H. Lee, Barry D. Dunietz, and Eitan Geva. Calculation from first principles of intramolecular golden-rule rate constants for photo-induced electron transfer in molecular donor–acceptor systems. 117(44):23391–23401.

[12] Myeong H. Lee, Barry D. Dunietz, and Eitan Geva. Donor-to-donor vs donor-to-acceptor interfacial charge transfer states in the phthalocyanine–fullerene organic photovoltaic system. 5(21):3810–3816.

[13] N. J. Tao. Electron transport in molecular junctions. 1(3):173–181.

[14] Abraham Nitzan and Mark A. Ratner. Electron transport in molecular wire junctions. 300(5624):1384–1389.

[15] Louie Slocombe, Marco Sacchi, and Jim Al-Khalili. An open quantum systems approach to proton tunnelling in DNA. 5(1):109.

[16] Dominik Marx. Proton transfer 200 years after von grotthuss: Insights from ab initio simulations. 7(9):1848–1870.

[17] Noam Agmon. The grotthuss mechanism. 244(5):456–462.

[18] H.P. Breuer and F. Petruccione. The Theory of Open Quantum Systems. Oxford Press, Oxford, 2002.

[19] Xiaohan Dan, Pouya Khazaei, Brandon C Allen, Ningyi Lyu, Callie Wilson, Ellen Mulvihill, Yuchen Wang, Saurabh Shivpuje, Sabre Kais, Victor S Batista, and Eitan Geva. QFlux: An open-source toolkit for quantum dynamics simulations on quantum computers. part VI - the generalized quantum master equation.

[20] E. Mulvihill, A. Schubert, X. Sun, B.D. Dunietz, and E. Geva. A modified approach for simulating electronically nonadiabatic dynamics via the generalized quantum master equation. J. Chem. Phys., 150:034101–20, 2019.

[21] E. Mulvihill and E. Geva. Simulating the dynamics of electronic observables via reduced-dimensionality generalized quantum master equations. J. Chem. Phys., 156:044119–13, 2022.

[22] R. Zwanzig. Nonequilibrium Statistical Mechanics. Oxford University Press, New York, 2001.

[23] Eitan Geva. Chapter 4: The quantum master equation, 2025. Unpublished lecture notes, University of Michigan.

[24] Yifan Lai and Eitan Geva. On simulating the dynamics of electronic populations and coherences via quantum master equations based on treating off-diagonal electronic coupling terms as a small perturbation. 155(20):204101. Publisher: American Institute of Physics.

[25] Yifan Lai and Eitan Geva. Electronic absorption spectra from off-diagonal quantum master equations. 157(10):104115.

[26] M.A. Nielsen and I. Chuang. Quantum computation and quantum information. Cambridge University Press, New York, 2000.

[27] Brandon C Allen, Xiaohan Dan, Delmar G A Cabral, Nam P Vu, Cameron Cianci, Alexander V Soudackov, Rishab Dutta, Sabre Kais, Eitan Geva, and Victor S Batista. QFlux: Classical foundations for quantum dynamics simulation. part i - building intuition and computational workflows.

[28] Alexander V Soudackov, Delmar G A Cabral, Brandon C Allen, Xiaohan Dan, Nam P Vu, Cameron Cianci, Rishab Dutta, Sabre Kais, Eitan Geva, and Victor S Batista. QFlux: Quantum circuit implementations of molecular dynamics. part III - state initialization and unitary decomposition.

[29] Frank Schlawin, Manuel Gessner, Andreas Buchleitner, Tobias Schätz, and Spiros S. Skourtis. Continuously parametrized quantum simulation of molecular electron-transfer reactions. 2(1):010314.

[30] Or Katz and Christopher Monroe. Programmable quantum simulations of bosonic systems with trapped ions. 131(3):033604.

[31] Lei Feng, Or Katz, Casey Haack, Mohammad Maghrebi, Alexey V. Gorshkov, Zhexuan Gong, Marko Cetina, and Christopher Monroe. Continuous symmetry breaking in a trapped-ion spin chain. 623(7988):713–717.

[32] Alejandro Cros Carrillo de Albornoz, Rodrigo G. Cortiñas, Max Schäfer, Nicholas E. Frattini, Brandon Allen, Delmar G. A. Cabral, Pablo E. Videla, Pouya Khazaei, Eitan Geva, Victor S. Batista, and Michel H. Devoret. Oscillatory dissipative tunneling in an asymmetric double-well potential.

[33] Jayameenakshi Venkatraman, Rodrigo G. Cortinas, Nicholas E. Frattini, Xu Xiao, and Michel H. Devoret. A driven quantum superconducting circuit with multiple tunable degeneracies. arXiv:2211.04605, May 2023. http://arxiv.org/abs/2211.04605 (accessed 2023-11-13).

[34] Jorge Chávez-Carlos, Talía L. M. Lezama, Rodrigo G. Cortiñas, Jayameenakshi Venkatraman, Michel H. Devoret, Victor S. Batista, Francisco Pérez-Bernal, and Lea F. Santos. Spectral kissing and its dynamical consequences in the squeeze-driven Kerr oscillator. npj Quantum Inf., 9(1):76, July 2023.

[35] Jayameenakshi Venkatraman, Xu Xiao, Rodrigo G. Cortiñas, and Michel H. Devoret. On the static effective lindbladian of the squeezed kerr oscillator.

[36] Nicholas E. Frattini, Rodrigo G. Cortiñas, Jayameenakshi Venkatraman, Xu Xiao, Qile Su, Chan U. Lei, Benjamin J. Chapman, Vidul R. Joshi, S. M. Girvin, Robert J. Schoelkopf, Shruti Puri, and Michel H. Devoret. Observation of pairwise level degeneracies and the quantum regime of the arrhenius law in a double-well parametric oscillator. Phys. Rev. X, 14:031040, Sep 2024.

[37] I. M. Georgescu, S. Ashhab, and Franco Nori. Quantum simulation. Rev. Mod. Phys., 86(1):153–185, March 2014.

[38] Ehud Altman, Kenneth R. Brown, Giuseppe Carleo, Lincoln D. Carr, Eugene Demler, Cheng Chin, Brian DeMarco, Sophia E. Economou, Mark A. Eriksson, Kai-Mei C. Fu, Markus Greiner, Kaden R.A. Hazzard, Randall G. Hulet, Alicia J. Kollár, Benjamin L. Lev, Mikhail D. Lukin, Ruichao Ma, Xiao Mi, Shashank Misra, Christopher Monroe, Kater Murch, Zaira Nazario, Kang-Kuen Ni, Andrew C. Potter, Pedram Roushan, Mark Saffman, Monika Schleier-Smith, Irfan Siddiqi, Raymond Simmonds, Meenakshi Singh, I.B. Spielman, Kristan Temme, David S. Weiss, Jelena Vučković, Vladan Vuletić, Jun Ye, and Martin Zwierlein. Quantum Simulators: Architectures and Opportunities. PRX Quantum, 2(1):017003, February 2021.

[39] Ignacio Loaiza and Artur F. Izmaylov. Block-invariant symmetry shift: Preprocessing technique for second-quantized hamiltonians to improve their decompositions to linear combination of unitaries. 19(22):8201–8209.

[40] Ignacio Loaiza, Aritra Sankar Brahmachari, and Artur F Izmaylov. Majorana tensor decomposition: a unifying framework for decompositions of fermionic hamiltonians to linear combination of unitaries. 10(3):035035.

[41] Ignacio Loaiza, Alireza Marefat Khah, Nathan Wiebe, and Artur F Izmaylov. Reducing molecular electronic hamiltonian simulation cost for linear combination of unitaries approaches. 8(3):035019.

[42] Béla Sz.-Nagy, Ciprian Foias, Hari Bercovici, and László Kérchy. Harmonic Analysis of Operators on Hilbert Space. Springer New York.

[43] Zixuan Hu, Rongxin Xia, and Sabre Kais. A quantum algorithm for evolving open quantum dynamics on quantum computing devices. 10(1):3301.

[44] Yuchen Wang, Ellen Mulvihill, Zixuan Hu, Ningyi Lyu, Saurabh Shivpuje, Yudan Liu, Micheline B. Soley, Eitan Geva, Victor S. Batista, and Sabre Kais. Simulating open quantum system dynamics on NISQ computers with generalized quantum master equations. 19(15):4851–4862.

[45] Ningyi Lyu, Pouya Khazaei, Eitan Geva, and Victor S. Batista. Simulating cavity-modified electron transfer dynamics on NISQ computers. 15(37):9535–9542.

[46] W. Forrest Stinespring. Positive functions on c -algebras. 6(2):211.

[47] Francesco Buscemi, G. Mauro D'Ariano, and Massimiliano F. Sacchi. Physical realizations of quantum operations. 68(4):042113.

[48] Ryan Sweke, Ilya Sinayskiy, Denis Bernard, and Francesco Petruccione. Universal simulation of markovian open quantum systems. 91(6):062308.

[49] Xiaohan Dan, Eitan Geva, and Victor S. Batista. Simulating non-markovian quantum dynamics on NISQ computers using the hierarchical equations of motion. 21(4):1530–1546.

[50] Anthony W. Schlimgen, Kade Head-Marsden, LeeAnn M. Sager-Smith, Prineha Narang, and David A. Mazziotti. Quantum state preparation and nonunitary evolution with diagonal operators. 106(2):022414.

[51] Chang Woo Kim, John M. Nichol, Andrew N. Jordan, and Ignacio Franco. Analog quantum simulation of the dynamics of open quantum systems with quantum dots and microelectronic circuits. 3(4):040308.

[52] Delmar G. A. Cabral, Pouya Khazaei, Brandon C. Allen, Pablo E. Videla, Max Schäfer, Rodrigo G. Cortiñas, Alejandro Cros Carrillo De Albornoz, Jorge Chávez-Carlos, Lea F. Santos, Eitan Geva, and Victor S. Batista. A roadmap for simulating chemical dynamics on a parametrically driven bosonic quantum device. 15(48):12042–12050.

[53] Xiang Sun and Eitan Geva. Equilibrium fermi's golden rule charge transfer rate constants in the condensed phase: The linearized semiclassical method vs classical marcus theory. 120(19):2976–2990.

[54] Xiang Sun and Eitan Geva. Nonequilibrium fermi's golden rule charge transfer rates via the linearized semiclassical method. 12(6):2926–2941. Publisher: American Chemical Society.

[55] Xiang Sun and Eitan Geva. Non-condon equilibrium fermi's golden rule electronic transition rate constants via the linearized semiclassical method. 144(24):244105.

[56] Xiang Sun and Eitan Geva. Non-condon nonequilibrium fermi's golden rule rates from the linearized semiclassical method. 145(6):064109.

[57] Hans-Dieter Meyera) and William H. Miller. A classical analog for electronic degrees of freedom in nonadiabatic collision processes. 70(7):3214–3223.

[58] M. Thoss and G. Stock. Mapping approach to the semiclassical description of nonadiabatic quantum dynamics. Phys. Rev. A, 59:64–79, 1999.

[59] Xing Gao, Maximilian A. C. Saller, Yudan Liu, Aaron Kelly, Jeremy O. Richardson, and Eitan Geva. Benchmarking quasiclassical mapping hamiltonian methods for simulating electronically nonadiabatic molecular dynamics. 16(5):2883–2895.

[60] Ellen Mulvihill, Xing Gao, Yudan Liu, Alexander Schubert, Barry D. Dunietz, and Eitan Geva. Combining the mapping hamiltonian linearized semiclassical approach with the generalized quantum master equation to simulate electronically nonadiabatic molecular dynamics. 151(7):074103.

[61] Qiang Shi and Eitan Geva. A derivation of the mixed quantum-classical liouville equation from the influence functional formalism. 121(8):3393–3404.

[62] Alexei A. Kananenka, Chang-Yu Hsieh, Jianshu Cao, and Eitan Geva. Accurate long-time mixed quantum-classical liouville dynamics via the transfer tensor method. 7(23):4809–4814.

[63] John C. Tully. Molecular dynamics with electronic transitions. 93(2):1061–1071.

[64] Michael F. Herman. A semiclassical surface hopping propagator for nonadiabatic problems. 103(18):8081–8097.

[65] R. B. Gerber, V. Buch, and Mark A. Ratner. Time-dependent self-consistent field approximation for intramolecular energy transfer. i. formulation and application to dissociation of van der waals molecules. 77(6):3022–3030.

[66] Gert D. Billing. Quantum corrections to the classical path theory. 99(8):5849–5857.

[67] P. F. Barbara, T. J. Meyer, and M. A. Ratner. Contemporary issues in electron transfer research. J. Phys. Chem., 100(31):13148–13168, 1996.

[68] D. Chandler. Electron transfer in water and other polar environments, how it happens. In B. J. Berne, G. Cicootti, and D. F. Coker, editors, Classical and Quantum Dynamics in Condensed Phase Simulations, chapter 2, pages 25–50. World Scientific, New Jersey, 1997.

[69] U. Weiss. Quantum dissipative systems. World Scientific, Singapore, 1999.

[70] V. May and O. Kühn. Charge and Energy Transfer Dynamics in Molecular Systems. Willey-VCH, Berlin, 2000.

[71] A. Nitzan. Chemical Dynamics in Condensed Phases. Oxford University Press, New York, 2006.

[72] P.A. Liddell, D. Kuciauskas, J.P. Sumida, B. Nash, D. Nguyen, A.L. Moore, T.A. Moore, and D. Gust. Photoinduced charge separation and charge recombination to a triplet state in a carotene-porphyrin-fullerene triad. J. Am. Chem. Soc., 119:1400–1405, 1997.

[73] P.A. Liddell, G. Kodis, A.L. Moore, T.A. Moore, and D. Gust. Photo switching of photoinduced electron transfer in a dithienylethene-porphyrin-fullerene triad molecule. J. Am. Chem. Soc., 124:7668–7669, 2002.

[74] J-L Brédas, D. Beljonne, V. Coropceanu, and J. Cornil. Charge-Transfer and Energy-Transfer Processes in π-Conjugated Oligomers and Polymers: A Molecular Picture. Chem. Rev., 104:4971–5004, 2004.

[75] A.C. Rizzi, M. van Gastel, P.A. Liddell, R.E. Palacios, G.F. Moore, G. Kodis, A.L. Moore, T.A. Moore, D. Gust, and S.E. Braslavsky. Entropic changes control the charge separation process in triads mimicking photosynthetic charge separation. J. Phys. Chem. A, 112:4215–4223, 2008.

[76] H. Tian, Z. Yu, A. Hagfeldt, L. Kloo, and L. Sun. Organic Redox Couples and Organic Counter Electrode for Efficient Organic Dye-Sensitized Solar Cells. J. Am. Chem. Soc., 133:9413–9422, 2011.

[77] A. Mishra, M.K.R. Fischer, and P. Bäuerle. Metal-Free Organic Dyes for Dye-Sensitized Solar Cells: From Structure: Property Relationships to Design Rules. Angew. Chem. Int. Ed., 48:2474–2499, 2009.

[78] S. M. Feldt, E. A. Gibson, E. Gabrielsson, L. Sun, G. Boschloo, and A. Hagfeldt. Design of organic dyes and cobalt polypyridine redox mediators for high-efficiency dye-sensitized solar cells. J. Am. Chem. Soc., 132:16714–16724, 2010.

[79] Y. Zhao and W. Liang. Charge transfer in organic molecules for solar cells: Theoretical perspective. Chem. Soc. Rev., 41:1075–1087, 2012.

[80] M. H. Lee, B. D. Dunietz, and E. Geva. Calculation from first principles of intramolecular golden-rule rate constants for photo-induced electron transfer in molecular donor-acceptor systems. J. Phys. Chem. C, 117:23391–23401, 2013.

[81] M.H. Lee, B.D. Dunietz, and E. Geva. Donor-to-donor vs. donor-to-acceptor interfacial charge transfer states in the phthalocyanine-fullerene organic photovoltaic system. J. Phys. Chem. Lett., 5:3810–3816, 2014.

[82] C.R. Baiz and K.J. Kubarych. Ultrafast vibrational Stark-effect spectroscopy: exploring charge-transfer reactions by directly monitoring the solvation shell response. J. Am. Chem. Soc., 132(37):12784–12785, September 2010.

[83] B. Strodel and G. Stock. Quantum modeling of transient infrared spectra reflecting photoinduced electron- transfer dynamics. J. Chem. Phys., 124:114105, 2006.

[84] J. Bredenbeck, J. Helbing, and P. Hamm. Labeling vibrations by light: Ultrafast transient 2D-IR spectroscopy tracks vibrational modes during photoinduced charge transfer. J. Am. Chem. Soc., 126:990–1991, 2004.

[85] S J Schmidtke, D F Underwood, and D A Blank. Following the solvent directly during ultrafast excited state proton transfer. J. Am. Chem. Soc., 126(28):8620–8621, July 2004.

[86] D. Xu and K. Schulten. Coupling of protein motion to electron transfer in a photosynthetic reaction center: Investigating the low temperature behavior in the framework of the spin–boson model. Chem. Phys., 182:91–117, 1994.

[87] A. Ishizaki and G.R. Fleming. Quantum Coherence in Photosynthetic Light Harvesting. Annu. Rev. Condens. Matter Phys., 3:333–361, 2012.

[88] A.K. Manna, D. Balamurugan, M.S. Cheung, and B.D. Dunietz. Unraveling the Mechanism of Photoinduced Charge Transfer in Carotenoid-Porphyrin-C_{60} Molecular Triad. J. Phys. Chem. Lett., 6:1231–1237, 2015.

[89] Kuo Kan Liang, Chih-Kai Lin, Huan-Cheng Chang, Albert A Villaeys, Michitoshi Hayashi, and Sheng Hsien Lin. Calculation of the vibrationally non-relaxed photoinduced electron transfer rate constant in dye-sensitized solar cells. Phys. Chem. Chem. Phys., 9(7):853–859, 2007.

[90] R. D. Coalson, D. G. Evans, and A. Nitzan. A nonequilibrium golden rule formula for electronic state populations in nonadiabatically coupled systems. J. Chem. Phys., 101:436–448, 1994.

[91] M. Cho and R. J. Silbey. Nonequilibrium photoinduced electron transfer. J. Chem. Phys., 103:595–606, 1995.

[92] A.F. Izmaylov, D. Mendive-Tapia, M.J. Bearpark, M.A. Robb, J.C. Tully, and M.J. Frisch. Nonequilibrium Fermi golden rule for electronic transitions through conical intersections. J. Chem. Phys., 135:234106–14, 2011.

[93] X. Sun and E. Geva. Non-Condon nonequilibrium Fermi's golden rule rates from the linearized semiclassical method. J. Chem. Phys., 145:064109–19, 2016.

[94] Z. Hu, Z. Tong, M. S. Cheung, B. D. Dunietz, E. Geva, and X. Sun. Photoinduced charge transfer dynamics in the carotenoid-porphyrin-c_{60} triad via the linearized semiclassical nonequilibrium fermi's golden rule. J. Chem. Theory Comput., 124:9579–9591, 2020.

[95] D. Brian, Z. Liu, B.D. Dunietz, E. Geva, and X. Sun. Three-state harmonic models for photoinduced charge transfer. J. Chem. Phys., 154:174105–18, 2021.

[96] R. Kubo and Y. Toyozawa. Application of the method of generating function to radiative and non-radiative transitions of a trapped electron in a crystal. Prog. Theoret. Phys., 13:160–182, 1955.

[97] J. Jortner. Temperature dependent activation energy for electron transfer between biological molecules. J. Chem. Phys., 64(12):4860–4867, 1976.

[98] Kurt V. Mikkelsen and Mark A. Ratner. Electron tunneling in solid-state electron-transfer reactions. Chem. Rev., 87(1):113–153, 1987.

[99] Marshall D. Newton and Norman Sutin. Electron transfer reactions in condensed phases. Ann. Rev. Phys. Chem., 35:437–480, 1984.

[100] Marshall D. Newton. Quantum chemical probes of electron-transfer kinetics: the nature of donor-acceptor interactions. Chem. Rev., 91(5):767–792, 1991.

[101] Q. Shi and E. Geva. Nonradiative electronic relaxation rate constants from approximations based on linearizing the path-integral forward-backward action. J. Phys. Chem. A, 108:6109–6116, 2004.

[102] X. Sun and E. Geva. Equilibrium Fermi's Golden Rule Charge Transfer Rate Constants in the Condensed Phase: The Linearized Semiclassical Method vs Classical Marcus Theory. J. Phys. Chem. A, 120:2976–2990, 2016.

[103] X. Sun and E. Geva. Non-Condon Equilibrium Fermi's Golden Rule Electronic Transition Rate Constants Via The Linearized Semiclassical Method. J. Chem. Phys., 144:244105–12, 2016.

[104] X. Sun, P. Zhang, Y. Lai, K.L. Williams, M.S. Cheung, B.D. Dunietz, and E. Geva. Computational Study of Charge-Transfer Dynamics in the Carotenoid-Porphyrin-C_{60} Molecular Triad Solvated in Explicit Tetrahydrofuran and Its Spectroscopic Signature. J. Phys. Chem. C, 122:11288–11299, 2018.

[105] A. Schubert, S. Bhandari, E. Geva, and B.D. Dunietz. A computational study of the electronic energy and charge transfer rates and pathways in the tetraphenyldibenzoperiflanthene/fullerene interfacial dyad. J. Phys. Chem. Lett., 14:9569–9583, 2023.

[106] S. Jang, Y-J Jung, and R.J. Silbey. Nonequilibrium generalization of Forster–Dexter theory for excitation energy transfer. Chem. Phys., 275:319–332, 2002.

[107] N. R. Kestner, J. Logan, and J. Jortner. Thermal electron transfer reactions in polar solvents. J. Phys. Chem., 78(21):2148–2166, 1974.

[108] J. Jortner and M. Bixon. Intramolecular vibrational excitations accompanying solvent-controlled electron transfer reactions. J. Chem. Phys., 88(1):167–170, 1988.

[109] A. J. Leggett, S. Chakravarty, A. T. Dorsey, Matthew P. A. Fisher, Anupam Garg, and W. Zwerger. Dynamics of the dissipative two-state system. Rev. Mod. Phys., 59(1):1–85, 1987.

[110] J.S. Endicott, L. Joubert-Doriol, and A.F. Izmaylov. A perturbative formalism for electronic transitions through conical intersections in a fully quadratic vibronic model. J. Chem. Phys., 141:034104–10, 2014.

[111] R.. A. Marcus. On the theory of oxidation-reduction reactions involving electron transfer. I. J. Chem. Phys., 24(5):966–978, 1956.

[112] R. A. Marcus. Electrostatic free energy and other properties of states having nonequilibrium polarization. I. J. Chem. Phys., 24(5):979–989, 1956.

[113] R.A. Marcus. Electron transfer reactions in chemistry. Theory and experiment. Rev. Mod. Phys., 65:599–610, 1993.

[114] P. Andrew and W. L. Barnes. Förster energy transfer in an optical microcavity. Science, 290:785–788, 2000.

[115] T. Schwartz, J.A. Hutchison, C. Genet, and T.W. Ebbesen. Reversible Switching of Ultrastrong Light-Molecule Coupling. Phys. Rev. Lett., 106:196405–4, 2011.

[116] T.W. Ebbesen. Hybrid Light-Matter States in a Molecular and Material Science Perspective. Acc. Chem. Res., 49:2403–2412, 2016.

[117] A. Thomas, J. George, A. Shalabney, M. Dryzhakov, S.J. Varma, J. Moran, T. Chervy, X. Zhong, E. Devaux, C. Genet, J.A. Hutchison, and T.W. Ebbesen. Ground-State Chemical Reactivity under Vibrational Coupling to the Vacuum Electromagnetic Field. Angew. Chem., 128:11634–11638, 2016.

[118] F. Herrera and F.C. Spano. Cavity-Controlled Chemistry in Molecular Ensembles. Phys. Rev. Lett., 116:238301–6, 2016.

[119] J. Flick, M. Ruggenthaler, H. Appel, and A. Rubio. Atoms and molecules in cavities, from weak to strong coupling in quantum-electrodynamics (QED) chemistry. Proc. Natl. Acad. Sci. USA, 114:3026–3034, 2017.

[120] J. Fregoni, G. Granucci, E. Coccia, M. Persico, and S. Corni. Manipulating azobenzene photoisomerization through strong light-molecule coupling. Nat. Commun., 9:2613–9, 2018.

[121] J. Flick, N. Rivera, and P. Narang. Strong light-matter coupling in quantum chemistry and quantum photonics. Nanophotonics, 7:1479–1501, 2020.

[122] R. Bhuyan, J. Mony, O. Kotov, G.W.Castellanos, J. Gómez-Rivas, T.O. Shegai, and K. Börjesson. The rise and current status of polaritonic photochemistry and photophysics. Chem. Rev., 123:1087710919, 2024.

[123] B. Xiang and W. Xiong. Molecular polaritons for chemistry, photonics and quantum technologies. Chem. Rev., 124:25122552, 2024.

[124] N.M. Hoffmann, C. Schäfer, A. Rubio, A. Kelly, and H. Appel. Capturing vacuum fluctuations and photon correlations in cavity quantum electrodynamics with multitrajectory Ehrenfest dynamics. Phys. Rev. A, 99:063819–9, 2019.

[125] N.M. Hoffmann, C. Schäfer, N. Säkkinen, A. Rubio, H. Appel, and A. Kelly. Benchmarking semiclassical and perturbative methods for real-time simulations of cavity-bound emission and interference. J. Chem. Phys., 151:244113–14, 2019.

[126] N.M. Hoffmann, L. Lacombe, A. Rubio, and N.T. Maitra. Effect of many modes on self-polarization and photochemical suppression in cavities. J. Chem. Phys., 153:104103–10, 2020.

[127] T.E. Li, J.E. Subotnik, and A. Nitzan. Cavity molecular dynamics simulations of liquid water under vibrational ultrastrong coupling, 2020.

[128] M.A.C. Saller, A. Kelly, and E. Geva. Benchmarking Quasiclassical Mapping Hamiltonian Methods for Simulating Cavity-Modified Molecular Dynamics. J. Phys. Chem. Lett., 12:3163–3170, 2021.

[129] T.S. Haugland, C. Schäfer, E. Ronca, A. Rubio, and H. Koch. Intermolecular interactions in optical cavities: An ab initio QED study. J. Chem. Phys., 154:094113, 2021.

[130] S.N. Chowdhury, A. Mandal, and P. Huo. Ring polymer quantization of the photon field in polariton chemistry. J. Chem. Phys., 154:044109–11, 2021.

[131] T.E. Li, A. Nitzan, and J.E. Subotnik. Cavity molecular dynamics simulations of vibrational polariton-enhanced molecular nonlinear absorption. J. Chem. Phys., 154:094124, 2021.

[132] T.E. Li, A. Nitzan, and J.E. Subotnik. Collective Vibrational Strong Coupling Effects on Molecular Vibrational Relaxation and Energy Transfer: Numerical Insights via Cavity Molecular Dynamics Simulations. Angew. Chem., 133:15661–15668, 2021.

[133] E.W. Fischer, J. Anders, and P. Saalfrank. Cavity-altered thermal isomerization rates and dynamical resonant localization in vibro-polaritonic chemistry. J. Chem. Phys., 156:154305, 2022.

[134] D.S. Wang, T. Neuman, S.F. Yelin, and J. Flick. Cavity-Modified Unimolecular Dissociation Reactions via Intramolecular Vibrational Energy Redistribution. J. Phys. Chem. Lett., 13:3317–3324, 2022.

[135] T.E. Li, A. Nitzan, and J.E. Subotnik. Polariton relaxation under vibrational strong coupling: Comparing cavity molecular dynamics simulations against Fermi's golden rule rate. J. Chem. Phys., 156:134106, 2022.

[136] A. Mandal, X. Li, and P. Huo. Theory of vibrational polariton chemistry in the collective coupling regime. J. Chem. Phys., 156:014101, 2022.

[137] A. Mandal, T.D. Krauss, and P. Huo. Polariton-Mediated Electron Transfer via Cavity Quantum Electrodynamics. J. Phys. Chem. B, 124:6321–6340, 2020.

[138] T.E. Li, H-T Chen, A. Nitzan, and J.E. Subotnik. Quasiclassical modeling of cavity quantum electrodynamics. Phys. Rev. A, 101:033831 – 17, 2020.

[139] A. Mandal, M.A.D. Taylor, B.M. Weight, E.R. Koessler, X. Li, and P. Huo. Theoretical advances in polariton chemistry and molecular cavity quantum electrodynamics. Chem. Rev., 123:97869879, 2023.

[140] M.A.C. Saller, Y. Lai, and E. Geva. Cavity-modified fermi's golden rule rate constants from cavity-free inputs. J. Phys. Chem. C, 127:3154–3164, 2023.

[141] Z. Tong, X. Gao, M.S. Cheung, B.D. Dunietz, E. Geva, and X. Sun. Charge transfer rate constants for the carotenoid-porphyrin-C_{60} molecular triad dissolved in tetrahydrofuran: The spin-boson model vs the linearized semiclassical approximation. J. Chem. Phys., 153:044105–10, 2020.

[142] A. Garg, J. N. Onuchic, and V. Ambegaokar. Effect of friction on electron transfer in biomolecules. J. Chem. Phys., 83:4491–4503, 1985.

[143] A. Trushechkin. Calculation of coherences in Förster and modified Redfield theories of excitation energy transfer. J. Chem. Phys., 151:074101–19, 2019.

[144] M.A.C. Saller, Y. Lai, and E. Geva. Cavity-modified fermi's golden rule rate constants: Beyond the single mode approximation. J. Chem. Phys., 159:151105, 2023.

[145] S. Mukamel. Principles of Nonlinear Optical Spectroscopy. Oxford University Press, Oxford, 1995.

[146] R. Kubo, M. Toda, and N. Hashitsume. Statistical Physics II: Nonequilibrium Statistical Mechanics. Springer-Verlag, New York, 1985.

[147] N. Makri. The Linear Response Approximation and Its Lowest Order Corrections: An Influence Functional Approach. J. Phys. Chem. B, 103(15):2823–2829, 1999.

[148] Anirban Hazra, Alexander V. Soudackov, and Sharon Hammes-Schiffer. Role of solvent dynamics in ultrafast photoinduced proton-coupled electron transfer reactions in solution. 114(38):12319–12332.

[149] X. Sun and E. Geva. Exact vs. Asymptotic Spectral Densities in the Garg-Onuchic-Ambegaokar Charge Transfer Model and its Effect on Fermi's Golden Rule Rate Constants. J. Chem. Phys., 144:044106–4, 2016.

[150] A. D. Godbeer, J. S. Al-Khalili, and P. D. Stevenson. Modelling proton tunnelling in the adenine–thymine base pair. 17(19):13034–13044.

[151] Zhubin Hu, Zhengqing Tong, Margaret S. Cheung, Barry D. Dunietz, Eitan Geva, and Xiang Sun. Photoinduced charge transfer dynamics in the carotenoid–porphyrin–c $_{60}$ triad via the linearized semiclassical nonequilibrium fermi's golden rule. 124(43):9579–9591.

[152] Xiang Sun, Pengzhi Zhang, Yifan Lai, Kyle L. Williams, Margaret S. Cheung, Barry D. Dunietz, and Eitan Geva. Computational study of charge-transfer dynamics in the carotenoid–porphyrin–c $_{60}$ molecular triad solvated in explicit tetrahydrofuran and its spectroscopic signature. 122(21):11288–11299.

[153] K. Wright. Differential equations for the analytic singular value decomposition of a matrix. 63(1):283–295.

[154] L. Dieci and C. Elia. SVD algorithms to approximate spectra of dynamical systems. 79(4):1235–1254.

[155] Luca Dieci and Erik S. Van Vleck. Lyapunov spectral intervals: Theory and computation. 40(2):516–542.

[156] L. Dieci and C. Elia. The singular value decomposition to approximate spectra of dynamical systems. theoretical aspects. 230(2):502–531.

[157] Luca Dieci and Erik S. Van Vleck. Lyapunov and sacker–sell spectral intervals. 19(2):265–293.

[158] Roman Korol, Nawaf Bou-Rabee, and Thomas F. Miller III. Cayley modification for strongly stable path-integral and ring-polymer molecular dynamics. 151(12):124103.

[159] Lena Leitenmaier and Olof Runborg. Heterogeneous multiscale methods for the landau–lifshitz equation. 93(3):76.

[160] Kai Li. The qubit fidelity under different error mechanisms based on error correction threshold. 10:893507.

[161] Henry Eyring. The Activated Complex in Chemical Reactions. J. Chem. Phys., 3(2):107–115, February 1935.

[162] Donald G. Truhlar, Bruce C. Garrett, and Stephen J. Klippenstein. Current Status of Transition-State Theory. J. Phys. Chem., 100(31):12771–12800, January 1996.

[163] P. Pechukas. Transition State Theory. Annu. Rev. Phys. Chem., 32(Volume 32,):159–177, October 1981.

[164] Keith J. Laidler and M. Christine King. Development of transition-state theory. J. Phys. Chem., 87(15):2657–2664, July 1983.

[165] Eli Pollak and Peter Talkner. Reaction rate theory: What it was, where is it today, and where is it going? Chaos, 15(2):026116, June 2005.

[166] N. E. Frattini, U. Vool, S. Shankar, A. Narla, K. M. Sliwa, and M. H. Devoret. 3-wave mixing Josephson dipole element. Appl. Phys. Lett., 110(22):222603, 05 2017.

[167] Nicholas E Frattini, Rodrigo G Cortiñas, Jayameenakshi Venkatraman, Xu Xiao, Qile Su, Chan U Lei, Benjamin J Chapman, Vidul R Joshi, SM Girvin, and Robert J Schoelkopf. The squeezed kerr oscillator: Spectral kissing and phase-flip robustness. arXiv:2209.03934, 2022. http://arxiv.org/abs/2209.03934 (accessed 2024-10-30).

[168] Tsunenobu Yamamoto. Quantum Statistical Mechanical Theory of the Rate of Exchange Chemical Reactions in the Gas Phase. J. Chem. Phys., 33(1):281–289, July 1960.

[169] David Chandler. Statistical mechanics of isomerization dynamics in liquids and the transition state approximation. J. Chem. Phys., 68(6):2959–2970, March 1978.

[170] Eitan Geva, Qiang Shi, and Gregory A. Voth. Quantum-mechanical reaction rate constants from centroid molecular dynamics simulations. J. Chem. Phys., 115(20):9209–9222, November 2001.

[171] Francisco X. Vazquez, Surma Talapatra, Roseanne J. Sension, and Eitan Geva. The Entropic Origin of Solvent Effects on the Single Bond *cZt-tZt* Isomerization Rate Constant of 1,3,5- *cis* -Hexatriene in Alkane and Alcohol Solvents: A Molecular Dynamics Study. J. Phys. Chem. B, 118(28):7869–7877, July 2014.

[172] William H. Miller. Quantum mechanical transition state theory and a new semiclassical model for reaction rate constants. J. Chem. Phys., 61(5):1823–1834, September 1974.

[173] William H. Miller, Steven D. Schwartz, and John W. Tromp. Quantum mechanical rate constants for bimolecular reactions. J. Chem. Phys., 79(10):4889–4898, November 1983.

[174] William H. Miller. "Direct" and "Correct" Calculation of Canonical and Microcanonical Rate Constants for Chemical Reactions. J. Phys. Chem. A, 102(5):793–806, January 1998.

[175] AD Godbeer, JS Al-Khalili, and PD Stevenson. Modelling proton tunnelling in the adenine–thymine base pair. Phys. Chem. Chem. Phys., 17(19):13034–13044, 2015.

[176] Micheline B Soley, Paul Bergold, and Victor S Batista. Iterative power algorithm for global optimization with quantics tensor trains. J. Chem. Theory Comput., 17(6):3280–3291, 2021.

[177] Micheline B Soley, Paul Bergold, Alex A Gorodetsky, and Victor S Batista. Functional tensor-train chebyshev method for multidimensional quantum dynamics simulations. J. Chem. Theory Comput., 18(1):25–36, 2021.

[178] James D Watson and Francis HC Crick. Genetical implications of the structure of deoxyribonucleic acid. Jama, 269(15):1967–1969, 1993.

[179] Gerhard L. Closs and John R. Miller. Intramolecular Long-Distance Electron Transfer in Organic Molecules. Science, 240(4851):440–447, April 1988.

[180] J. R. Miller, L. T. Calcaterra, and G. L. Closs. Intramolecular long-distance electron transfer in radical anions. The effects of free energy and solvent on the reaction rates. J. Am. Chem. Soc., 106(10):3047–3049, May 1984.

[181] Rudolph A. Marcus. Electron Transfer Reactions in Chemistry: Theory and Experiment (Nobel Lecture). Angew. Chem., Int. Ed. Engl., 32(8):1111–1121, 1993.

[182] Frank Schlawin, Manuel Gessner, Andreas Buchleitner, Tobias Schätz, and Spiros S. Skourtis. Continuously parametrized quantum simulation of molecular electron-transfer reactions. PRX Quantum, 2:010314, Jan 2021.

[183] Visal So, Midhuna Duraisamy Suganthi, Abhishek Menon, Mingjian Zhu, Roman Zhuravel, Han Pu, Peter G. Wolynes, José N. Onuchic, and Guido Pagano. Trapped-ion quantum simulation of electron transfer models with tunable dissipation. arXiv:2405.10368, 2024. http://arxiv.org/abs/2405.10368 (accessed 2024-10-30).

[184] Miguel A. Prado Reynoso, D. J. Nader, Jorge Chávez-Carlos, B. E. Ordaz-Mendoza, Rodrigo G. Cortiñas, Victor S. Batista, S. Lerma-Hernández, Francisco Pérez-Bernal, and Lea F. Santos. Quantum tunneling and level crossings in the squeeze-driven kerr oscillator. Phys. Rev. A, 108:033709, 2023.

[185] Francesco Iachello, Rodrigo G Cortiñas, Francisco Pérez-Bernal, and Lea F Santos. Symmetries of the squeeze-driven kerr oscillator. J. Phys. A, 56:495305, 2023.

[186] Ignacio García-Mata, Rodrigo G. Cortiñas, Xu Xiao, Jorge Chávez-Carlos, Victor S. Batista, Lea F. Santos, and Diego A. Wisniacki. Effective versus Floquet theory for the Kerr parametric oscillator. Quantum, 8:1298, March 2024.

[187] Jorge Chávez-Carlos, Miguel A. Prado Reynoso, Ignacio García-Mata, Victor S. Batista, Francisco Pérez-Bernal, Diego A. Wisniacki, and Lea F. Santos. Driving superconducting qubits into chaos. arXiv:2310.17698, 2024. https://arxiv.org/abs/2310.17698 (accessed 2024-10-30).

[188] Nicholas Frattini. Three-wave Mixing in Superconducting Circuits: Stabilizing Cats with SNAILs. Phd dissertation, Yale University, New Haven, CT. **2021**. https://elischolar.library.yale.edu/gsas_dissertations/332 (accessed 2024-11-13).

[189] Andy Z. Ding, Benjamin L. Brock, Alec Eickbusch, Akshay Koottandavida, Nicholas E. Frattini, Rodrigo G. Cortinas, Vidul R. Joshi, Stijn J. de Graaf, Benjamin J. Chapman, Suhas Ganjam, Luigi Frunzio, Robert J. Schoelkopf, and Michel H. Devoret. Quantum control of an oscillator with a kerr-cat qubit. arXiv:2407.10940, 2024. http://arxiv.org/abs/2407.10940 (accessed 2024-10-30).

[190] A. D. Godbeer, J. S. Al-Khalili, and P. D. Stevenson. Modelling proton tunnelling in the adenine–thymine base pair. Phys. Chem. Chem. Phys., 17:13034–13044, 2015.

[191] S Ghosh and S P Bhattacharyya. Dynamics of atom tunnelling in a symmetric double well coupled to an asymmetric double well: The case of malonaldehyde#. J. Chem. Sci., 124(1):13–19, January 2012.

[192] Subhasree Ghosh, Srijeeta Talukder, Shrabani Sen, and Pinaki Chaudhury. Optimised polychromatic field-mediated suppression of H-atom tunnelling in a coupled symmetric double well: two-dimensional malonaldehyde model. Mol. Phys., 113(23):3826–3838, December 2015.

[193] KW Murch, U Vool, D Zhou, SJ Weber, SM Girvin, and I Siddiqi. Cavity-assisted quantum bath engineering. Phys. Rev. Lett., 109(18):183602, 2012.

[194] JM Kitzman, JR Lane, Camryn Undershute, PM Harrington, NR Beysengulov, CA Mikolas, KW Murch, and Johannes Pollanen. Phononic bath engineering of a superconducting qubit. Nat. Commun., 14(1):3910, 2023.

[195] Chao Shen, Kyungjoo Noh, Victor V. Albert, Stefan Krastanov, M. H. Devoret, R. J. Schoelkopf, S. M. Girvin, and Liang Jiang. Quantum channel construction with circuit quantum electrodynamics. Phys. Rev. B, 95:134501, Apr 2017.

[196] VV Sivak, Alec Eickbusch, Baptiste Royer, Shraddha Singh, Ioannis Tsioutsios, Suhas Ganjam, Alessandro Miano, BL Brock, AZ Ding, Luigi Frunzio, et al. Real-time quantum error correction beyond break-even. Nature, 616(7955):50–55, 2023.

[197] Zaki Leghtas, Steven Touzard, Ioan M Pop, Angela Kou, Brian Vlastakis, Andrei Petrenko, Katrina M Sliwa, Anirudh Narla, Shyam Shankar, Michael J Hatridge, et al. Confining the state of light to a quantum manifold by engineered two-photon loss. Science, 347(6224):853–857, 2015.

[198] Zhengqing Tong, Xing Gao, Margaret S. Cheung, Barry D. Dunietz, Eitan Geva, and Xiang Sun. Charge transfer rate constants for the carotenoid-porphyrin-c $_{60}$ molecular triad dissolved in tetrahydrofuran: The spin-boson model vs the linearized semiclassical approximation. 153(4):044105.

[199] Arkajit Mandal, Xinyang Li, and Pengfei Huo. Theory of vibrational polariton chemistry in the collective coupling regime. 156(1):014101.

[200] Lachlan P. Lindoy, Arkajit Mandal, and David R. Reichman. Quantum dynamical effects of vibrational strong coupling in chemical reactivity. 14(1):2733.

[201] Jonathan Welch, Daniel Greenbaum, Sarah Mostame, and Alan Aspuru-Guzik. Efficient quantum circuits for diagonal unitaries without ancillas. 16(3):033040.

[202] Wynter Alford, Laetitia P. Bettmann, and Gabriel T. Landi. Subtleties in the pseudomodes formalism.

[203] Jayameenakshi Venkatraman, Xu Xiao, Rodrigo G. Cortiñas, and Michel H. Devoret. Nonlinear dissipation in a driven superconducting circuit. 110(4):042411.